Modeling and Design of a Solar House with Focus on a Ventilated Concrete Slab Coupled with a Building-Integrated Photovoltaic/thermal System

YuXiang Chen

A Thesis

in

The Department

of

Building, Civil, and Environmental Engineering

Presented in Partial Fulfillment of the Requirements
for the Degree of Master of Applied Science (Building Engineering) at
Concordia University
Montreal, Quebec, Canada

January 2009

Your file Votre référence
ISBN: 978-0-494-63298-7
Our file Notre référence
ISBN: 978-0-494-63298-7

Abstract

Modeling and Design of a Solar House with Focus on a Ventilated Concrete Slab Coupled with a Building-Integrated Photovoltaic/thermal System

YuXiang Chen

This thesis presents an interdisciplinary research of an integrated solar/structural system: an innovative ventilated concrete slab (VCS) thermally coupled with a building-integrated photovoltaic/thermal (BIPV/T) roof in a constructed energy-efficient solar house - ÉcoTerra. The house is one of twelve demonstration houses across Canada that were built within the "EQuilibrium Housing" initiative launched by Canada Mortgage and Housing Corporation. The BIPV/T system converts solar irradiance to electricity with the photovoltaic (PV) panels and, at the same time, collects thermal energy from the PV panels and cools them down. The VCS uses the structural mass for active thermal energy storage. In the heating season, it stores part of the collected thermal energy from the BIPV/T roof and releases it passively into the living space, thus lowering space heating energy consumption. ÉcoTerra adopts an integrated space and domestic hot water heating system, which combines the solar systems (VCS-BIPV/T and passive solar design) and a ground source heat pump. Shown by full-scale monitoring data, a large amount of thermal energy can be efficiently collected by the BIPV/T roof and stored in the VCS. The VCS-BIPV/T system significantly reduces the space heating energy consumption in ÉcoTerra. The main contributions of this research are designing an original type of VCS, assessing the thermal performance of the VCS-BIPV/T system, and developing numerical simulation models for the VCS and the BIPV/T roof. Numerical simulation models are verified with full-scale monitoring data. The design concepts and construction details of the VCS-BIPV/T system and the house are also presented.

Acknowledgements

This work could not have been accomplished without the support and help of many people and institutions, for which I am very grateful.

I am especially grateful to my co-supervisor Dr. A. K. Athienitis for conveying his enthusiasm for and profound knowledge of energy-efficient solar houses and who gives me the opportunity to work on the ÉcoTerra project. I am deeply indebted to Dr. K. E. Galal, my other co-supervisor, for his uninterrupted thoughtfulness and his support for carrying out my present work. Dr. Athienitis and Dr. Galal have been mentoring me since my undergraduate studies. I am full of gratitude for their continuous guidance, encouragement and trust over the years.

ÉcoTerra project is a collective work of many people. I would like to thank the people from Alouette Homes (the house builder), especially Bradley Berneche (owner), Nicole Laberge (project manager) and Jean Ardouin (construction manager). They did not only construct ÉcoTerra, but also provided nonstop support for my research work. Dr. Kwang-Wook Park from Concordia University helped me in preparing the instrumentation equipments and drove me many times to the remote construction site under all kinds of weather conditions. My colleague Brendan O'Neill consistently works closely with me in analyzing the thermal performance and commissioning of the automation of the house.

While realizing that the following list must be incomplete, I would like to thank in no particular order:

- My close friends and colleagues Eleni Mouriki, Costas Kapsis, Liam O'Brien, Brendan O'Neill, Leanne Robinson, Caroline Hachem, Jose Candanedo, Kwang-wook Park and Luis Candanedo for their encouragement and help, and for accepting absences of social contacts on my part,

- Brendan O'Neill, Liam O'Brien, Leanne Robinson and Caroline Hachem for carefully proofreading the manuscript and giving me helpful writing suggestions,

- Jose Candanedo for sharing his knowledge in heat transfer modeling and TeX typesetting,

- Kathy McAleese, Lyne Dee and Meli Stylianou for their administrative assistance,

- Xiaolin Gao for her love, understanding and patience,

- Gabriel Miclette and his mother Monique Daoust, for their tremendous moral support. They have provided me a home away from home.

Finally, I sincerely want to thank my mother, Zhuanying Liang, my father, Junfa Chen, and my sister, Minhua Chen, for their endless love and continuous financial support. I would like to dedicate this work to them.

Financial support of this work was provided by Natural Sciences and Engineering Research Council (NSERC) of Canada through the Solar Buildings Research Network (SBRN). The BIPV/T system was funded through the TEAM (Technology Early Action Measures) program of Natural Resources Canada (NRCan). Canada Mortgage and Housing Corporation (CMHC) conducted the demonstration program. Hydro Québec participates in monitoring the house.

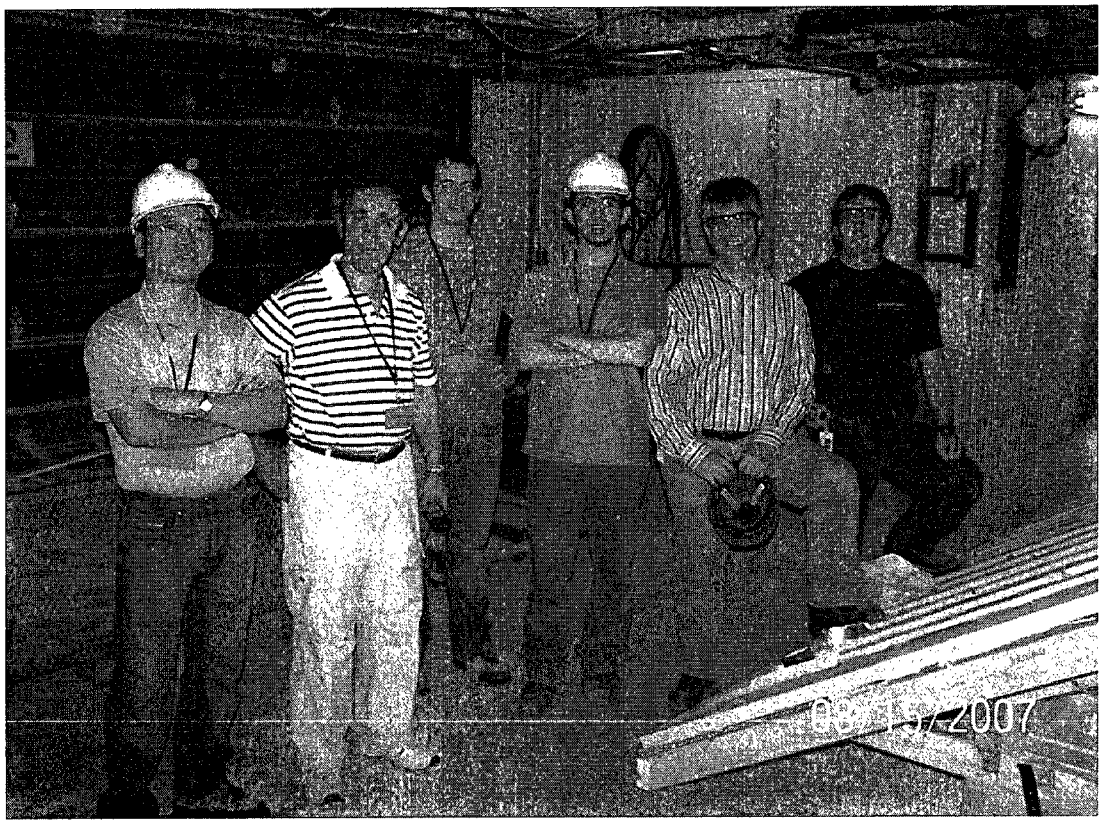

From left to right: Dr. Kwang-Wook Park, Dr. A. K. Athienitis, Brendan O'Neill, YuXiang Chen, Bradley Berneche (president of Alouette Home) and Jean Ardouin

Left: Nicole Laberge (project manager) and Jean Ardouin (construction manager)

书山有路勤为径,

学海无涯苦作舟.

There is no royal road to learning.

唐·韩愈

Yu Han, Tang Dynasty, China

Contents

List of Figures

List of Tables

Nomenclature

$A_{pvt.ncs}$	net cross section area of BIPV/T normal to air flow
D_h	hydraulic diameter
GWh	gigawatt hour
$T_{PVT.air.out}$	BIPV/T system outlet air temperature
c	material specific heat $[J/(kg \cdot K)]$
$h_{c.pvt}$	CHTC inside BIPV/T air cavity $[W/(m^2 \cdot K)]$
$h_{c.r}$	combined convective and radiative heat transfer coefficient $[W/(m^2 \cdot K)]$
$h_{c.vcs}$	CHTC inside VCS air channel $[W/(m^2 \cdot K)]$
$h_{c.wd}$	wind-induced external CHTC on roof $[W/(m^2 \cdot K)]$
k	material conductivity $[W/(m \cdot K)]$
kWh	kilowatt hour
k_{cnc}	concrete conductivity $[W/(m \cdot K)]$

Acronyms

ACH	air changes per hour
BIPV/T	building-integrated photovoltaic/thermal
CFD	computational fluid dynamics
CFM	cubic feet per minute
CHTC	convective heat transfer coefficient $[W/(m^2 \cdot K)]$

COP	coefficient of performance
DHC	diurnal heat capacity
DHW	domestic hot water
GFA	gross floor area
GSHP	ground source heat pump
HRV	heat recovery ventilator
HVAC	heating, ventilation and air conditioning
HX	heat exchanger
PV	photovoltaic
PV/T	photovoltaic/thermal
R	resistance in imperial unit $[ft^2 \cdot F \cdot hr/Btu]$, R 1 = RSI 0.176
Re	Reynolds number
RSI	resistance in SI unit $[m^2 \cdot K/W]$, RSI 1 = R 5.678
TC	thermocouple
TES	thermal energy storage
VCS	ventilated concrete slab

Greek Symbols

α	solar absorptance
ρ	material density $[kg/m^3]$

Subscript

cnc	concrete
pvt	photovoltaic/thermal
vcs	ventilated concrete slab

Chapter 1

Introduction

In Canada, about 17% of the total annual national energy demand is in the residential sector[1] (in 2006, about 3.74×10^5 GWh and 233 kWh/m^2)[2]. Of the annual energy consumption, more than 78% was used for space and domestic hot water (DHW) heating[2] (Figure 1.1). Hence, if reduction in residential energy consumption is desired, reducing the energy consumption for space and DHW heating is critical. Applying solar heating technologies in these two areas can greatly reduce heating fuel consumption of Canadian homes [Hastings and Mørck, 2000; Athienitis and Santamouris, 2002; Eicker, 2003].

The study of an integrated solar/structural system, a building-integrated photovoltaic/thermal (BIPV/T) roof coupled with a ventilated concrete slab (VCS), in an built demonstration house[3] will be presented in this thesis. This integrated system serves to reduce the heating energy consumption of the house. The data from field

[1]Statistics Canada, Energy supply and demand data. `www40.statcan.gc.ca/l01/cst01/prim71-eng.htm`

[2]Natural Resources Canada, residential end-use model, 2008. `www.oee.nrcan.gc.ca/corporate/statistics/neud/dpa/tablestrends2/res_ca_2_e_3.cfm?attr=0`

[3]Although this was a team effort involving several students and other professionals, the author played a key role. He participated in the design process, instrumentation, and monitoring of the house.

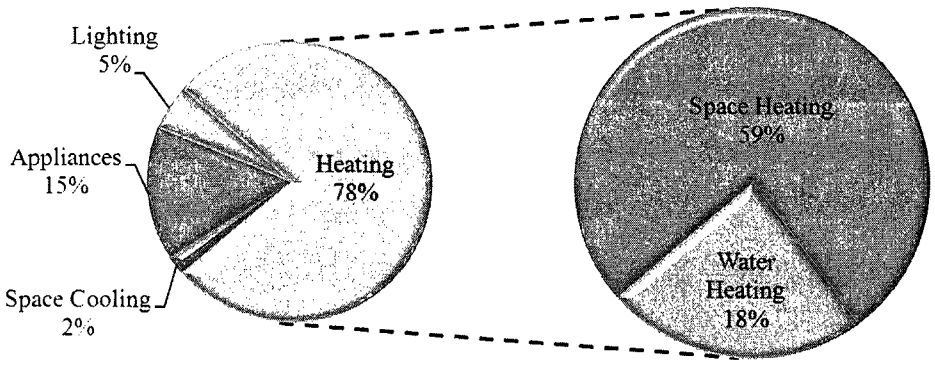

Figure 1.1: Shares of secondary energy use in Canadian residential sector for year 2006[2]

operations, the assessments of the thermal performance, and the simulation models are presented.

1.1 An Integrated Energy System: ÉcoTerra

Figure 1.2: ÉcoTerra, November 2007

Canada Mortgage and Housing Corporation (CMHC) launched a demonstration initiative "EQuilibrium Housing" in 2006. Its goal is to promote healthy and low energy homes. As one of the twelve selected demonstration houses across Canada, ÉcoTerra (Figure 1.2) was designed and built in 2007 by Alouette Homes, a prefabricated home manufacturer. Canadian Solar Buildings Research Network (SBRN) assisted with the design of the house. ÉcoTerra is designed to achieve annually close to net-zero energy consumption. This goal is achieved by significantly reducing the space and DHW heating energy consumption through the optimal integration of conventional and advanced heating technologies. These include a geothermal heat pump, a BIPV/T roof[4], an active thermal energy storage (TES) system - VCS, and passive solar design (Figure 1.3). A supervisory control system is used to optimize the overall performance of this integrated energy system. The main adopted technologies are briefly described as follows:

- A BIPV/T system is integrated into the south-facing roof. It converts solar irradiance to electricity and, at the same time, collects thermal energy from the photovoltaic (PV) panels, thus cooling them down. When the temperature of the PV panels exceeds a certain level, outdoor air is drawn underneath them to extract the excess heat from them. The collected heat can be used for space and DHW heating, as well as clothes drying.

- A VCS is thermally connected to the BIPV/T system. In the heating season, it serves as an active TES system to store part of the collected thermal energy from the BIPV/T system and release it passively into the living space to assist space heating. The VCS slab may also be used for night cooling in the summer.

- Large south facing, triple-glazed windows and distributed thermal mass (e.g. concrete walls and slabs) are employed for passive solar design.

[4]The prototype of this BIPV/T roof is developed by Athienitis and his research team[Pantic, 2007]

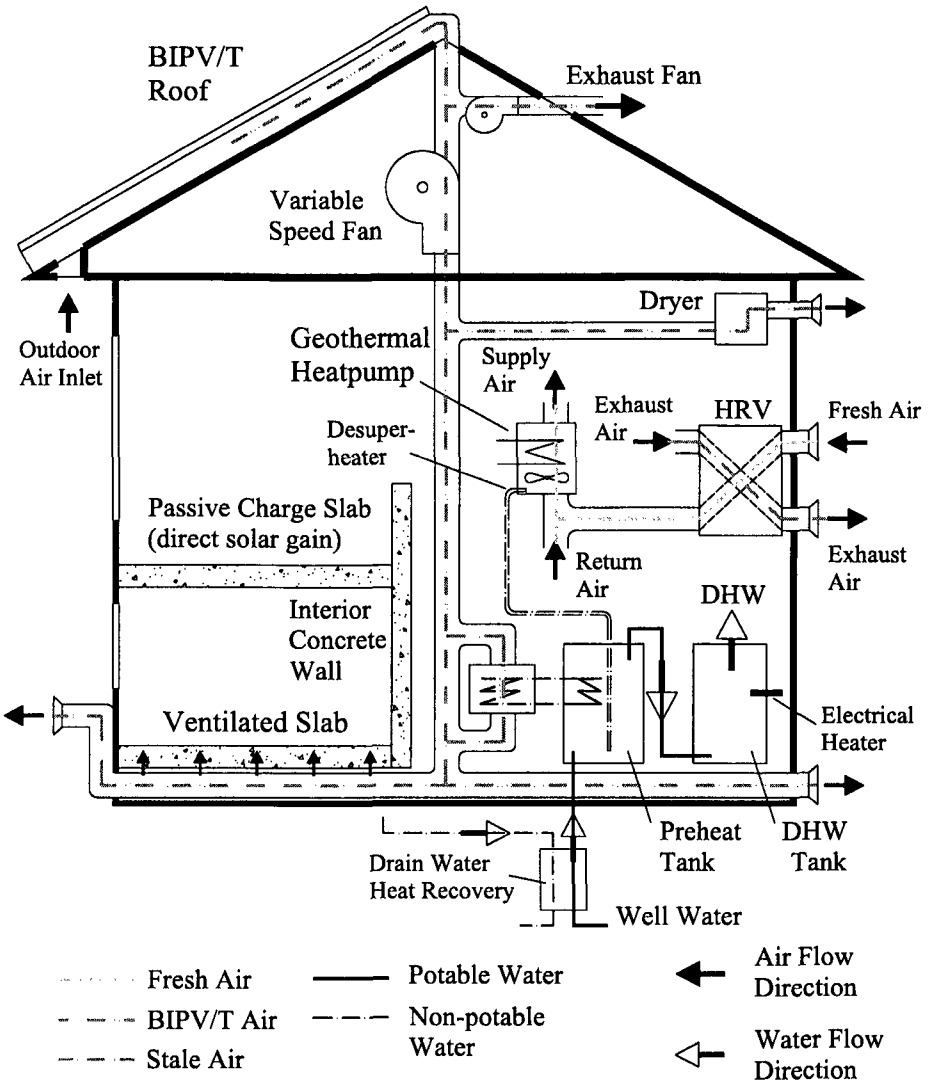

Figure 1.3: Schematic of the integrated mechanical system in ÉcoTerra

1.2 Building-Integrated Photovoltaic/Thermal System

In building-integrated photovoltaic (BIPV) systems, PV panels act as an integrated part of the building envelope. This enhances the architectural appearance of the building and avoids occupying extra land which is required for a free standing PV system. However, one major problem with BIPV systems is overheating [Bazilian et al., 2001; Krauter et al., 1999]. When the solar incident angle is small, about

85% of the solar irradiance is absorbed by the PV panels. The exact value depends mainly on the absorptance of the surface material and the surface conditions, such as cleanness [Duffie and Beckman, 2006]. About 5 to 15% of the absorbed solar radiation can be converted to electricity, depending primarily on the type of PV cell and its operating temperature. The rest of the absorbed solar radiation (roughly 70% of the total solar irradiance) becomes heat. If proper cooling (e.g. natural or mechanical ventilation) is not provided, overheating will occur. Overheating will reduce the efficiency of the electricity generation and shorten the lifespan of the PV panels [Duffie and Beckman, 2006]. This heat may be extracted and collected for space or DHW heating purposes whilst reducing the problem of PV panel overheating. The benefits are two-fold. In this case, the system is called BIPV/thermal (BIPV/T) system.

The collected heat, depending on temperature, could be used in a variety of applications. If this heat is collected for space heating, the excess portion of this heat can be stored in thermal mass, such as concrete slabs, for later use (e.g. at night). This way the useful amount of collected heat is maximized and, at the same time space overheating is avoided. Figure 1.3 shows the concept of a roof-mounted air-based BIPV/T system as installed in ÉcoTerra. A heat transfer fluid, air in this case, is drawn underneath the panels to extract the heat.

In building applications, solar thermal collectors can be mounted on the south-facing facades and roofs to actively collect additional solar thermal energy. In these cases, BIPV/T systems can be used to replace some or all the conventional solar thermal collectors. Due to the desire for low operation temperatures to increase the electricity production of the PV panels, the outlet temperature of the heat transfer fluid cannot be as high as that from conventional closed loop solar thermal collectors.

Besides replacing conventional solar thermal collectors, BIPV/T systems integrate

PV into the building envelope. This integration can replace conventional building envelope materials. Furthermore, a BIPV/T system is a cogeneration system, producing heat and electricity at the same time. Overall solar energy use is increased. These advantages reduce the balance-of-system[5] cost of the PV system [Bazilian et al., 2001].

1.3 Ventilated Concrete Slab

A ventilated concrete slab (VCS) uses the structural mass as active thermal storage. The main function of thermal mass in building applications is to lower peak loads for space conditioning (heating or cooling) by storing and releasing a considerable amount of thermal energy (heat or coolness) at a desirable rate. This section will at first discuss the importance of the thermal mass in buildings and the characteristics required. Then, the reason of using concrete slab as thermal mass will be explained. Finally, the advantages of using VCS will be presented.

1.3.1 Thermal Mass in Buildings

Ancient civilizations realized the ability of thermal mass to moderate daily room temperature swings year-around, preventing overheating in the summer and assisting heating in the winter. Massive pueblos[6] were made of hand-formed masonry called adobe, which is typically 50 to 60 *cm* thick. This simple thermal mass and insulation served the occupants well by buffering their living spaces year-round [Howard and Fraker, 1990]. These adobe houses are a typical application of passive thermal mass.

[5]The balance-of-system (BOS) encompasses all components of a photovoltaic system other than the photovoltaic panels. (Source: US Department of Energy. `www.eere.energy.gov/solar/bos.html`)

[6]Houses of Native Americans in the southwestern USA

In the areas of northern China and the Korean peninsula, traditional houses are usually constructed with mud walls thicker than 50 cm. One valuable invention is the big brick block called a "Keng" inside this kind of house. The "Keng" serves as a place for sitting or sleeping on. The normal dimension is about 0.7 m high, 2 m wide, and as long as the room in which it is located. It is assembled with bricks, but with a small cave inside for lighting a fire. The brick, serving as thermal mass, stores the intensive heat from the fire lit inside the cave, holding it over a long time (6 to 12 hours), and releasing it slowly to the living space.

Today, it is generally accepted that incorporating thermal mass into buildings and houses will greatly improve the thermal performance of buildings as follows:

- Thermal mass buffers and moderates (by absorbing and releasing thermal energy) the effects of ambient conditions (outdoor air temperature through infiltration, transmitted solar radiation, internal heat gain, etc.) on the indoor operative temperature [ASHRAE, 2005] (i.e. the collective effect of air and radiant temperature). This reduces the temperature swing's magnitude and frequency, and hence improves thermal comfort.

- Thermal mass can be incorporated in active or passive thermal energy storage (TES) such as building pre-heating or -cooling. By storing thermal energy in the thermal mass when the source is available, or when the utilization efficiency is higher, and then retrieving this stored thermal energy later, the building can be partially or even completely thermally naturalized (i.e. the operative temperature is maintained at a comfortable level; no auxiliary heating/cooling is needed). For example, night time building pre-cooling using outdoor cool air has been successfully used in practice [Winwood et al., 1997d; Standeven et al., 1998; Braun, 2003].

- The peak cooling or heating requirement can be reduced and delayed due to the

above-mentioned points. Reducing the peak demand will lead to a reduction in heating, ventilating, and air-conditioning equipment capacity. Reduced equipment capacity can represent energy, operation and construction cost savings. Delaying, and hence staggering the peak-load periods of individual components or buildings, can reduce the community's peak demand. Peak demands distort the ability to match generating capacity to average demands.

There are many different ways that thermal mass can participate in storing and releasing thermal energy. In other words, the thermal mass can be thermally coupled to its environment in different ways. The most common case is that the thermal mass stores and releases thermal energy passively, such as in the mass of furniture, structural components, etc. For example, a massive floor in a direct gain zone[7] can absorb the transmitted solar radiation and release the thermal energy later into the living space [Athienitis and Santamouris, 2002]. Thermal energy can also be stored in and retrieved from thermal mass by mechanically driving heat transfer fluid. For example, in solar hydronic space heating systems, water in the tank is used to store heat from the solar collector. The stored heat is released to the living space by circulating the warm water to radiators. In some other cases, thermal mass can be both passively or actively charged and then passively or actively discharged. For example, a ventilated slab in the direct gain zone can be passively charged by the transmitted solar radiation and actively charged using the heat from solar thermal collector, either at the same time or different time, by the heat transfer fluid flowing through its cores.

The heat transfer rate between the thermal mass surface and its surrounding environment plays a vital role in the functioning of the thermal mass. For example, a thermal mass that is directly exposed to solar radiation can collect solar energy quickly. But

[7]The space that first receives the transmitted solar radiation in the passive solar space heating condition

for thermal mass that is only convectively coupled, the TES is achieved mainly by natural convection and long wave radiation. Increasing the TES efficiency (e.g. the heat transfer rate, or storing time) and, consequently, maximizing the amount of energy that can be stored will result in an increased utilization effectiveness of the thermal mass.

The thermal conductivity should be high enough in the thermal mass to allow thermal energy to "penetrate" deep into the storage material. This will increase the thermal energy storing efficiency. Materials with high conductivity values, such as metal, however, should be avoided because high conductivity will shorten the time lag for heat delivery/release [ACI Committee 122, 2002]. Specific heat (measured in $J/(kg \cdot K)$) and heat capacity (measured in $J/(m^3 \cdot K)$) should be high to maximize the amount of energy that can be stored in a given amount of material. Materials with high thermal diffusivities (conductivity divided by heat capacity, measured in m^2/s)) are more effective at heat transfer than heat storage. Therefore, materials with low thermal diffusivities are desirable for storing solar energy.

When the thermal mass is exposed to interior space, there are certain requirements for its optical characteristics. The choice of the optical properties is also related to the heat distribution in the building interior. In a passive solar application, the mechanisms of heat distribution within a direct gain zone, after short-wave solar radiation has entered through the window, are very complex. The basic rule is that surfaces within the direct gain zone, with the exception of the floor, should be light in color [Balcomb, 1983]. This is valid for both lightweight and massive elements. Light-colored surfaces can aid in the distribution of thermal energy and daylight to all surfaces of the room. By making the surfaces light in color, short-wave solar radiation is more liberally scattered throughout the space. Light surfaces, especially matte white surfaces, greatly aid in daylight distribution. However, if the floor is

massive and is in direct gain zone, it should not be light in color (see Section 1.3.2). The absorptivity "α" of nonmetallic material is a surface effect largely dependent on surface color, and is roughly [Balcomb, 1983]:

$$\alpha = \begin{cases} 0.8 \sim 0.9 & \text{very dark surfaces} \\ 0.5 \sim 0.6 & \text{most surfaces} \\ 0.3 \sim 0.4 & \text{light colored surfaces} \end{cases}$$

The location, shape and quantity of the thermal mass are important factors and interrelated. In order to maximize the utilization of thermal mass, they must be considered simultaneously. For example, when a concrete slab is located in the direct gain zone to absorb the transmitted solar radiation and store it as heat, the slab has to be at the place of first incidence. Instead of being thick and having small surface area, it would be much better to be thin and have a larger surface area. If the slab is too thin, there will be overheating on the top surface and not much heat can be stored [Athienitis and Santamouris, 2002]; while, a too thick slab will increase the building's structural load and take up interior space.

Solar buildings represent a specialized application of thermal mass for solar heat storage, retention, and release. Thermal mass plays a very important role in the good building thermal performance. The intensive heat gain from solar radiation, such as transmitted solar radiation through glazing or heat collected from solar thermal collectors, needs to be buffered and stored in order to be used at an appropriate rate.

1.3.2 Concrete Slab as Thermal Mass

Due to its inherent structural functionality and the availability of raw materials used in its production, concrete is the world's most widely used building material. Concrete is also well known as an excellent material for thermal mass.

Among common building materials, commonly used normal-weight concrete matches the thermophysical requirements for thermal mass: relatively high conductivity compared to non-metal material (about 1.9 $W/(m{\cdot}K)$), high density (about 2300 kg/m^3), high specific heat capacity (about 900 $J/(kg \cdot K)$), and relatively low thermal diffusivity (about 9×10^{-7} m^2/s) (C.1). If the material's capacity for thermal energy retention and release is considered in a dynamic (i.e. time-related) way, the diurnal heat capacity (DHC) concept by Balcomb [1983], also shows that concrete is a very good thermal mass material.

The thermal conductivity of concrete varies in a large range primarily depending on its aggregate type mixture and density. Using quartzite as aggregate will give concrete higher thermal conductance "k_{cnc}". Further, the higher density (higher aggregate volume fraction) gives much higher k_{cnc}. Moisture content also affects concrete's thermal conductivity. Higher moisture content results in higher k_{cnc}.

For optical properties, the total hemispherical emissivity of rough concrete surface is about 0.91; meanwhile, its solar absorptivity is about 0.6 [ASHRAE, 2005, Ch. 3]. Rough-textured surfaces provide more surface area for collection of solar energy than smooth surfaces, but this advantage in solar energy collection has not been thoroughly investigated. In cases where concrete slab is used as thermal mass in direct solar gain applications, the high solar absorptivity of the concrete maximizes the amount of solar energy that can be absorbed. At the same time, its high-emissivity characteristic enables efficient re-radiation of the stored energy into the occupied space [ACI Committee 122, 2002].

The main advantages of choosing concrete slabs as thermal mass, in terms of location, shape and quantity, are as follows:

- When a large window area is adopted in order to receive more direct solar radiation as heat source, a massive and effective thermal mass must be placed

at the place of first incidence to absorb this transmitted solar radiation. If a large portion of the transmitted solar radiation is reflected and re-distributed instead of being absorbed, space over-heating can occur. Because the floor surface is often the place of first incidence, a massive floor in medium dark color (e.g. exposed concrete) should be used.

- In concrete-structure buildings, the slab is the largest portion (in volume or weight) of the mass of the structure. An abundant amount of thermal mass is already available for use. A large amount of energy can be stored for only a small variation in temperature.

- The concrete slab is evenly distributed over the floor and it is already, or can be easily exposed to interior air. An example of this is a ceramic floor and an exposed ceiling (i.e. no suspended ceiling). This enables the concrete slab to absorb and release thermal energy directly and evenly into the indoor living space. This also means the slab can be used for radiant floor heating or cooling.

- Indoor thermal discomfort is normally caused by the warm-head-and-cool-feet situation, due to vertical air temperature stratification ([ASHRAE, 2004] & [ASHRAE, 2005, Ch. 8]). Maintaining heat storage at the floor level or using radiant floor heating can counteract the inevitable tendency for stratification.

- Using concrete slabs for TES is using the building's structure as thermal mass. This will not occupy extra living space nor block the outdoor view of occupants. In some cases, trombe walls[8] are placed close to transparent envelope portions, like windows and transparent insulation, to absorb and store solar energy. In such cases, outdoor views and indoor living space are sacrificed.

The thermal and optical characteristics of concrete together with a slab's suitable

[8] A sun-facing wall built from material that can act as a thermal mass

location and shape define the advantages of using structural concrete slab as thermal mass.

1.3.3 Ventilated Concrete Slab

When a thermal mass is coupled to indoor air through a natural convection mechanism only, the effectiveness of heat transfer is relatively low due to the facts that the heat transfer is restricted by the free surface area, the controls over the heat exchange and the thermal mass temperature are limited, and the heat transfer coefficient by natural convection alone is relatively poor. Heat transfer by natural convection is relatively slow compared to forced convection. For example, on a horizontal surface, the natural convection heat transfer coefficient (CHTC) is only about 3 to 5 $W/(m^2 \cdot K)$ and forced convection can typically achieve values five times higher CHTC [ASHRAE, 2005, Ch. 3]. These drawbacks lead to the idea of using concrete slabs as active TES systems.

In active TES systems, the thermal mass is mainly charged (i.e. storing thermal energy) actively. Heat transfer fluids are driven through the internal space of the thermal mass to exchange heat with the thermal mass. For example, forced warm air passes through the rock bed. Existing practices of active TES system using concrete slab include hydronic radiant heating floor [Athienitis and Chen, 1993], TermoDeck^{TM} systems (Section 2.2.4), etc.

A VCS is an active TES system. In VCS, air is circulated into the hollow cores of the slab by a fan. Mechanical ventilation can employ forced convection. Using the hollow cores of the concrete slab for heat exchange means more effective thermal mass and a larger heat transfer area can be utilized. Thus, less time is needed to charge the thermal mass and more energy can be stored in the thermal mass. By using VCS, the storage efficiency and effectiveness are increased. The thermal coupling between

the structural mass and the thermal energy source is enhanced.

Another advantage of using VCS emerges when forced-air solar thermal collectors (e.g. BIPV/T system) are adopted. The heated outlet air can be passed directly through the VCS. VCS stores the thermal energy collected from the air and releases it later passively or actively into the living space. The necessary supply air temperature for heating the VCS could be just slightly (about 3 to 10°C) higher than the slab temperature which is close to room temperature. That means a large amount of air at a relatively low but useful temperature can be utilized. A BIPV/T system can provide this heated air.

1.4 Objective and Scope of the Research

This thesis presents a study on an integrated system - VCS-BIPV/T: an innovative ventilated concrete slab (VCS) coupled with a building-integrated photovoltaic/thermal (BIPV/T) system, in an energy efficient solar home named ÉcoTerra. The main objective of this study is to quantify the VCS-BIPV/T system's capability and effectiveness of using the structural mass as active TES system to store the collected solar thermal energy to assist space heating. The following is a summary of the content of the thesis:

- Chapter 1, Introduction, briefly presents the background, the motivation and the objective of this research.

- In Chapter 2, Literature Review, the related work on photovoltaic/thermal (PV/T) systems and thermal storage systems from literature will be reviewed, with focus on the research and development in utilizing building structural mass as active thermal mass.

- Chapter 3, Design and Thermal Performance of a Solar House with a VCS-BIPV/T system, describes the design concepts, building characteristics, and the preliminary thermal performance of ÉcoTerra.

- Chapter 4, BIPV/T System, presents a comprehensive study on the BIPV/T system installed in ÉcoTerra, including the design philosophy, data from field operations, assessment of thermal performance, and modeling. A brief discussion on the wind-induced CHTC is also presented.

- Chapter 5, Ventilated Concrete Slab, has the similar topics to Chapter 4, but the object presented is the VCS instead of the BIPV/T system.

- Chapter 6, Conclusions, summarizes and discusses the important findings from the previous chapters.

- In the appendices, additional selected information related the ÉcoTerra project, the BIPV/T system and the VCS, such as the construction details, future improvements, the thermophysical properties of concrete material, are included.

Chapter 2

Literature Review

This chapter reviews the related literature on photovoltaic/thermal (PV/T) systems and thermal energy storage (TES) systems. The research and development in utilizing building structural mass as active thermal mass is the main focus. Section 2.1, BIPV/T Systems, presents the review on the advantages of PV/T or building-integrated (BI) PV/T systems in energy generation and the modeling of their thermal performance. In Section 2.2, Thermal Mass, literature related to the studies of thermal mass and TES systems will be explored. The studies, assessments, and modeling of the thermal performance of the thermal mass and the related contribution to the improvement of the thermal performance of the buildings are included. The review in this chapter also provides important information on critical design aspects on the PV/T systems and the active TES system.

2.1 BIPV/T Systems

One of the main studies of this thesis is the use of PV/T or BIPV/T systems to generate energy. In the following review of literature, previous studies of PV/T

or BIPV/T systems will be presented. These reviews emphasize the advantage of PV/T or BIPV/T systems and provide important information for their design and modeling.

Bazilian et al. [2001] carried out a broad survey on the existing built examples and current research regarding BIPV cogeneration systems which are generating electricity and recovering the by-products, such as heat and daylight, from the BIPV systems. An evaluation method was presented which examines the energy and economic performances of BIPV cogeneration systems. The authors concluded that BIPV cogeneration systems, which produce both electricity and utilize the thermal energy by-product at the same time, have higher efficiencies than BIPV systems that generate electricity only. Later, Bazilian et al. [2002] conducted a thermographic analysis on a BIPV/T system. The analysis helps with the interpretation of the surface emissivities and operating temperatures, as well as qualitative graphical analysis of temperature gradients. Almost in the same period, Bazilian and Prasad [2002] created a numerical model for use as a design tool for BIPV/T systems. The numerical model is validated with experimental data.

Charron and Athienitis [2006a,b] conducted detailed theoretical and experimental studies on double facades with integrated PV panels in two different configurations. In the first configuration (#1), the PV panels were placed on the front surface and in the second configuration (#2), the PV panels were placed in the middle of the cavity. In their first paper [Charron and Athienitis, 2006a], a one-dimensional finite difference thermal model was developed for theoretical study. They found that configuration 2 has an increased combined (thermal-electric) efficiency, but lower electricity generation when compared with configuration 1. In their second paper [Charron and Athienitis, 2006b], a two-dimensional control-volume finite difference thermal model was created. Good agreement with a one-dimensional analytical model

was observed. They further concluded that the values of the convective heat transfer coefficient (CHTC) from the literature are generally lower than those observed in their experiments. Experiments conducted showed a considerable amount of heat can be recovered and collected in the double-facade systems.

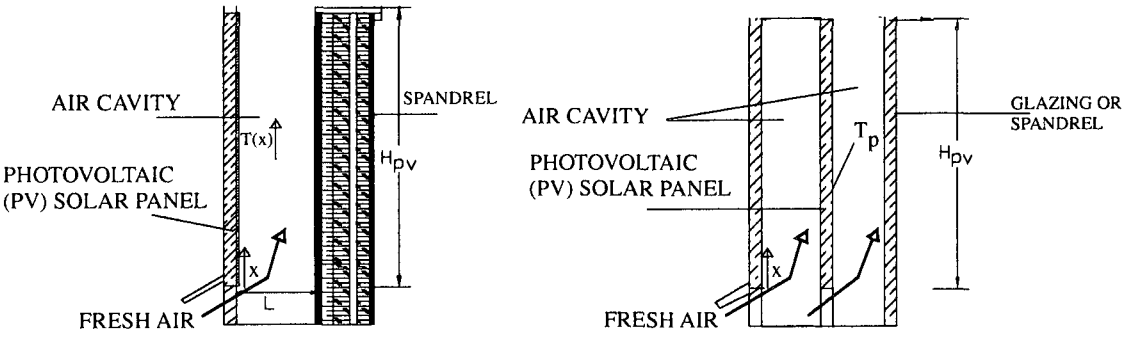

(a) Configuration 1 (b) Configuration 2

Figure 2.1: Double facades with integrated PV/T systems [Charron and Athienitis, 2006a]

Later, Liao et al. [2007] performed a computational fluid dynamics (CFD) study on configuration 1 [Charron and Athienitis, 2006a]. The fluid flow generated from their CFD model was partially validated with the data obtained by a particle image velocimetry[1] (PIV) system. The temperature profiles from the CFD model had good agreement with experimental data. Local and average CHTC were generated from the CFD model, as were the correlations.

Krauter et al. [1999] performed experiments to compare the thermal performance of a PV facade system under three different heat extracting configurations. The findings were: 1) active ventilation of conventional PV facades allows a reduction of cell operation temperatures by up to 18 °C at an air speed of about 2 m/s; 2) cell temperature increases by 20.7 °C for thermal insulating PV facade elements without cooling; and 3) a hybrid thermal insulating PV facade element combined with a water cooling system lowers the operating cell temperature by 20 °C.

[1] An optical method used to measure velocities and related properties in fluids

2.2 Thermal Mass

Thermal mass plays an important role in the thermal performance of buildings, especially in solar buildings. Maximization of the effectiveness of the thermal mass and the TES system have been being studied over three decades.

2.2.1 Thermal Mass in Buildings

The American Concrete Institute's guide "ACI 122R02" [ACI Committee 122, 2002] presents the thermal-property data and design techniques that are useful in designing concrete and masonry building envelopes for energy code compliance. This guide provides detailed information on the thermal properties of the building envelope and the materials that comprise the envelope system. Essentially, the use of concrete, and its inherent thermal capacitance, helps the design of energy-conserving buildings.

In the guide, information about the physical properties (e.g. density, conductivity, and etc) of all kinds of concrete (e.g. different aggregate types, different volumetric percentage, etc) is presented. The measurement and empirical calculation methods for obtaining conductivity are presented. The guide also presents studies that analyzed the effect of thermal mass of concrete and masonry exterior walls on the thermal performance of buildings. It quantifies the thermal lag effect induced by different kinds of concrete and masonry envelopes. The guide points out that concrete and masonry buildings containing large thermal mass have lower annual heating and cooling loads than other similarly insulated buildings. In the end, the advantages of the thermal properties of concrete and masonry for passive solar design are discussed. The guide emphasizes that "concrete and masonry materials fulfill all of the requirements for effective thermal storage in passive solar applications. These materials have been used with great success in passive solar buildings to store the collected

solar energy, prevent overheating, and re-radiate energy to the interior space when needed."

Zhang et al. [2006] conducted a theoretical study on the ideal thermophysical properties of a building envelope using a simplified numerical model. Their numerical model was verified with experimental data. They concluded that the higher the thermal capacity (i.e. the product of density "ρ" and specific heat capacity "c") of the material of the internal wall, the less energy is consumed for cooling/heating. The conductivity k of the internal wall layer does not have significant influence on the thermal performance of the buildings, but low k for the external wall layer is desired.

Braun [2003] reviewed the research related to the use of building thermal mass for shifting and reducing peak cooling loads in commercial buildings. He summarized the results from simulations, laboratory tests, and field studies. Braun pointed out that the opportunities for reducing cooling operation costs through the use of building thermal mass are due to four effects as follows:

- Reduction in peak demand costs;
- Use of low cost off-peak electrical energy;
- Reduction in mechanical cooling resulting from the use of cool night-time air for ventilation pre-cooling;
- Improvement of mechanical cooling efficiency due to increased operation at more favorable part-load and ambient conditions.

However, Braun states that the savings are sensitive to many factors, including utility rates, type of equipment, occupancy schedule, building construction, climate conditions, and control strategy.

One interesting point noted by the author is that in typical office buildings, internal gains are on the order of 0.03 to 0.07 kW/m^2 GFA. The thermal capacity of a typical concrete building is on the order of 0.08 to 0.12 $kWh/(m^2 \cdot K)$ GFA. Thus, for an internal space, the energy storage is on the order of 1 hour for every 0.5 °C of pre-cooling of the thermal mass. In other words, for counteracting 1-hour internal heating gain, the structural mass needs to be cooled down by 0.5 °C.

2.2.2 Thermal Mass in Solar Applications

Athienitis and Santamouris [2002] presented comprehensive studies on the thermal mass in solar applications. They presented thermal analyses and modeling techniques on the thermal performance of the thermal mass, including the analytical solution approach, the admittance method, the explicit finite difference approach, and the thermal network concept. Based on their thermal analysis, design guidelines are provided for the sizing of the thermal mass and the fenestration, as well as the design and control of TES systems. They noted that all components of the solar buildings are inter-related and should be treated as an integral system in order to maximize the utilization of solar energy and enhance thermal comfort.

Balcomb [1983] introduced the concept of "diurnal[2] heat capacity" (DHC). It is the amount of heat that can be stored in building thermal mass during the first half of a 24-hr cycle and returned to the space during the second half of the cycle. DHC is a measure of the ability of the wall/floor to absorb and store heat during one part of a periodic 24-hr cycle and then to release the heat back through the same surface during the second part of the cycle. The author concluded that among three time domains of heat storage (short-term: a few hours, diurnal, and long-term: longer than one day), diurnal heat storage is the most significant to passive solar design. If one

[2]24-hr cycle

designs on the basis of diurnal storage, long-term storage will usually be adequate. The author provides the numerical methods of DHC analysis. The DHC method provides a useful measure of the heat storage capacity of a whole room or a whole building during periodic clear-day weather. After the DHC of the whole room or the whole building is obtained, the peak-to-peak room temperature swing in the direct gain space can be estimated with a simple calculation, and it is proved to be in good agreement with the author's simulation analysis.

After the DHC concept, Balcomb discusses the effectiveness and prediction of convection for transferring heat to a remote space either through single doorways or through interconnected building spaces. The author pointed out that convection through doorways is a very effective way of heating remote rooms. It is evident that a major amount of the thermal storage in a remote room is due to convection from the direct gain zone[3]. The major driving mechanism for this convection is the heat engine - driven by the sun on one side and by walls absorbing heat on the opposite side. Balcomb also provided design guidelines for convective loops and formulations for convection heat flux through doorways and room-to-room temperature difference.

Balcomb [1983] summarized the design guidelines for thermal mass in passive solar heating. He emphasized that "all the guidelines lead strongly to one conclusion: if there is a limited amount of mass that can be put in space, it is much better to spread the mass thinly to achieve as large a surface area as possible".

The MIT press series *Solar Heat Technologies: Fundamentals and Applications* [Bankston, 1990-1997] provides comprehensive and detailed information about solar heat technologies that were investigated in the 1970's and 1980's. This series includes the fundamental physics, the review of research and development, and also the monitoring results of the existing practices.

[3]The space firstly receives the transmitted solar radiation in the passive solar space heating condition

In one book of this series, Franta [1990] addressed the significant impact of the thermal energy distribution in building interiors (TEDBI) on the effectiveness of solar utilization, thus energy use, and thermal comfort of the occupants. The primary issues the geometry and the location of the thermal mass. The author concluded that "as energy became more of a concern through the use of conservation and solar applications, there was a desire to distribute thermal energy within buildings using as little power as possible. This resulted in designers attempting to distribute energy with buildings by natural rather than mechanical means". The author discussed some issues that were often overlooked or poorly understood by building designers and engineers, and provided a review of research and development on TEDBI between 1972 and 1982. One of them is the *3-dimensional natural convections at high Rayleigh number* in building interiors by Solar Energy Research Institute (SERI).

In another book of this series, edited by Balcomb [1992], the evolution of research, demonstration projects, and design competitions concerned with the building integration of passive system (e.g. pass thermal mass) is reviewed. This book also summarized the monitoring and results, primarily in the US from 1969 to 1987, for full-size passive solar residential and commercial buildings. These activities ranged from detailed heat transfer studies to monitoring programs that investigated the energy-consumption characteristics and energy savings of passive buildings.

Hastings and Mørck [2000] presented their work and other researchers' work on the system characteristics and design guidelines of solar air heating system coupled with thermal mass. Rossi and Scudo [2000] described an ***open* collection loop with radiant discharge storage** system, where the air circulates, by natural or mechanical driving forces, through the thermal collector, the ceiling channels, the room space and then back to the collector. Filleux and Elste [2000] described a ***closed* collection loop with radiant discharge storage** system, where the air is circulated in a

closed loop through the collector to the storage and back to the collector. The TES considered here is active TES.

2.2.3 Concrete Slab as Thermal Mass

Howard and Fraker [1990] addressed TES techniques that are directly coupled to the interior space of buildings, typically the surfaces of the interior building's structural elements. They focused on the results from major research and development in this field over the 1970's and 1980's, such as using building based material and components as thermal mass, strategies for integrating TES into building interiors, etc. They emphasized some important factors needed to be considered in the design of a TES system:

- The interior design considerations of the owner or operator;
- The amount of storage required for good performance and comfort with respect to the climate energy source;
- The frequency and quantity of internal heat gains supplied or generated by occupants, lights, equipment, and appliances.

Classic "rules-of-thumb" by E. Mazria and the Diurnal heat capacity (DHC) method from Los Alamos National Laboratory (LANL) - Solar Group (also see [Balcomb, 1983]) for TES design and analysis were briefly described by Howard and Fraker. Mazria provided heat storage guidelines for different generic passive system types. Homes designed with these rules performed fairly well; however, the application of these rules to multi-zone or internal-load-dominated commercial, industrial, or institutional structures were not very satisfactory. LANL's work showed that the optimal mass thickness of common construction materials can be determined by the

analysis of a materials' DHC. A basic finding of the DHC method is that the density and the specific heat of the storage materials have a major effect upon optimal thickness and effective storage capacity. An optimal storage material would have relatively high density and specific heat, and reasonable, but not excessive, thermal diffusivity. Thickness beyond optimal value (about 10 cm for lower density masonry material and about 18 cm for high-density materials [Balcomb, 1983]) has little added effect on diurnal heat storage.

Howard and Fraker [1990] also presented a discussion about the optimal ratio of the storage layer area to the glazing area in direct gain applications. A 6-to-1 storage-to-glazing area ratio is considered to be most effective if the mass is well distributed in the direct gain space. In standard construction (no added mass, insulated light frame walls), the solar glazing area should be less than 8% of interior floor area.

Bilgen and Richard [2002] presented their experimental and theoretical study on the impact of incident solar radiation on the transient thermal behavior of a concrete slab as listed below. Note that the temperatures in their experiments ranged from 28 to 62 °C, which is not in the range of indoor applications. However, the solar thermal characteristics of the concrete are expected to be similar in indoor temperature range.

- The ratio of the heat stored (total incident heat flux minus heat loss via radiation and convection) to the incident energy during the heating period decreases inverse-exponentially as a function of time. This ratio is not strongly affected by the intensity of the incident energy. The same trend applies to the ratio of the heat released from the slab surface at a various time to the heat released at the beginning of the cooling period. The major energy storage-restitution takes place during the first three to four hours. The radiation makes about 60% of heat loss while natural convection covers the rest.

- A numerical model was created and validated using experimental data. This

model is used in the sensitivity study on the thermophysical properties of concrete, including the emissivity, conductivity, density and specific heat. It shows that the influence of these parameters on the results, and in particular on the temperature of the slab, is negligibly small. Note that the sensitivity study on the thermophysical properties of the concrete only covers a relatively narrow range.

- The energy storage efficiency decreases from 74% at 2 hours after the beginning of the heating period to 35% at 12 hours after the beginning. Slab thickness and surface radiative properties can be used to optimize the thermal performance, such as thermal storage efficiency. Simulation shows that by changing the slab thickness from 10 cm to 20 cm, the energy storage density is increased by 30% and the thermal efficiency is improved by 6%. This comparison is made 6 hours after the beginning of the heating period in each simulation. Beyond this point, the amount of energy stored increases very slowly.

Shaw et al. [1994] conducted an experimental study on the effective utilization of building structural mass as a thermal regulator. At first, they studied the effect of a false ceiling on the thermal response of a work space. The work space had hollow core concrete slabs forming the ceiling and the floor. They concluded that false ceilings reduce the effectiveness of the thermal-mass effect of the ceiling concrete slab, and result in higher peak air temperature. The cooling load can be reduced if pre-cooling of the slabs is employed. However, simply exposing the building structure to the workspace provides limited heat storage capacity and hence, limits the structure mass' ability to regulate internal temperature.

Persaud and Symons [2006] presented their experimental results on a composite structural system consisting of timber beams and a concrete slab. The concrete slab considered is cast on profiled steel decking supported by the timber beams. The

beams and the slab are connected with shear connectors. Experimental tests show that the composite system has improved structural strength and efficiency. Their study indicates that using concrete-timber composite structure, thermal mass could be integrated into the structure of timber frame buildings.

Combining radiant floor heating and passive solar heating

Athienitis et al. [Athienitis and Chen, 1993; Athienitis, 1997; Athienitis and Chen, 2000] performed a series of experimental and theoretical studies on radiant floor heating with thermal storage. They addressed that "the key problem with the performance of a passive solar building with a floor heating system is overheating. This is due to the fact that, when a significant amount of solar radiation is incident on the floor, its thermal storage mass is already warm from continuous auxiliary heating input during the night and in the early morning". Their goal was to develop a methodology of thermal mass sizing and appropriate control strategies to achieve a reduction of operation cost, a decrease in heating equipment capacity, and the prevention of floor overheating. Athienitis and Chen [1993] stated the advantages of using radiant floor heating as follows:

- The combination of radiant floor heating and thermal storage offers the possibility of significantly improving building energy efficiency without compromising thermal comfort. It raises the mean radiant temperature due to the warm floor. Therefore, a lower room air temperature will provide the same thermal comfort level, resulting in reduced infiltration heat losses.

- Radiant floor heating is integrated into the building structure. It saves living and working space.

Their findings for electric floor heating with thermal storage are as follows:

- Proportional control results in improved thermal performance of the system with thermal storage compared to on/off control.

- The use of simple thermostat night setback (step change) contributes to energy conservation but often leads to a high increase (over 100%) in the peak heating load on cold days. Thus, a smoother setpoint profile with a ramp change is desirable. The ramping rate depends, to a large extent, on the amount of thermal storage and may be determined from simulations.

This work was later extended by Athienitis [1997]. The author presented a theoretical study of an integrated radiant floor heating - direct gain passive solar system. His numerical model is validated with experimental data and the direct solar gain effect is quantified in this study. The author's conclusions are listed as follows:

- Thermal mass in a floor heating system may be effectively employed for both storage of auxiliary supplied heat and direct passive solar gain.

- Efficient storage of passive solar gains in the thermal mass can be achieved by employing a lower setpoint at night followed by a smooth change to a higher setpoint during the daytime such as a half-sinusoid.

- Control of radiant heating based on the operative temperature provides better thermal comfort and reduces auxiliary energy consumption.

- For a concrete floor thermal mass integrated with a radiant heating system, a 10-cm thick slab causes a higher room temperature swing than 5-cm thick slab when high solar gains are present.

Athienitis and Chen [2000] employed a three-dimensional explicit finite difference model to study the effect of direct beam solar incident irradiance on the thermal

performance of a massive concrete floor with different flooring covers. Their model was validated with experimental data and the validation shows that the assumptions of uniform floor surface temperature and uniformly spread solar beam radiation are not accurate enough to reflect the local effect of the direct beam. Their study also showed that beam radiation will cause localized high temperatures as solar beam radiation can cause a local floor surface temperature in the illuminated area to be 8 °C higher than that in the shaded area. The study also demonstrated that carpets will obstruct the TES function of a massive floor, and also cause local high temperature. Partial carpet cover further increases floor surface temperature differences up to 15 °C when solar radiation is absorbed.

2.2.4 Ventilated Concrete Slab

Fort [2000] provided design guidelines for two kinds of active TES that can be integrated into solar air heating systems: **hypocaust** - a massive floor with channels through which warmed air is circulated, and **murocaust** - a massive wall with channels serving a similar function. For these two mentioned TES systems, the author described several design aspects:

- Type of air circulation: natural or forced convection;
- Type of discharge: passively by radiation or actively by forced air;
- Type of system loop: 1, open collect loop with radiant discharge, 2, closed loop with radiant discharge, and 3, closed loop charge with open loop discharge.

For various hypocaust types, Fort provided their respective characteristics, such as specific heat storage capacity, time constant, phase delay, and recommended range of air velocity. In conclusion, the author listed the following practical Do's and Don'ts:

- Size the hypocaust to cover the whole floor rather than make it the minimal size indicated by the calculations.

- Keep pressure drops low; duct connections are the most critical points.

- Use floor hypocausts as they may be better than wall nurocausts for distribution.

- Use murocausts in combination with hypocausts to help reduce ducting.

- Use ample thermal mass as it yields better distribution and may eliminate the need for sophisticated controls.

- Ensure air-tightness.

Braham [2000] reviewed independently published performance data of low-energy buildings using three types of various ventilation and TES strategies and their respective impact: Type 1, natural ventilation with exposed slab; Type 2, natural ventilation with core-cooled slabs; and Type 3, mechanical ventilation with core slab cooling. The analysis showed that using Type 3 with low-energy fans, circulating the ventilation air through the hollow cores of the structural ceiling or floor slabs before discharging into the occupied space, maximizes coupling HVAC loads with the thermal capacity inherent in the building's structural concrete. This enhancement is due to the following reasons:

- Improved heat transfer characteristics of turbulent heat flow within the center of the hollow-core slab.

- Higher thermal storage capacity due to the greatly extended air paths within the slab.

- A more predictable and controllable rate of energy transfer to and from the slab.

Using heat recovery mechanical ventilation in combination with thermal energy storage systems which use structural mass, the heating energy consumption can be easily reduced from typical values of $\geq 150\ kWh/(m^2 \cdot yr)$ GFA (Type 1: natural ventilation with exposed slab) to below 50 $hWh/(m^2 \cdot yr)$ GFA (Type 3: mechanical ventilation with core slab cooling). The Type 3 building considered in the study is the Elizabeth Fry Building at the University of East Anglia [Standeven et al., 1998] and in this example, TermoDeck (page 32) slabs are employed. The study demonstrates that low-energy mechanical ventilation systems incorporating efficient heat recovery and effective fabric energy storage[4] have higher year-round comfort criteria, and significantly lower prime energy consumption, than natural ventilation strategies (i.e. Type 1).

Winwood et al. [1997a,b,c,d] presented their comprehensive study on the advanced fabric energy storages[4] (FES) which use the building structural mass as thermal mass and pass ventilation air through the structural mass for the purpose of heat exchange. The first paper [Winwood et al., 1997a] presented a literature survey of advanced FES systems focusing on the FES-slab (TermoDeck system). The second paper [Winwood et al., 1997b] described the investigation of fluid flow in the FES-slab using computational fluid dynamics (CFD) simulation. The theoretical analysis of the thermal performance of whole building and the slab was carried out using the software ESP-r[5], and was presented in the third paper [Winwood et al., 1997c]. A simplified multi-node slab model was incorporated into the full-building simulation. The slab model uses the average heat transfer coefficient which was evaluated analyt-

[4] use structural mass to store thermal energy

[5] An *integrated modeling tool for building applications*. `www.esru.strath.ac.uk/Programs/ESP-r.htm`

ically from the second paper. The validation showed that whole-building simulations using this model produce accurate results when compared to experimental data. The last paper [Winwood et al., 1997d] presented experimental monitoring of the first UK building using FES-slab. The monitoring included thermal performance and energy consumption. The results show that FES-slabs provide stable and comfortable conditions throughout the whole year. Recommendations for improvements were made for future similar kinds of practice.

TermoDeck^{TM} approach

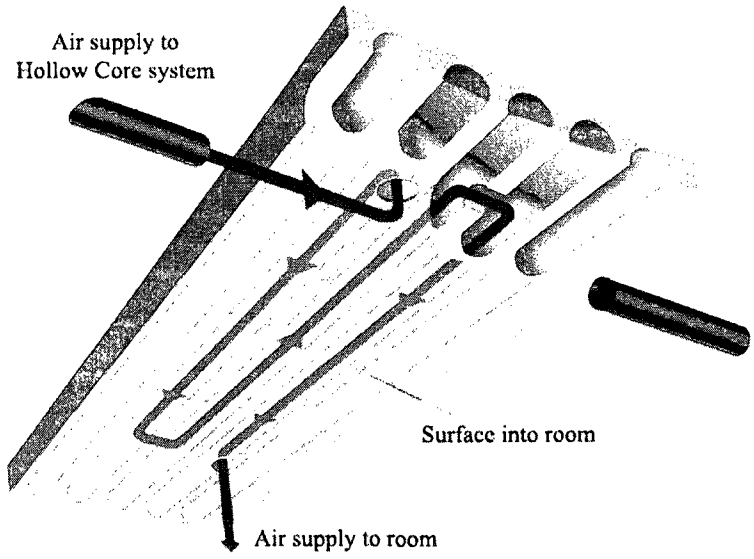

Figure 2.2: TermoDeck illustration (source: Swedish International Pressbureau. `www.publicitet.com`)

TermoDeck was developed in Sweden in the 1980's. Its applications focus on reducing cooling load in commercial buildings. TermoDeck utilizes the hollow cores within precast concrete floor slabs as ventilation ducts. Supply air is circulated through these ducts before being released into the living space. During this process, the TermoDeck slabs act as a thermal energy reservoir and the air is tempered. In some applications, for example, during summer nights, outdoor cool air is pumped

at low velocity through these ducts to extract the stored heat during daytime and to cool down the slabs to a certain temperature. In the daytime, the pre-cooled slabs condition the air passing through their internal cores. The air then circulates in the room below before returning via corridors to a heat exchanger and exhaust.

One of the existing buildings using TermoDeck, Elizabeth Fry Building at the University of East Anglia, is studied by Braham [2000]. The monitored data provided by Standeven et al. [1998] showed that:

- Heating and cooling energy consumption is half that of a conventional building of the same type.
- Use of TermoDeck provides good levels of thermal comfort. Occupant satisfaction and productivity is high.
- Capital and maintenance costs are low.

Barton et al. [2002], using an explicit finite difference numerical model, carried out a theoretical study on the thermal performance of the TermoDeck. The model is validated with experimental data, and proved to have a high accuracy. The study concluded that the bends in the channels have a minimal impact on the overall heat transfer; and greater thermal attenuation is achieved by using a five-core pass system in comparison with a three-core system.

Ren and Wright [1998] in their study developed a simplified dynamic thermal model of a hollow core concrete slab thermal storage system and associated room. This model used a lumped parameter concept and thermal network technique. It considered the heat exchange between the ventilation air and the slab core, the thermal storage in the building structure, and the surface temperature difference in the room. Ren and Wright verified their model with measured performance data. The compar-

isons showed that the model gives an acceptable accuracy for normal cyclic operation, but not for step input operation (e.g. step temperature change of supply air). One thing should be noticed that, in the application of Dittus-Boelter correlation, $Nu = 0.023 \cdot \mathrm{Re}^{0.8} \cdot \mathrm{Pr}^{n}$, to calculate the convective heat transfer coefficient (CHTC), the author used $n = 0.4$ instead of 0.3. When the core air is warmer than the core surface (such as the case in this reference), $n = 0.3$ should be used [Kreith and Bohn, 2001]. Nonetheless, this study shows the feasibility and advantage of using a lumped parameter model with thermal network technique in whole building thermal modeling.

Shaw et al. [1994] listed some advantages and one disadvantage of the TermoDeck approach:

- The TermoDeck approach utilizes a low cost construction form.
- It has the potential for efficient TES and controlled release of stored energy through the time constant of the structural mass. Controllable and efficient pre-conditioning of the building thermal mass can be achieved. It also "compensates" for improper design and control.
- It offers the potential to operate the central plant[6] with maximum efficiency. The concrete acts as a thermal storage and maintains the final supply temperatures within an acceptable band. A relatively low air supply volume can be used to avoid the need for high fan power.
- In addition, thermal comfort benefits from the large proportion of radiative heating.
- A potential penalty is TermoDeck approach has no 'rapid response' to the needs of an internal space.

[6]HVAC central unit, such as a chiller, a hot water boiler, a fan, etc.

2.3 Conclusions

The literature review shows that using building structural mass for TES has great potential. It is becoming the new trend to utilize the structural mass to improve the thermal performance of buildings, mainly by moderating temperature swings and reducing space conditioning energy consumption. Mechanically facilitated heat transfer within the structural mass helps in improving the storage efficiency and the control (e.g. temperature and heat transfer rate). Current research and developments merely focuses on reducing and shifting the cooling load of buildings. When reducing heating load is under consideration, attention is needed on how building structural mass can be used efficiently and effectively to store and distribute the collected solar thermal energy.

When more solar thermal energy (e.g. besides passive solar heating) is needed to further decrease space and DHW heating energy consumption, solar thermal collectors are desired. BIPV/T systems have proven to be an ideal option when PV systems have been employed to generate electricity. During the winter, the space and DHW heating are at their peak demand; meanwhile, the availability of the solar energy is at its low point. A larger area of solar thermal collector might be needed in order to collect a considerable amount of solar thermal energy in a short period. The collected heat could become intensive during the collecting period. At this point, efficient and rapid storage of the available solar thermal energy is highly desired. Mechanically facilitated structural mass becomes a great choice for active TES. It is able to efficiently store the intensive solar thermal energy collected by solar thermal collectors and naturally distribute the heat evenly into the living space.

The review reveals the necessity and feasibility of using active thermal mass to store heat for space heating purposes. It also presents the advantages of using VCS as active thermal mass in solar building applications. Comprehensive and detailed

study on using a VCS coupled with a BIPV/T system to efficiently and effectively utilize solar thermal energy is presented in this thesis to serve the above mentioned need.

Chapter 3

Design and Thermal Performance of a Solar House with a VCS-BIPV/T system

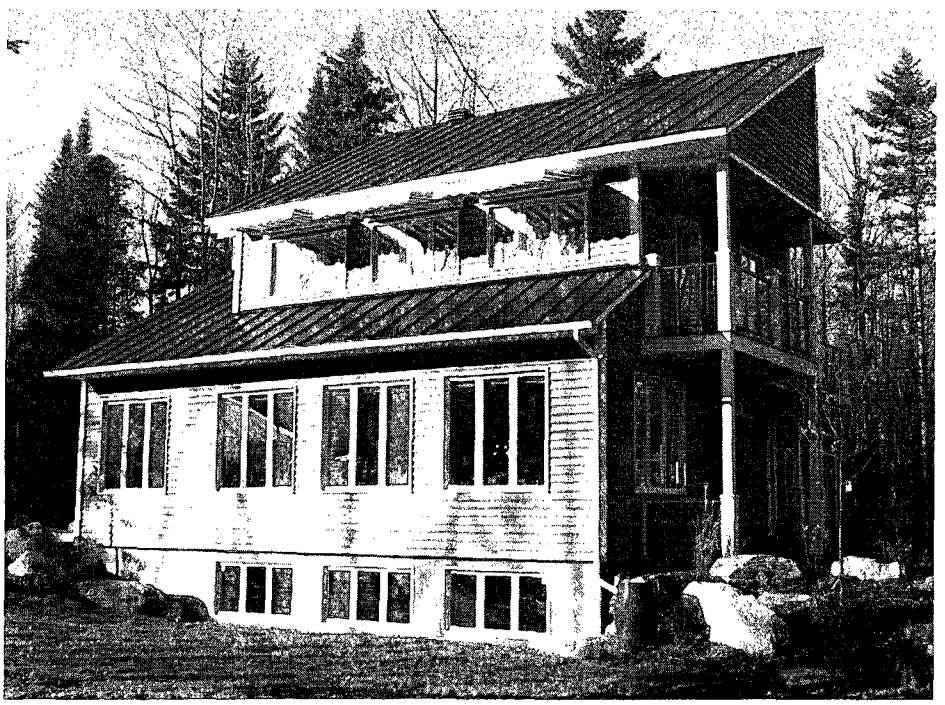

Figure 3.1: ÉcoTerra, fall 2007 (courtesy of Alouette Homes)

This chapter describes the design and thermal performance of an energy-efficient solar house: ÉcoTerra. This house includes an integrated system: ventilated concrete slab thermally coupled with building-integrated photovoltaic/thermal system (VCS-BIPV/T). Actual thermal performance of ÉcoTerra is extensively monitored. The design background, the building characteristics, and the recorded thermal performance of the house provide meaningful and in-depth information for the study of the VCS-BIPV/T system and this type of solar house.

In this chapter, the energy-saving approaches and the overview of the corresponding energy analysis will be described first. Then the concepts and design of the main house components will be described and explained. Detailed and in-depth engineering calculations and explanations of the VCS-BIPV/T system are included in the Chapters 4 and 5. Further information related to the construction details and lessons learned are included in Appendix A.

3.1 Introduction

In fall, 2006, Canada Mortgage and Housing Corporation (CMHC) launched a housing demonstration initiative named EQuilibrium. The purpose of this initiative is to promote sustainable types of housing. Health, affordability, resources, environment, and energy are the five principles of this initiative. For the energy part, CMHC describes it as follows: "One of the primary objectives of the EQuilibrium Housing initiative is to demonstrate the capacity of housing to drastically reduce the energy load required by a home, and then to produce as much, or more, renewable energy than it consumes on an annual basis ... They are designed to produce as much energy annually as they consume. Connected to the electricity grid, these homes draw power only as needed - and can feed excess power back into the system ..."[1]

[1]Canada Mortgage and Housing Corporation. www.cmhc.ca/en/inpr/su/eqho/eqho_003.cfm

Alouette Homes, a Quebec based prefabricated house builder, submitted its design proposal and was later selected as one of the twelve pilot demonstration teams. The built house is named ÉcoTerra[2]. It is a pre-fabricated energy-efficient solar house whose annual energy consumption aimed to be close to net-zero.

Reducing the heating energy consumption for space and DHW in this house is critical in achieving close-to-net-zero annual energy consumption. Several innovative systems that utilize solar technologies were selected at the conceptual design stage. These technologies include: (1) passive solar heating with passively charged thermal mass, and (2) BIPV/T with TES using actively charged thermal mass. An integrated space and domestic hot water heating system was adopted. The solar systems are supplemented by a ground source heat pump. A home automation system is employed to operate the system based on advanced control strategy and order of priority to optimize this integrated system's overall performance.

Design concepts were followed by careful engineering calculations, such as the energy consumption, cost analysis, and constructability. The optimization of the design of the ÉcoTerra, such as the sizing of the VCS-BIPV/T system, south-facing window area, and envelope design, involved advanced building simulations. Design meeting between engineers, architects and home builders took place frequently during the design and construction periods. The construction started in June 2007 and finished in November of the same year. The house is meant to be energy efficient and yet affordable and easy to construct. Since the construction finished, the Concordia engineering team has been monitoring the adopted innovative mechanical system, as well as the performance of the whole house. The team is also monitoring and provides recommendations for the home automation system. Up to the date that this thesis finished, the process is ongoing. Parameters that are being monitored include the power consumption, heating/cooling load, performance of the innovative

[2]Alouette Homes. www.maisonalouette.com/english/ecoterra2/alouettehomes.html

systems, etc. Those data will be shared by several institutional parties for academic research purposes.

3.2 An Overview of the Preliminary Design and Energy Analysis

ÉcoTerra is located in Eastman, Québec, close to Sherbrooke. Because weather statistics for Eastman are not available, data for Sherbrooke is used for energy analysis and simulation. Table 3.1 shows the monthly average dry bulb temperature and horizontal global solar radiation[3] of Sherbrooke. The outdoor design temperature for heating is -28 °C. ÉcoTerra is prefabricated in modules and assembled on site. The total floor area is about 140 m^2 excluding the 90 m^2 basement floor area. It is designed to accommodate a four-person family. Figure 1.3 on page 4 shows the integrated mechanical system in ÉcoTerra.

Table 3.1: Monthly average weather data of Sherbrooke, Canada (source: HOT2000 weather source code)

Month	Jan	Feb	Mar	Apr	May	Jun	Jul	Aug	Sep	Oct	Nov	Dec
Dry bulb temperature [°C]	-10.9	-10.7	-3.3	3.6	11.1	16.2	18.3	16.8	12.2	6.6	0.1	-8.1
Horizontal global solar radiaiton [MJ/m^2/day]	5.66	8.90	12.72	16.16	18.40	19.76	19.93	17.04	12.70	8.79	4.84	4.25

3.2.1 Energy-saving approaches

The main energy-saving approaches in this energy-efficient solar house are listed below:

[3]The sum of both the direct and diffuse components as measured incident on a flat horizontal plane.

1. **Energy self-generation:**

   (a) Electricity: a PV system is installed to generate electricity. The PV system produces approximately as much power as to balance the total electricity consumption from power grid.

   (b) Thermal Energy:

      i. BIPV/T roof collects the heat generated by solar irradiance using outdoor air as heat transfer fluid. The collected heat can be used for DHW and space heating. An active thermal mass - ventilated concrete slab - is employed to store part of the collected heat and release it later for space heating.

      ii. Passive solar heating. Thermal mass in the form of concrete slabs and walls, together with high thermal performance glazing are incorporated into the house to maximize the utilization of solar thermal energy.

2. **Energy efficiency**

   (a) The envelope is well thermally insulated and air tight. This reduces the undesirable heat loss during heating season or heat gain during the cooling season resulting from envelope conduction and natural ventilation.

   (b) Energy efficient devices:

      i. A ground source heat pump (GSHP) is adopted to provide space heating and cooling, also partially DHW heating.

      ii. Energy efficient lighting devices, such as compact florescent light bulbs are used. This kind of lighting device has high efficacy, which means more light is produced with the same amount of electricity. High efficacy also means less heat is produced, which consequently reduces the cooling load.

iii. Low or ultra low flow shower heads and faucets, a clothes washer and a dishwasher with reduced water use are installed in the house. Less water consumption means lower hot water heating load.

(c) Heat recovery:

i. The heat recovery ventilator maintains ventilation according to indoor air quality health standard and recovers heat from the ventilated air at the same time.

ii. Waste hot water heat recovery system recovers the heat from waste hot water and pre-heats the incoming fresh water.

3.2.2 Preliminary energy analysis

The overall energy analysis approach at the design stage is a set of combinations of simulation done with HOT2000 [NRCan, 2003], RETScreen [NRCan, 2006], and customized Mathcad [PTC, 2007] programs. Simulations were performed using real weather data. HOT2000 is used to optimize the envelope, RETScreen for the estimation of PV electricity generation, and Mathcad programs for the simulation of the thermal performance of the house and different components, such as the VCS thermal mass, BIPV/T system, the direct solar gain zone. Simulations from customized Mathcad programs are used to optimize the heat recovery from the PV and avoid overheating due to solar gains - i.e. optimize thermal mass in the house in relation to window area and determine the optimum window area. The optimal models based on simulation were adopted. The simulated thermal performance of the whole house became the basis for the sizing of mechanical space heating and cooling systems. These simulations are based on preliminary design parameters. Some of these parameters were changed during the construction as described in the later section.

The simulated thermal performance contains inaccuracy to a certain extent. Nev-

ertheless, the data from energy analysis in the design stage is the basis for the integrated design of the whole house, especially the sizing of the mechanical system.

Summary of results from HOT2000 simulations

The heating setpoint is 21 °C for main floor, and 19 °C for basement. Based on HOT2000 simulation, the Gross Space Heating Load is predicted to be 77012 MJ (21390 kWh) per year. Usable passive solar gains of 34051 MJ (9459 kWh) plus internal gains of 13407 MJ (3724 kWh) reduce the space heating system load to 29613 MJ (8226 kWh). Using a geothermal heat pump (water-air) results in an estimated annual space heating energy consumption of 7582 MJ (2106 kWh). The DHW (for 150 L/day of water at 55 °C) energy consumption with electric heating and blanket tank insulation of RSI 1 is 12017 MJ (3338 kWh). There are two tanks in series. The water in the first tank is pre-heated by the BIPV/T, desuperheater and the drain water heat recovery exchanger. The water in the second tank will be heated to 55 °C by electrical coil. For appliances and lighting together, the load is 3975 kWh. The dryer consumes about 900 kWh of this energy.

Summary of results from RETScreen simulations

In the design stage, a 3 kW PV system was decided to be installed. It consisted of 22 amorphous thin film PV panels attached to metal roofing. Each panel is rated at 136 watts for a total of 22 x 136 = 2992 watts. The electricity generation by the PV system, as determined by RETScreen, is 3420 kWh/yr for a slope of 30 degrees. Eventually in the construction stage, there are only 21 panels installed. So as to provide a output voltage within the range limited by the inverter, the panels are wired in three parallel arrays consisting of 7 panels each.

Mathcad simulations for VCS-BIPV/T system

Chen et al. [2007] conducted a theoretical study on the thermal performance of ÉcoTerra and its VCS-BIPV/T system. For the BIPV/T system, the flow velocity of the air under the PV will vary from a minimum of 0.5 m/s to a maximum of about 1 m/s and the outlet air temperature $T_{PVT.air.out}$, will be typically from 15 to 30 °C higher than the ambient air temperature. For example, in the summer, the typical outlet air temperature is 40 to 50 °C; while in spring and fall, 25 to 40 °C is typical on clear days. The BIPV/T system can typically produce a peak of 12 kW of heat at 500 CFM of air flow. In heating season, the air will be most useful for drying clothes and heating the floor slab. In all other seasons, the heated air will be used for drying clothes and DHW preheating. Figure 3.3 shows, on day 40[4] - a typical sunny and mild cold winter day, the estimated performance of the VCS-BIPV/T system. The BIPV/T system collects solar thermal energy and the VCS is heated by the collected thermal energy.

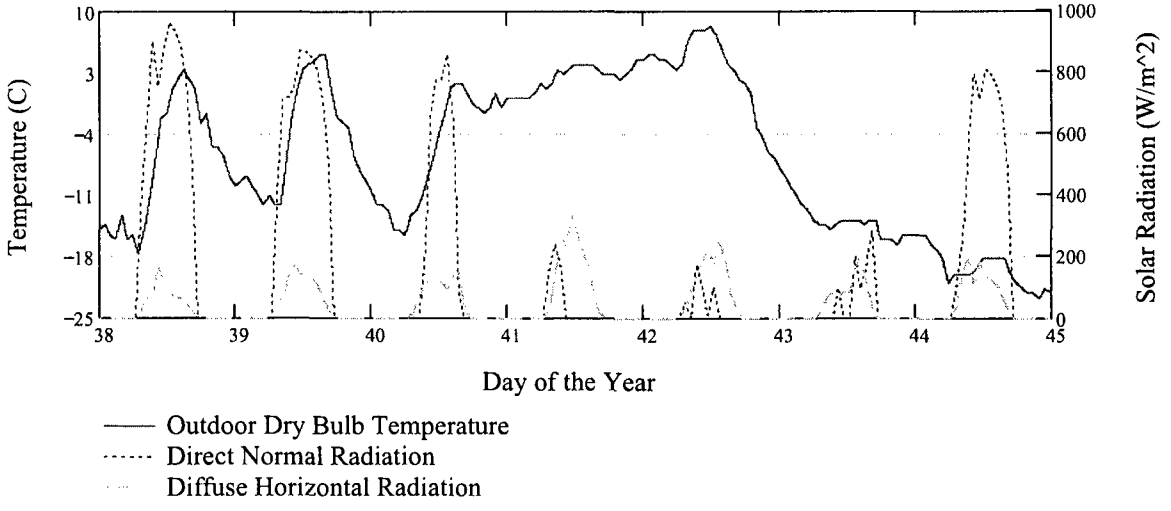

Figure 3.2: Weather profiles for simulation in preliminary design stage (day 38 to day 44[4]) [Chen et al., 2007]

During the period from November to March, the heated air will be used mainly to

[4]Day 40 is the 40^{th} day of the year starting from January 1^{st}, i.e. February 9^{th}

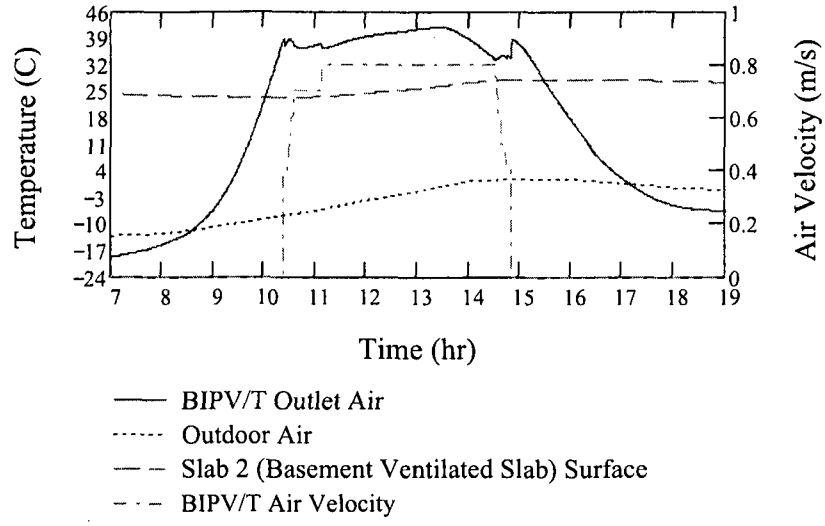

Figure 3.3: Simulated temperature profiles of VCS-BIPV/T system in preliminary design stage (day 40[4]) [Chen et al., 2007]

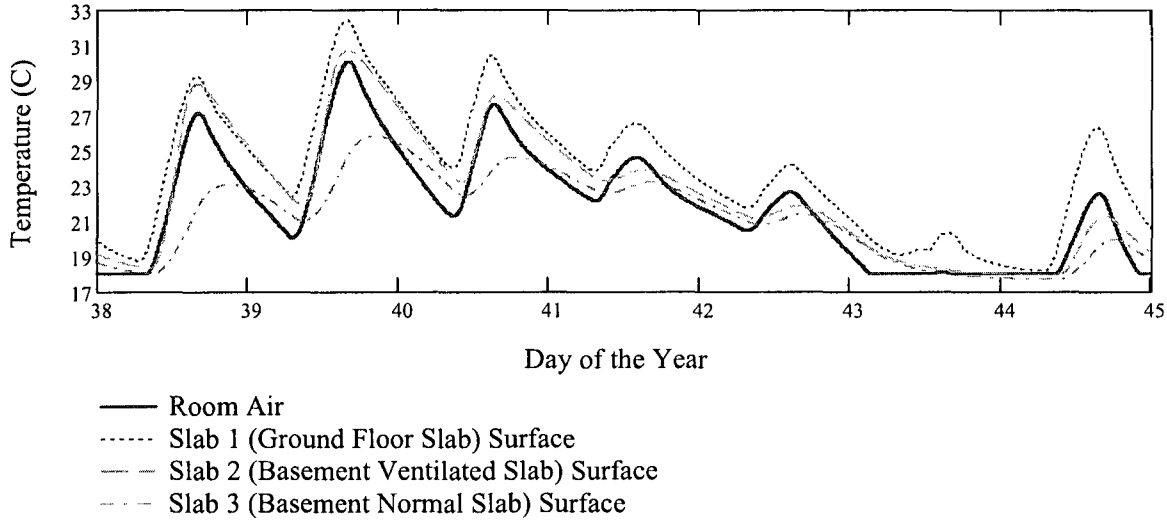

Figure 3.4: Simulated temperature profiles of room air and slab surfaces in preliminary design stage [Chen et al., 2007]

heat the thermal mass in the basement, with an average daily recovered thermal energy of about 10 kWh, there will be about 1500 kWh of space heating load reduction in the heating season. Figure 3.4 shows the temperature profiles of the slabs' top surfaces and room air. Note that, space and floor surface overheating is predicted even during cold outdoor temperature conditions. During the other 7 months, a high outlet air temperature (over 40 °C on clear days) can be achieved and the priority is

to heat water when drying of clothes is not needed.

Conclusions for energy analysis and simulation

HOT2000 is not able to consider the energy reduction contributions from some of the components, such as VCS-BIPV/T system and drain hot water heat recovery. This reduction was manually subtracted from the calculation of HOT2000. Table 3.2 shows the estimated annual energy consumption and compares them with reference values which would be consumed by a regular house of a similar size.

Table 3.2: Reference and estimated energy consumption of ÉcoTerra (REC: reference energy consumption [NRCan, 2003]; EEC: estimated energy consumption) [Chen et al., 2007]

Annual Energy Consumption $[kWh]$	**REC**	**EEC**
Space Heating Load	13209	1123
DHW Heating Load	5191	609
Electrical Appliance	8760	3975
PV Electricity Generation	0	3420

As we will see later, by comparing the simulation with field measured data, the above estimations have errors to a certain extent. They include: overestimating the outlet air temperature from the BIPV/T system, overestimating the temperature of room air and floors, and etc. The errors are mainly due the difference between the assumed environment and the constructed environment, such as the thermal insulation values, the air leakage in the duct, the different transmittance value of windows, the shading from the surrounding trees, and so on. However, the simulations did give rough ideas and guidelines for the integrated design of this advanced energy-efficient solar house.

3.3 Major Building Characteristics

In this section, the main characteristics of the built environment will be described. The Detailed and in-depth engineering calculations and explanations of the VCS-BIPV/T system are included in the Chapters 4 and 5.

3.3.1 Envelope

The thermal insulation value of the envelope greatly affects the energy consumption for heating/cooling the house. Besides the heat transfer consideration, other properties of the insulation material, such as sound insulation, integrated structural performance and water vapor permeance, also need to be considered carefully.

There were two main interacting issues regarding the envelope's thermal insulation. The first issue is the thermal resistance vs. cost. Obviously, for the opaque portion of the envelope (wall, roof, and foundation), the higher thermal resistance it has the better thermal performance it has. However, according to the simulations by HOT2000, the effectiveness of reducing the annual energy consumption for heating and cooling becomes smaller as the thermal resistance goes higher. This means that increasing the thermal resistance to reduce the energy consumption becomes less effective as the thermal resistance goes higher. Furthermore, higher thermal resistance costs more in material and construction, but less heating/cooling utility bills.

The second issue is what kind of insulation should be used. Traditional insulating methods - fiber glass bat in-between wood studs and then exteriorly covered by extruded polystyrene (EXPS) panel - will result in very thick exterior walls if R35 or above effective insulation value is desired. Two kinds of innovative spray-in-place foam insulation are used in ÉcoTerra: "Enertite®" [CCMC, 2007] and "Walltite®"

[CCMC, 2006]. There are additional contributions from these two thermal insulation materials. Enertite can improve the acoustic insulation of the envelope. Meanwhile, Walltite acts as an air or vapor barrier, and also contributes structural rigidity to the wall system. More detailed specifications are included in Section A.3.

Table 3.3: Simulated effects of insulation values on annual heat loss

Roof		Wall		Under Basement Slab	
RSI	Heat Loss [MJ]	RSI	Heat Loss [MJ]	RSI	Heat Loss [MJ]
5.5	6784	4.0	22524	0.5	13821
7.1	5381	5.3	16986	1.3	13314
8.4	4631	6.3	14337	2.6	12702
9.1	4294	7.6	11879		
9.5	4104				
RSI value is the effective value. Heat loss is the annual value. 1kWh = 3.6MJ					

Table 3.3 lists the simulation results from HOT2000 for annual heat loss through different components under different insulation values. After balancing the requirement of construction and material cost, energy consumption, and other technical issues as mentioned above, the shaded values in this table are adopted at the design stage. RSI 5 (R 28) is chosen for the basement walls. Those value listed here are effective thermal resistance. Actual thermal resistance will be slightly higher or lower depending on the composition of the envelope components. Figure 3.5 shows the construction drawing of the cross section of the envelope.

Design issues regarding windows are described in Section 3.3.3. The air tightness of the house, verified by a blow door test, is 0.9 ACH under 50 Pa pressure.

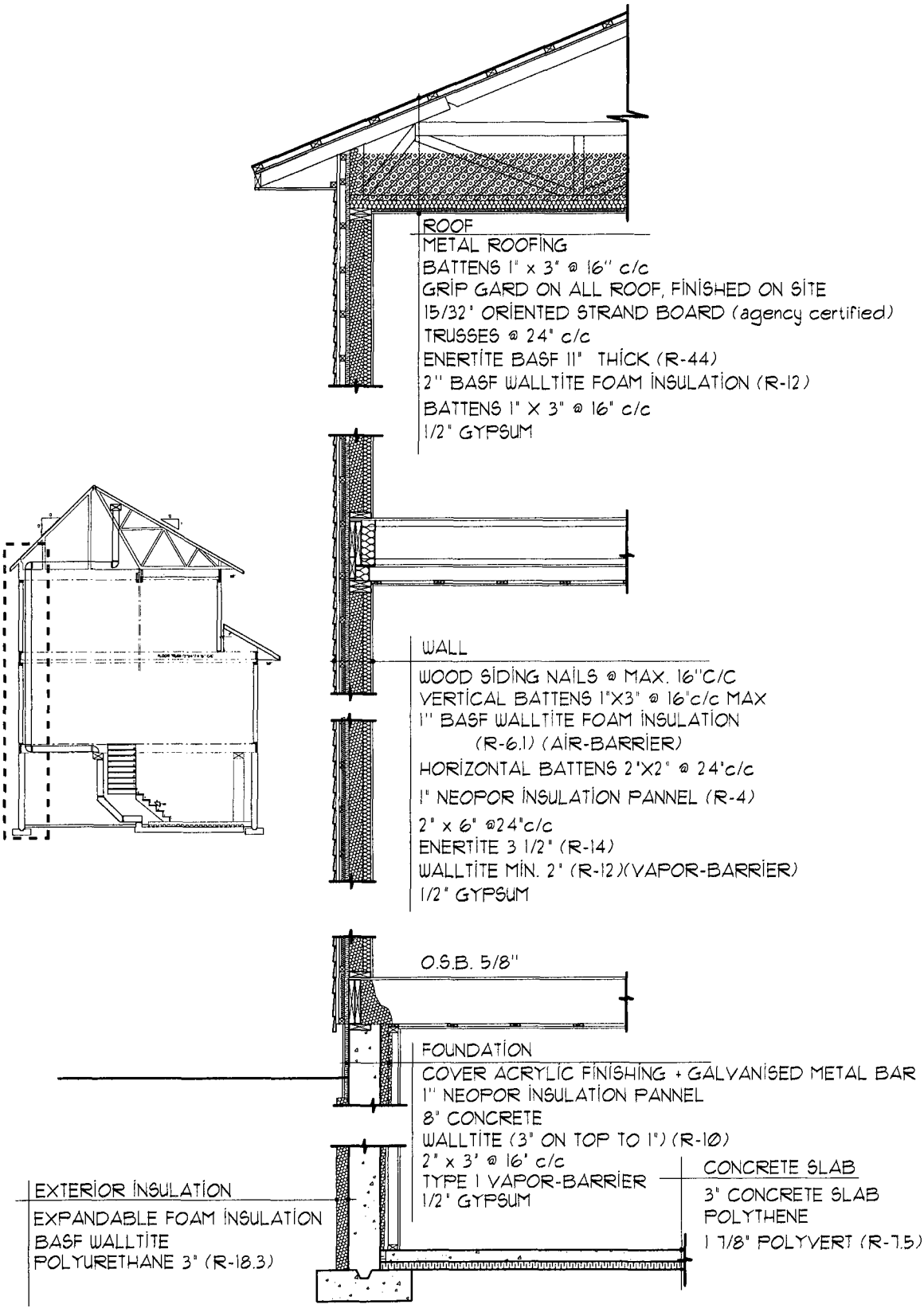

Figure 3.5: Cross section of the north wall (courtesy of Alouette Homes)

3.3.2 Mechanical system

The primary heating and cooling equipment was chosen to be a 2.2-ton[5] two-stage water-to-air GSHP with an ECM (electronically commutated) fan motor. A 3 ton GSHP is actually installed. This heat pump uses well water at the flow rate of 8.3 GPM from the 160 ft deep well, which is found at the site. The heat pump, through its desuperheater is also estimated to provide about 700 kWh/yr of heating for domestic hot water.

The ventilation rate can be controlled by the home automation system. When the house is occupied, the controller will set the heat recovery ventilator (HRV) to regular mode, which sets the ventilation rate at 0.3 ACH (air changes per hour). When the house is not occupied, the last person leaving the house can switch the ventilation rate to 0.15 ACH. This control strategy is able to reduce the heat loss due to unnecessary ventilation. The net annual air leakage and ventilation load (without ventilation control strategy and with HRV at 60% efficiency) is around 5070 kWh as estimated by HOT2000 simulation for a natural air infiltration of 0.07 ACH and a total air change rate of 0.33 ACH.

The system consists of two 60-gallon tanks in series. The entering cold well water is first heated by a drain water heat recovery system, and then enters the first storage tank. In the first storage tank, the water will be heated using the desuperheater of the geothermal heat pump and the hot air from BIPV/T system (if available) through an 6-row coil air-to-water heat exchanger with a face area of 2.5 ft^2. The DHW will be heated up to the final supply temperature (55 °C) in the second storage tank using a backup electrical heater.

Data from one operation is plotted in Figure 3.6 to demonstrate the effectiveness of the air-to-water heat exchanger when using the solar heated air to warm the

[5] 1 ton = 12000 Btu/hr = 3517 watts

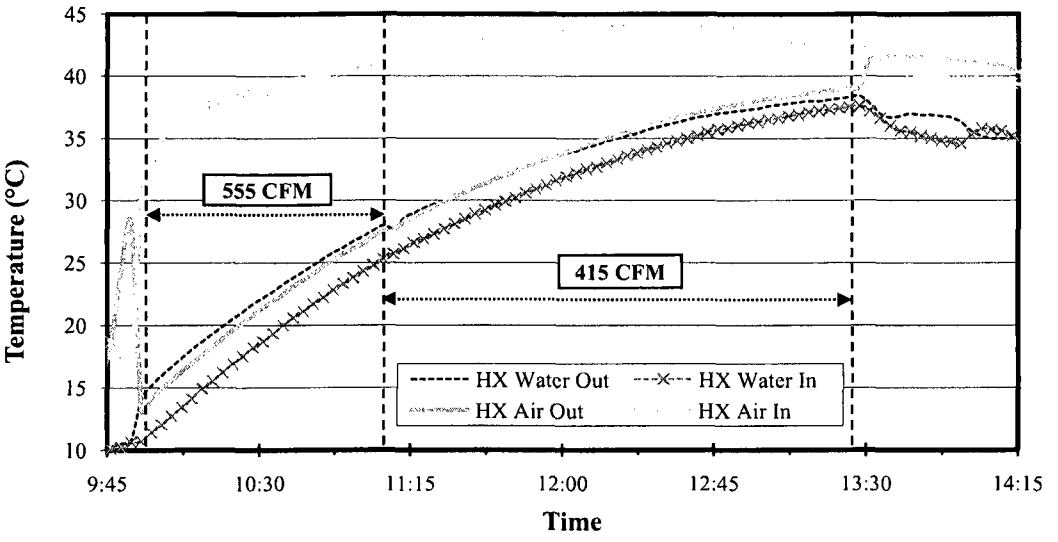

Figure 3.6: Temperature profiles of water and air in heat exchanger, April 17^{th}, 2008

domestic hot water. The effectiveness of the heat exchanger is calculated to be about 85% (with an estimated water flow rate of 8 gpm). It can be seeing that the 227 L (60-gallon) domestic hot water pre-heating tank was heated from 10 to 25 °C in 67 minutes with a warm air flow rare of 0.26 m^3/s (555 CFM) coming from the BIPV/T unit, and from 25 to 37.5 °C in 140 minutes with 0.19 m^3/s (415 CFM) air flow rate. This corresponds to an average energy transfer of 3.5 kW in the first time frame, and of 1.5 kW in the second.

Using the heat pump desuperheater for DHW heating is estimated to reduce total DHW energy consumption (3338 kWh) by about 700 kWh. The "Power-pipe" - drain hot water heat recovery - is estimated to reduce this consumption by another 700 kWh (manufacturer claims 25 to 40% savings, a conservative estimate of about 20% is adopted here).

3.3.3 Passive solar heating

Traditionally, there are three main factors concerned with window design: daylighting, view and thermal resistance. As passive solar heating is employed in ÉcoTerra, transmittance of solar radiation becomes another important factor. Windows with high thermal resistance and high solar radiation transmittance are used. They are triple glazed with two hard low-e coatings (emissivity 0.35) on the cavity-side of two outer panes, two 13-mm Argon filled gaps, and vinyl frame with thermal breaker. The effective thermal resistance is about RSI 0.85 (R 5) (window size affects the effective RSI value) and the solar heat gain coefficient (SHGC) is about 0.5. The transmittance of the windows is about 36% to solar energy at normal incident angle, and 71% to visible light. The total south-facing window area is about 40% of the south facade area. The south-facing window area of the ground floor is about 13 m^2, which is approximately 15% of the ground floor area. Note that, windows with high energy-rating cost more than regular windows. Upgrading windows raises the classic question: initial investment vs. long term benefit/pay back.

Table 3.4: Simulated effects of south-facing window areas on space heating load

Ground Floor South Facing Window Area (m^2)	Gross Space Heat Loss (MJ)	Usable Solar Gains (MJ)	Net Loss (MJ)
7.2	78057	28779	49278
9.8	79487	30541	48946
12.9	81253	33863	47390
14.8	82343	35486	46857
17	83566	37241	46325

Compared the wall thermal resistance (RSI 6.3), the thermal resistance of the window (RSI 0.85) is still relatively low. This means the larger the window area, the more the heat loss. However, the larger the window area, the more solar radiation will be utilized for passive solar heating. Based on the HOT2000 simulations (Table 3.4), larger south facing window area will result in smaller gross space heating load (i.e.

net loss), but this becomes less effective as the window area becoming larger.

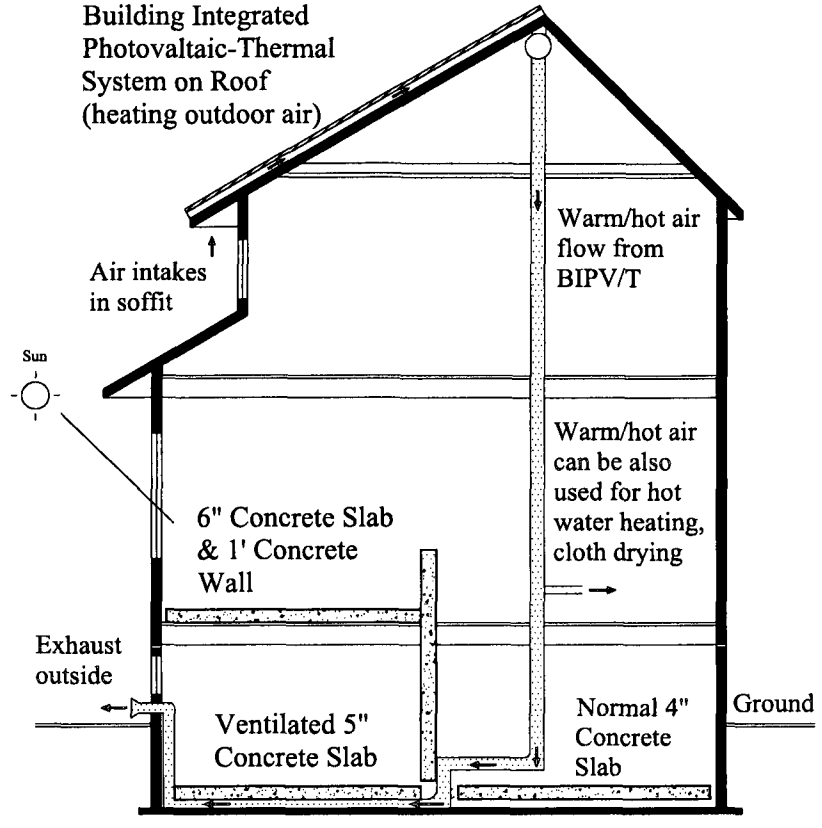

Figure 3.7: Locations of thermal mass and BIPV/T system

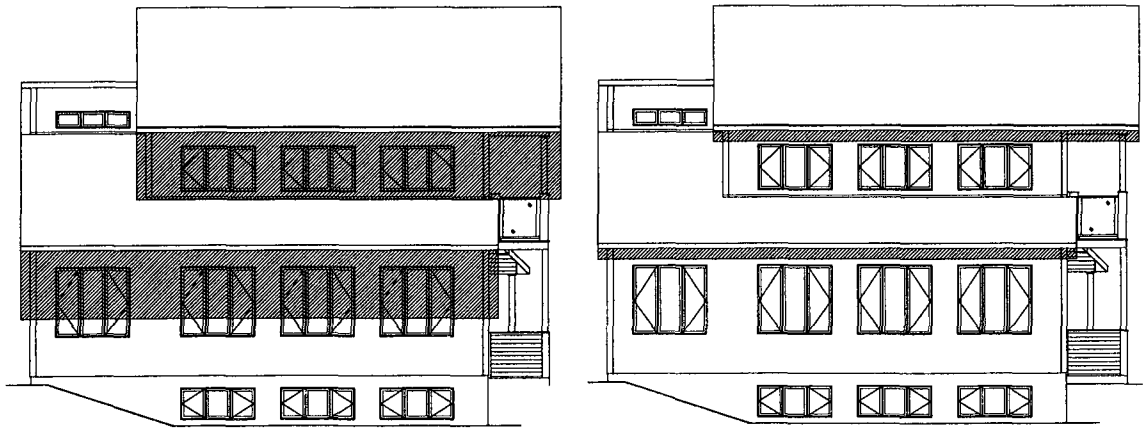

(a) June 21^{st} (b) December 21^{st}

Figure 3.8: Passive shading with overhang

Concrete mass in the ground floor and walls are used as the main direct gain thermal mass to store the solar energy transmitted through the south-facing windows. The

locations of the concrete mass can be seen in Figure 3.7. One 150 mm thick concrete slab is cast directly on top of the wooden floor supported by wood trusses underneath. Room air temperature is allowed to raise 5.5 °C from 21 °C (heating setpoint) to maximize passive solar heating. In general, distributed thermal mass is preferable and a concrete thickness of about 200 mm has optimal thermal admittance [Athienitis and Santamouris, 2002].

The size of the overhangs (e.g. soffit) over the south-facing windows is calculated. It allows the window to be exposed to direct solar radiation as much as possible in the heating season (Figure 3.8(b)), but blocks most of the direct solar radiation when it is not needed (Figure 3.8(a)).

3.4 Thermal Performance

The temperature distribution inside the house is heavily monitored. One thermocouple is installed in each room or hallway to measure its room air temperature. There are a total of six of them. There are another ten thermocouples embedded in the ground floor concrete slab: five near the top surface and five at the bottom (Figure 3.9). "T" type (copper-constantan[6]) thermocouples with accuracy of ±0.5 °C were used.

Currently, the house is reserved for monitoring, and sometimes for public visiting, so it is not occupied. The space heating consumption recorded will be over-estimated due to the absence of internal heat gains (e.g. appliances and human bodies). However, with the comparison of the data between cold sunny days and cold overcast days, the contributions to the reduction of space heating energy consumption from passive solar heating can be evaluated. For three continuous days (Figure 3.10),

[6]An alloy of 45 percent nickel and 55 percent copper, used chiefly in electrical instruments because of its constant resistance.

during which BIPV/T and ventilated slab did not operate, the heating requirement was 78 kWh for Jan. 12^{th}, 60 kWh for Jan. 13^{th}, and 96 kWh for Jan. 14^{th}. The average outdoor temperature on Jan. 12^{th} was 5 °C higher than that of Jan. 13^{th}, which was sunny. Figure 3.10(b) shows the temperatures of the family room above the passive slab and the basement below the slab. It can be seen that the cycling of the forced-air heating system is about 2 hours. The temperatures inside the passive slab show no significant stratification. If the room is further thermally coupled with the thermal mass, for example using TermoDeck approach (Section 2.2.4), the effective thermal capacitance of the room is increased. The warm supply air could be discharged after going through the thermal mass or returning through the thermal mass. The frequency of the cycling of the heating system will hence be reduced. In such way, the temperature fluctuation of the room will be reduced. Based on this point of view, active TES system should be promoted.

Another graph (Figure 3.11) for April 27^{th} indicates that the thermal energy stored from passive solar heating alone (i.e. no active storage) on one sunny cool day can help to avoid the auxiliary heating for the following cold day.

When VCS is used to store the thermal energy from BIPV/T system, the thermal

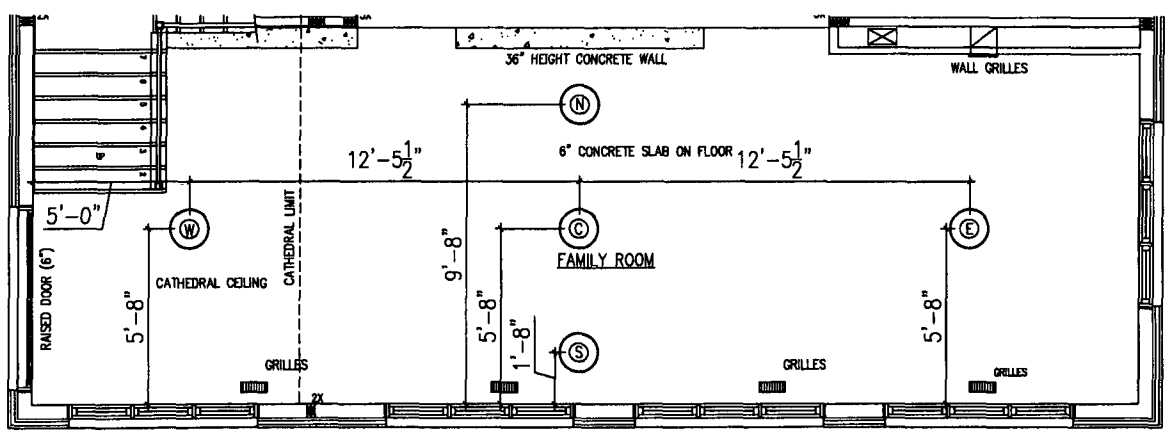

Figure 3.9: Locations of thermocouples in passive slab (the circled letters represent the locations)

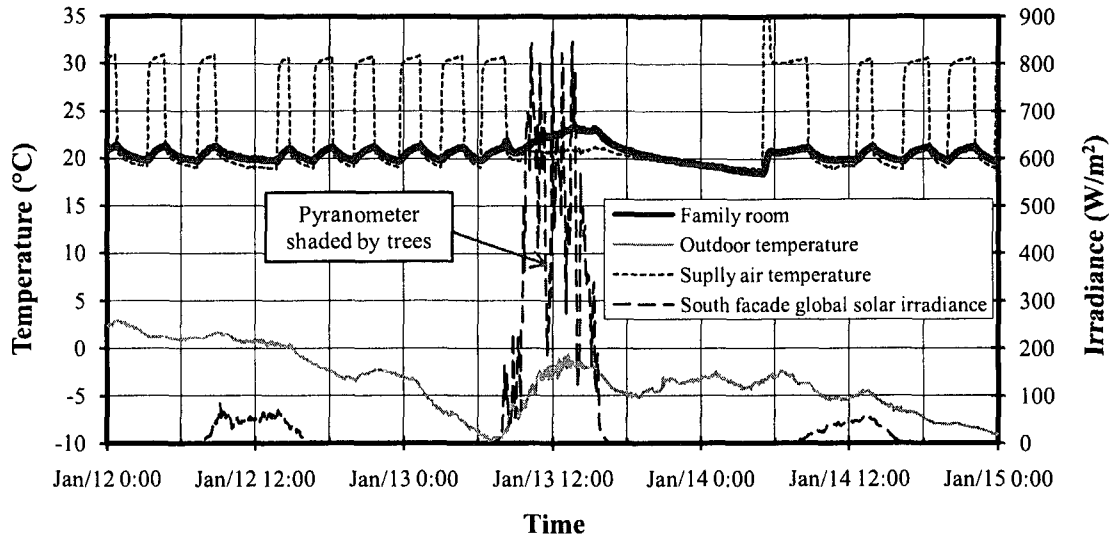

(a) Outdoor conditions

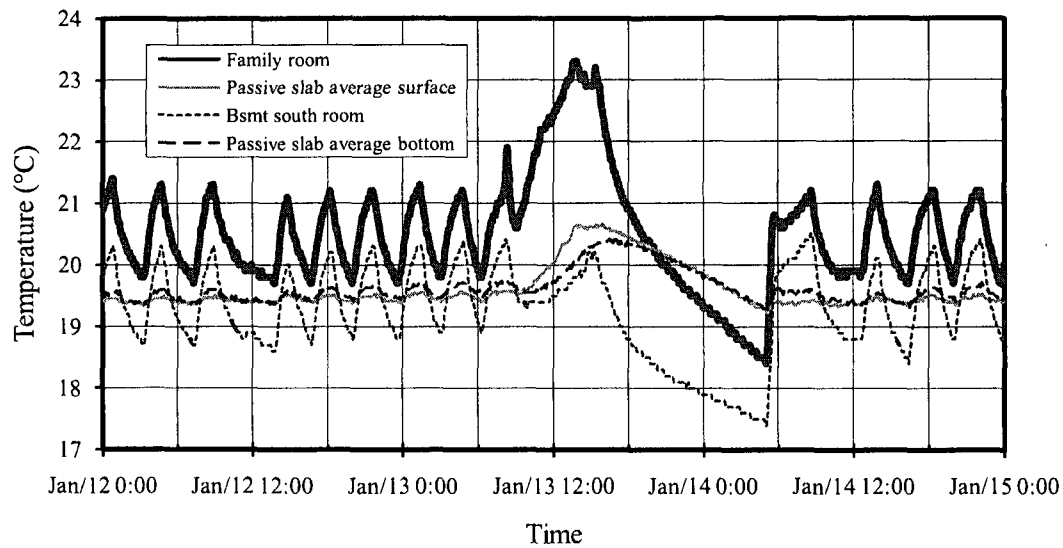

(b) Passive thermal mass temperatures

Figure 3.10: Temperature profiles on cold days with and without passive heating

energy collected from passive and active solar space heating further reduces the space heating load. Figure 3.12 shows that on a perfect sunny day, Feb. 24^{th}, with the passive solar space heating and the thermal energy collected from BIPV/T (about 3 kWh stored in the active slab), the room temperature was brought up about 4 °C higher (from 21 °C heating setpoint to almost 25 °C) during the day time even though average outdoor temperature was around -1 °C. The thermal energy stored

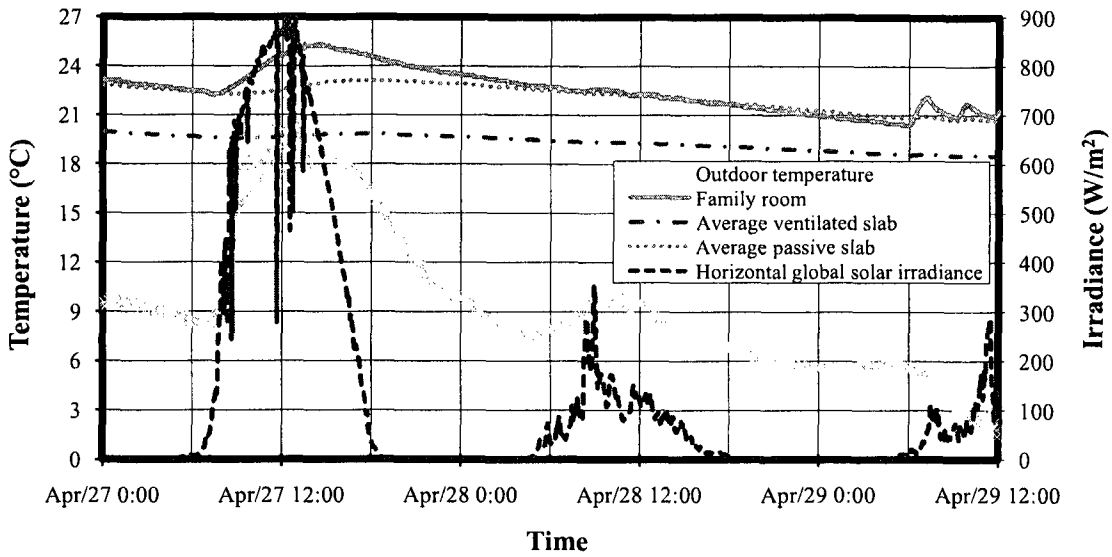

Figure 3.11: Temperature profiles on one cool sunny day followed by two cold overcast days

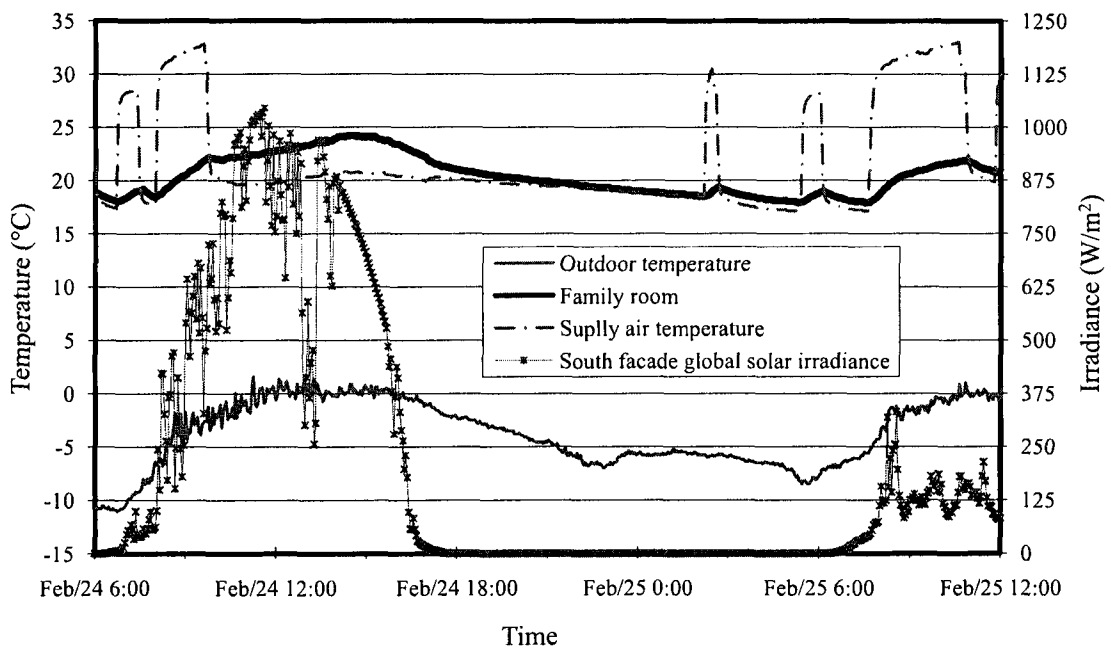

Figure 3.12: Temperature profiles on one cold day using passive and active solar heating, Feb. 24^{th} to 25^{th}, 2008

was adequate to keep the room air temperature above setpoint until 3:00 am of the next day when the night-time outdoor temperature dropped to around -5 °C.

Figure 3.13 shows the thermal performance of three consecutive cold sunny days in

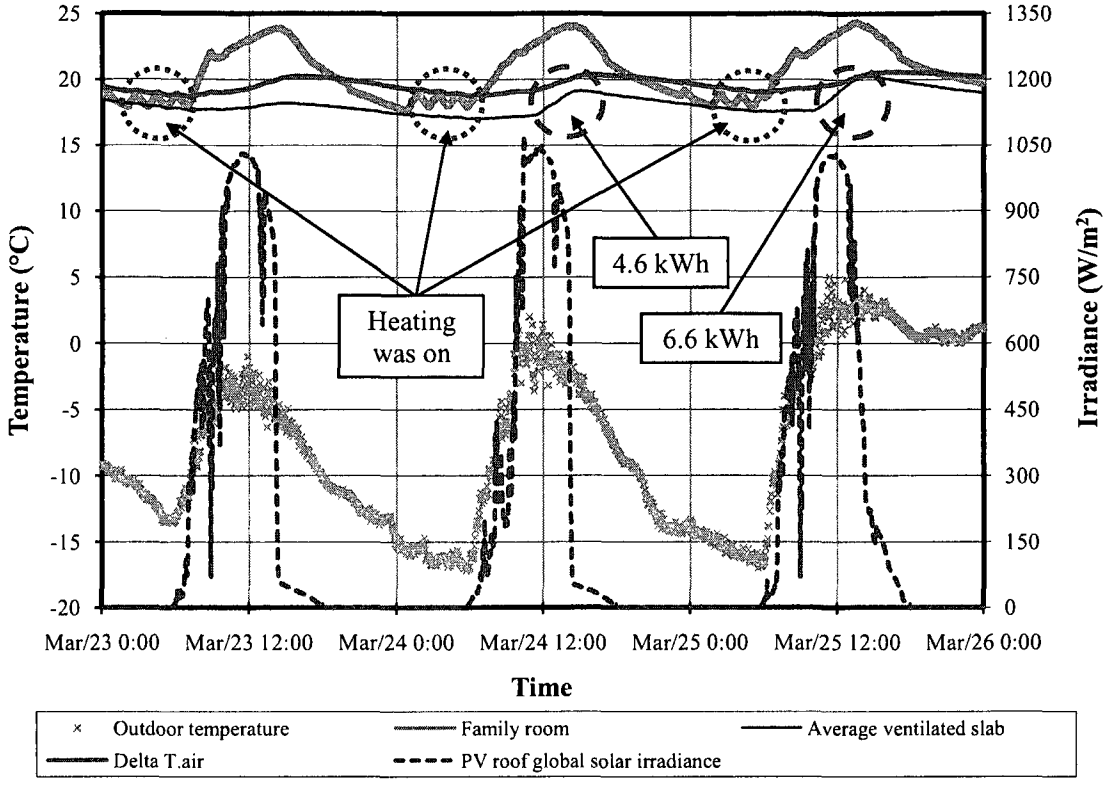

Figure 3.13: Temperature profiles on cold days using passive and active solar heating, March 23^{rd} to 25^{th}, 2008

the year 2008. On March 23^{rd}, the active TES was not operated. For March 24^{th} and 25^{th}, 4.6 and 6.6 kWh thermal energy were stored in the ventilated slab, respectively. During the two nights between 23^{rd} and 25^{th}, heating was only required for about 4 hours just before dawn. The average heating load was 65 kWh/day. Another figure showing the combined heating effect is Figure 5.6.

3.5 Summary

An energy-efficient solar house - ÉcoTerra was designed and built by SBRN and its members: Alouette Homes, researchers, industry partners and graduate students. ÉcoTerra integrates several innovative systems such as BIPV/T roof, VCS, GSHP, HRV and passive solar design, into conventional residential architectural design. The

design of the house was based on advanced building concepts and simulations. Preliminary results demonstrate that the systems perform well. The space heating load is greatly reduced by those integrated solar technologies. The house is expected to have annual total energy consumption approaching net-zero (less than 4000 kWh, 10% of that for normal house in similar size). This chapter provides the details in the design concepts, preliminary design simulations and preliminary results of the performance of the house, as well as the some of the individual components.

Chapter 4

BIPV/T System

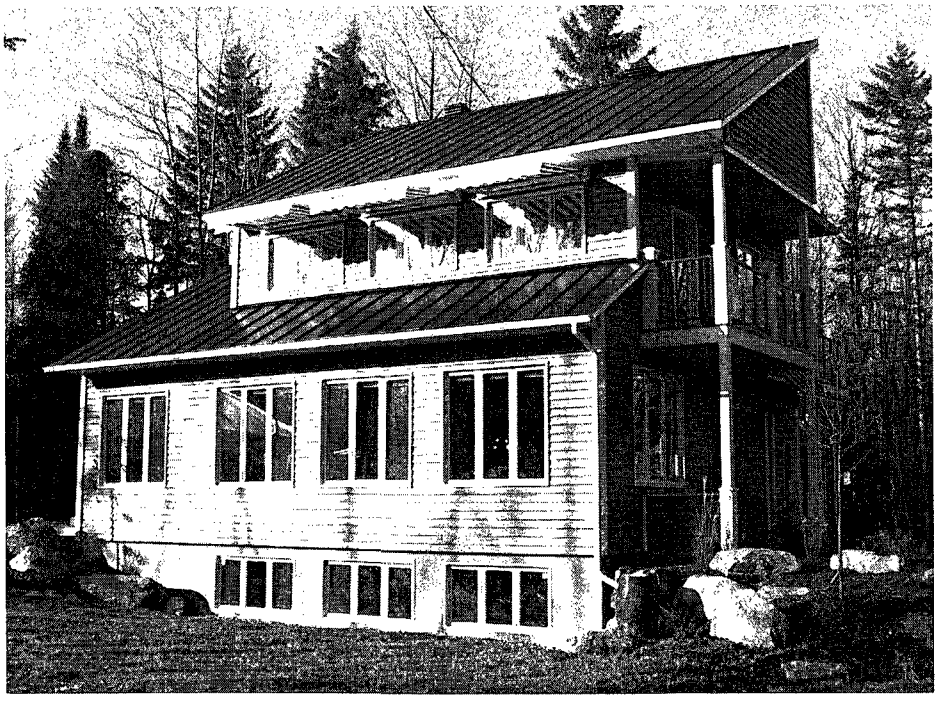

Figure 4.1: BIPV/T roof

In this chapter, the field measurement, study and modeling of the BIPV/T system in ÉcoTerra will be presented. The construction detail of and the lessons learned from the BIPV/T system are described in Appendix B.

4.1 Introduction

A BIPV/T system is able to convert solar radiation to electricity and thermal energy at the same time. When solar radiation strikes the surface, PV panels convert some of the absorbed solar radiation into electricity, and the rest of the absorbed solar radiation becomes heat. The PV panels are thus heated up. Heat transfer fluids (air in the case of ÉcoTerra) can be used to extract this thermal energy. The heat collected can be used for water and space heating, clothes drying, etc. Another advantage of collecting the thermal energy from the PV panels is the reduction in the PV operating temperature. Thus the efficiency of the electricity generation of the PV panels can be increased. A BIPV/T system can also serve as a part of the building envelope. This reduces the cost of the energy system as the BIPV/T replaces traditional material of the building envelope. A small amount of power is needed to drive the air, and additional constructions (e.g. duct, fan, pumps, etc) are needed for transferring the thermal energy. The trade-off is worthwhile after calculation. Figure 4.2 shows the concept of the BIPV/T system in ÉcoTerra.

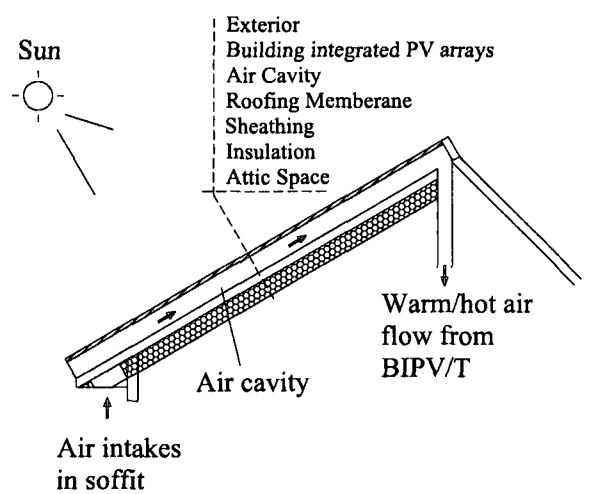

Figure 4.2: Schematic of the BIPV/T system in ÉcoTerra

The BIPV/T system in ÉcoTerra consists of amorphous laminate photovoltaic panels integrated into the metal roof. It is designed to cover one continuous south-facing roof

surface to make sure the system is water and air tight. 21 photovoltaic laminates[1] are attached to the metal roofing. Based on manufacture's specification, each panel is rated at 136 W at standard test conditions for a total of $21 \times 136 = 2856\, watts$. The electricity generation efficiency under normal operation condition (cell temperature at 46°C) is 6.1%. The cell temperature coefficient is 0.286 W/K. This means for every 10°C increase above 25°C (standard test conditions), there will be about a 3-watts deduction in electricity per panel. For an operation temperature of 80°C (expected under the summer condition without ventilation), the total electricity loss will be $0.286 \times 55 \times 21 = 330\, watts$ from a 2856-watt system capacity (about 12%). The electricity generated by the BIPV system as determined by RETScreen [NRCan, 2006] is 3265 kWh/yr for a 30-degree slope. This result does not consider the snow covering and shading on the panels that may occur from nearby trees.

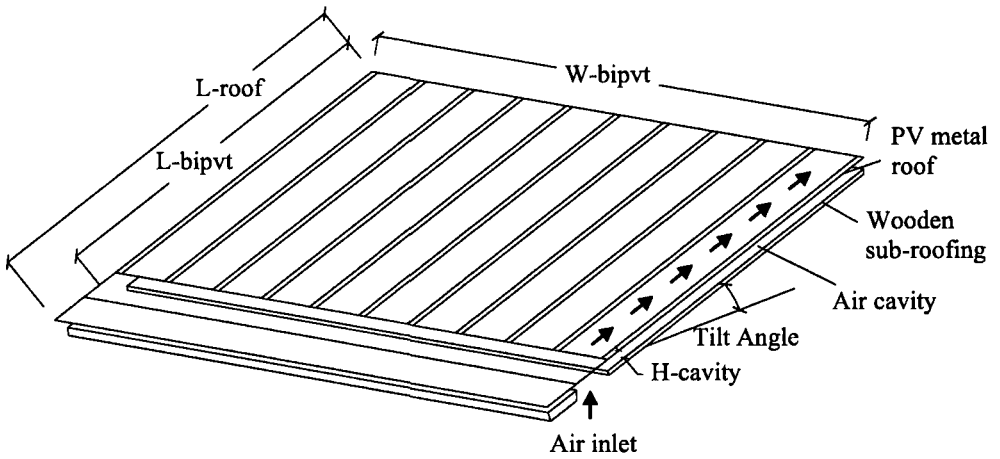

Figure 4.3: Schematic of BIPV/T geometry

The dimensions of the south-facing roof are 6.2 m (20 ft) long in the upward direction ("L-roof") and 10.4 m (34 ft) wide ("W-bipvt"). The PV panels and metal roofing cover the whole roof; however, the inlet of the BIPV/T system is not at the front edge of roof. The length of the BIPV/T system is 5.5 m (18 ft) ("L-bipvt"). The height of the air cavity (the distance between the metal roofing and the wooden sub-

[1]UNI-Solar PVL-136. `www.uni-solar.com/interior.asp?id=102`

roofing, "H-cavity") is 0.038 m (1.5 in). The calculated net cross section (normal to the air path) area $A_{pvt.ncs}$ of the BIPV/T air cavity is 0.332 m^2 after cross sectional area is adjusted to account for the upward wooden battens that are along the air path and that reduce the gross cross section area.

The air cavity that is created between the metal roofing and the wooden sub-layer is used to circulate outdoor air behind the PV modules. The metal roofing and the wooden sub-layer are separated by the upward 1"x3" and horizontal 1"x3" wooden battens. The outdoor air is used as the heat transfer fluid for simplicity and practical construction purposes. It is an open loop system so as to keep the temperature of the PV panels as low as possible, thus increasing their electricity production. The heat collected can be used for water and space heating, clothes drying, etc, in order of priority.

1. Drying clothes: if $T_{PVT.air.out}$ >15 °C, the dryer will run in fan mode only and air is drawn from the roof to dry the clothes and then exhausted.

2. Preheating water: if $(T_{PVT.air.out} - T_{water}) > 6$ °C then the air can be used to heat the water through air-to-water heat exchanger. T_{water} is the water temperature at the bottom of the preheat tank.

3. Thermal mass heating: if $(T_{PVT.air.out} - T_{mass}) > 3$ °C, then warm air is passed through VCS for active heat storage. Generally, with a target temperature of 19 °C in the basement, the floor slab will be at approximately 17 °C, so if the air from the BIPV/T system is at 20 °C or higher it can be used to heat the mass in the floor. Because of the air distribution system with the fan on, this heat will slowly be distributed to the rest of the house over a long period.

The orientation and the tilt angle of the BIPV/T system are critical to its performance because they define how much instantaneous and annual solar irradiance will

be received by the BIPV/T roof. Facing within 15 degrees away from true south is the optimal orientation [CMHC, 1998]. The optimal tilt angle can be roughly evaluated by the incident angle coefficient F_{iac} (the cosine of the angle of incident) at solar noon. At solar noon (about noon at local time) in Eastman (latitude at 45.26N), the solar altitude angle ranges from 22 degrees (December 21^{st}) to 68 (June 21^{st}), and the sun's profile angle equals to solar altitude angle. Table 4.1 lists the F_{iac} values under different α and β. The optimal roof tilt angle for Eastman is 45 degrees because its average F_{iac} is the highest for sun profile angles ranging from 20 to 70 degrees.

Table 4.1: Incident angle coefficients F_{iac} for Eastman

Sun profile angle α (degrees)	**Roof tilt angle β (degrees)**					**Wall**
	30	35	40	45	50	90
20	0.77	0.82	0.87	0.91	0.94	0.94
30	0.87	0.91	0.94	0.97	0.98	0.87
40	0.94	0.97	0.98	1.00	1.00	0.77
50	0.98	1.00	1.00	1.00	0.98	0.64
60	1.00	1.00	0.98	0.97	0.94	0.50
70	0.98	0.97	0.94	0.91	0.87	0.34

4.2 Monitoring Approach

In order to carefully study the thermal performance of the BIPV/T system, the system is heavily instrumented. Thermocouples are installed to monitor the temperature distribution. Solar irradiance and wind speed are being recorded. The time step of recording the temperatures and the irradiance readings is 3 minutes.

Temperature Thermocouples (TC) were installed during the pre-fabrication of the BIPV/T system. "T" type (copper-constantan) thermocouples with accuracy of $\pm 0.5\,^{\circ}C$ were used. Thermocouples are installed vertically along the air path

inside the air cavity (Figure 4.4(a) and 4.4(b)). Air temperatures are measured at all the 6 positions. Top surface (back of the metal roofing) temperatures are measured at all locations except location "1". Back surface (top of the wooded sub-layer) temperatures are measured only at position "2", "3", "4", and "5". The thermocouples for top surface temperature are fastened on the surface of the nearby wood frame. When the metal roofing is installed on top of the wood frame roof, the thermocouples firmly touch the metal roofing.

Thermocouples are also installed horizontally along the outlets at position "6". At every second outlet hole, one thermocouple is installed to measure the metal temperature and one more for the outlet air. There are a total of 10 thermocouples for metal and 10 for outlet air temperatures. These 20 thermocouples are used to check if the BIPV/T system is thermally balanced. Other temperatures are being recorded (Figure 4.4(c)), including two more thermocouples that were installed in the main ducts after the top outlet. One thermocouple is installed between the wooden sub-roofing (wood sheathing) and the spray insulation, and one thermocouple is installed to measure the air temperature in the vented attic.

Irradiance Pyranometers were installed after the roof module was assembled on site. Global solar irradiance is measured at three locations: in the vertical plane of the south facade, in the plane of the BIPV/T roof, and the horizontal plane on top of the roof. LI-200[2] pyranometer with error less than 5% is used.

Flow rate The flow rates in the BIPV/T roof were measured manually at the outlets of different paths (e.g. outlet after the heat exchanger or after the VCS bypassing the heat exchanger or not). The flow rate measuring device that was used is called a "Balometer" - an air capture hood equipped with a digital manometer used

[2]LI-COR Biosciences. `www.licor.com/env/Products/Sensors/200/li200_description.jsp`

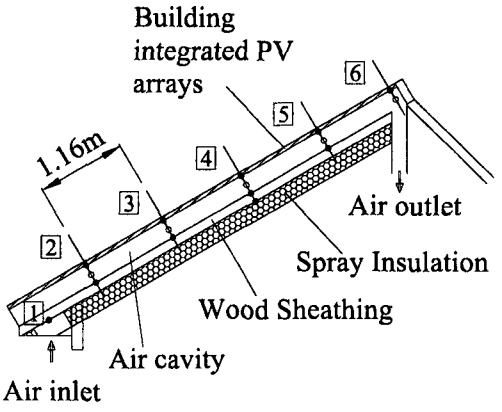

(a) Schematic of TC locations on roof

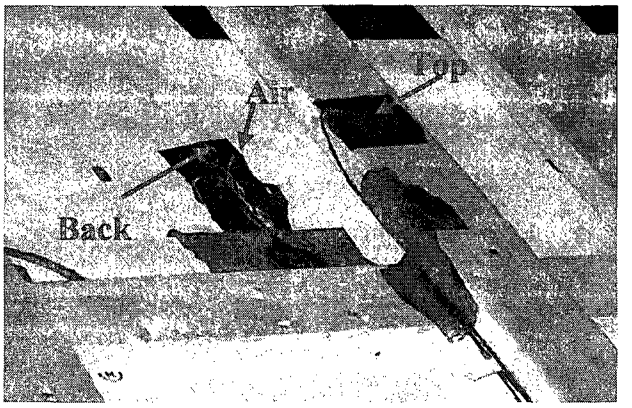

(b) TC positions at location "3" of Figure 4.4(a)

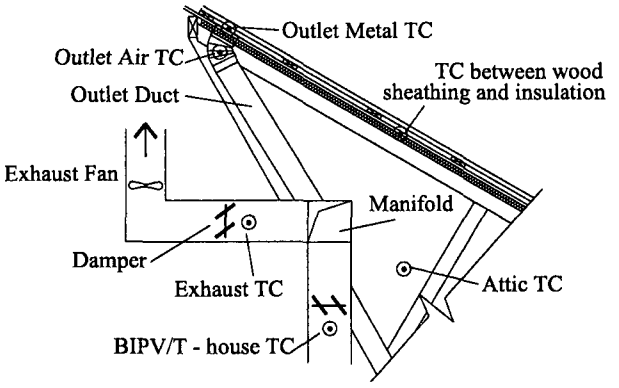

(c) Schematic of TC locations in air collecting duct and attic space

Figure 4.4: Locations of thermocouple in BIPV/T

to measure volumetric air flows, air temperatures, etc [3]. The accuracy for measuring air flow is $\pm 3\%$ of the reading plus ± 7 CFM. By changing the fan speed, the measured highest and lowest flow rates are 283 and 104 L/s (600 and 220 CFM), respectively. Knowing the $A_{pvt.ncs}$ (net area of cross section normal to air flow), the corresponding maximum and minimum air velocities in the BIPV/T cavity are calculated to be 0.85 and 0.31 m/s, respectively. $TotalFlowRate(CFM) = AirVelocity(m/s) \times 705$.

Wind speed A cup anemometer was installed on the pitch of the roof. However, the lower limit of wind speed measurement is 7 km/hr. Since the wind, even in low speed, has a significant effect on the thermal performance of the BIPV/T system

[3]TSI. www.tsi.com/en-1033/products/13872/balometer_standard_capture_hoods.aspx

(Section 4.5.1), lower wind speed values are needed for the detailed study on BIPV/T system. Local wind speed can also be approximated using the concept of a gradient mean wind speed V_g at the gradient height Z_g [Hutcheon and Handegord, 1983]. The mean wind speed V_z at any height Z is given by

$$\frac{V_z}{V_g} = \left[\frac{Z}{Z_g}\right]^{\alpha}$$

where

Z_g is the 400 m for well-wooded area

α is 0.25

Hourly meteorological wind data from Environment Canada[4] for the airport of the city Sherbrooke provides the value of gradient mean wind speed. The wind speed at roof height or 10 meters above the roof (needed in wind-induced CHTC correlation) in ÉcoTerra can be approximated. The local gust wind speed can also be approximated in a similar way. The comparison between the calculated wind speed and the locally measured value at roof height shows good agreement in the measured range.

4.3 Thermal Performance

Various system operation tests were conducted under different weather conditions and flow rates, and data were logged to analyze the performance. The monitored and analyzed data is used to optimize the automatic control of the BIPV/T system. After the optimization, self-operation of the BIPV/T system is monitored and desired performance is observed.

[4]Environment Canada. `http://climate.weatheroffice.ec.gc.ca/climateData/canada_e.html`

Thermographic study Figure 4.5 shows a thermographic image taken with an infrared camera during a warm summer day with the BIPV/T system operating. The temperature of the PV panels was in the range between 50 and 60 °C. Meanwhile, the temperature of the metal roofing of the lower roof was larger than 70 °C. The necessity and significant cooling effect of the air ventilation underneath the PV panels is obvious. The thermographic study also indicates that the air flow is well balanced as there is no significant horizontal temperature variation. The air flow underneath is approximately even; so is the air velocity. No significant horizontal temperature variation is also indicated by the air and metal temperatures measured at the outlet (Table 4.2). Knowing the BIPV/T system is well balanced is important in its thermal analysis. The thermal model can be approximated as two dimensional.

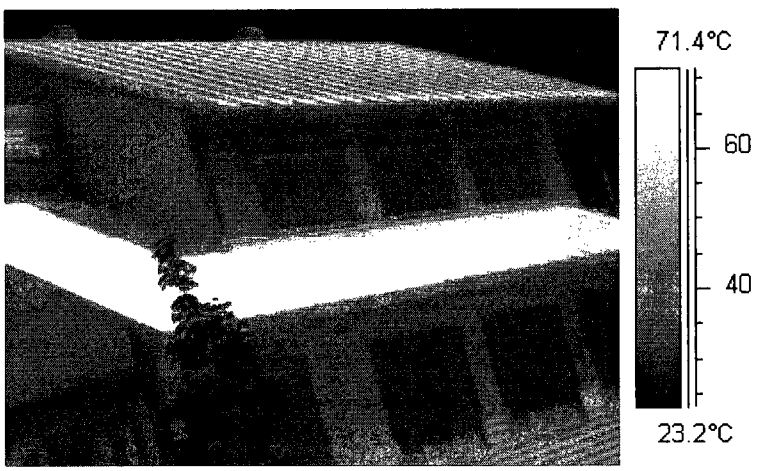

Figure 4.5: Thermographic image of BIPV/T roof

Figures 4.6 to 4.9 provide measured data for three typical days: a cold sunny day (March 17^{th}, 2008), a warm sunny day (April 17^{th}, 2008) and a warm partially cloudy day (June 25^{th}, 2008). Table 4.2 shows the statistic analysis of the measured values of the outlet metal and air temperature from these three days. At the outlet, there are 10 thermocouples measuring the metal temperatures and other 10 measuring the air temperatures. For each data recording time (every 3 minutes), the difference between the maximum and minimum temperatures and the standard deviation of all

the readings are calculated for air and metal, respectively. The "Maximum difference" represents the maximum value of the differences over time. The "Maximum standard deviation" represents the maximum value of the standard deviations over time. For the data measured on June 25^{th} between 11:00 to 17:00, the temperatures have a wide range (Figure 4.9). Their statistical analysis can represent the typical discrepancy of the outlet temperatures. The maximum difference between the lowest and the highest PV panel temperature was 5.8 °C, and the maximum standard deviation of the difference was 2.1 °C. For outlet air temperatures, these values were 4.1 and 1.3 °C, respectively. These values indicate that there is no significant horizontal temperature variation. The air flow in the BIPV/T cavity is well balanced.

Table 4.2: Statistical analysis of the measurements of the BIPV/T system temperatures (unit: °C)

	March 17th		April 17th		June 25th	
BIPV/T outlet	PV panel	Air	PV panel	Air	PV panel	Air
Maximum difference	5.1	4.9	4.5	4.8	5.8	4.1
Maximum standard deviation	1.6	1.6	1.3	1.6	2.1	1.3

Figure 4.6(a) shows the BIPV/T energy output in a commissioning test on March 17^{th}, 2008. The BIPV/T outlet air temperature reached almost 40 °C under cold clear sunny conditions with outdoor temperature close to -5 °C. The temperature increase was slightly more than 40 °C. The roof wind speed was about 1.8 m/s at noon. On Feb. 24^{th}, the weather condition was almost the same as that of March 17^{th}, except that the wind speed was about 3 m/s at noon. Under the same flow rate, the temperature increase of the air was only 30 °C. It can be observed that for every 1 m/s increase of wind speed, the outlet air temperature drops about 8 °C. This observation is reinforced by other field measurements, and it reveals that the wind effect on the thermal performance of the BIPV/T system is significant, and hence the choice of the correlation for wind-induced CHTC in the BIPV/T modeling is critical (Section 4.5.1).

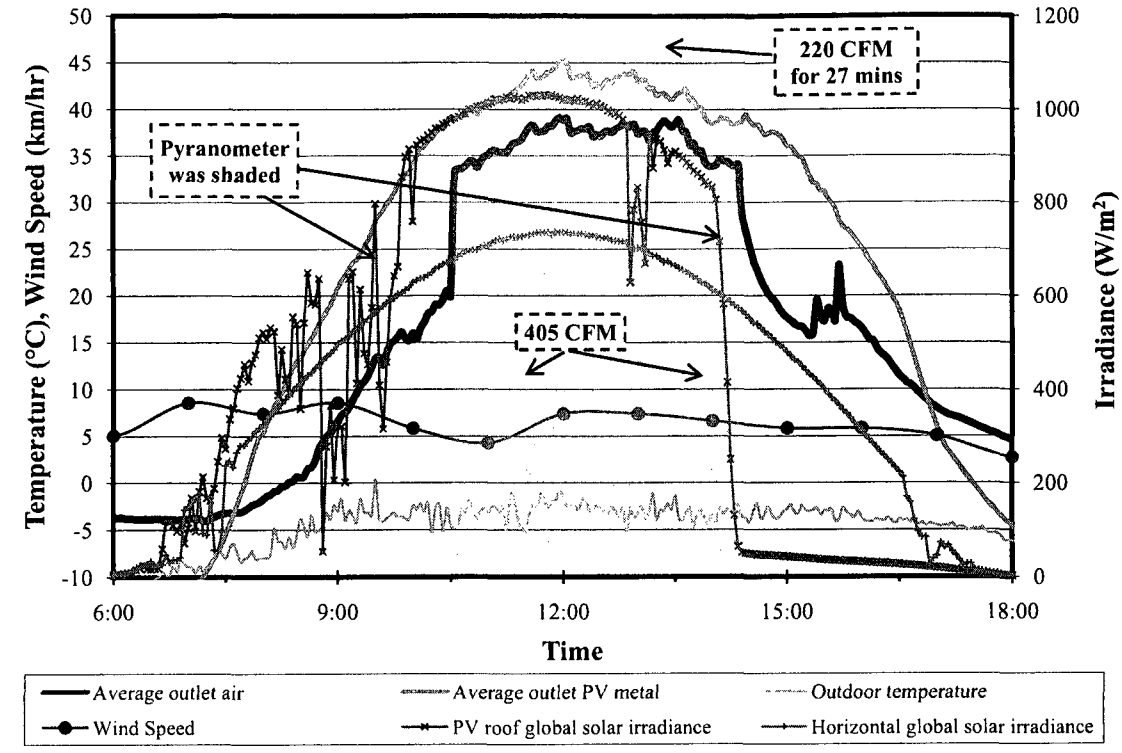

(a) Outlet temperatures and weather profiles

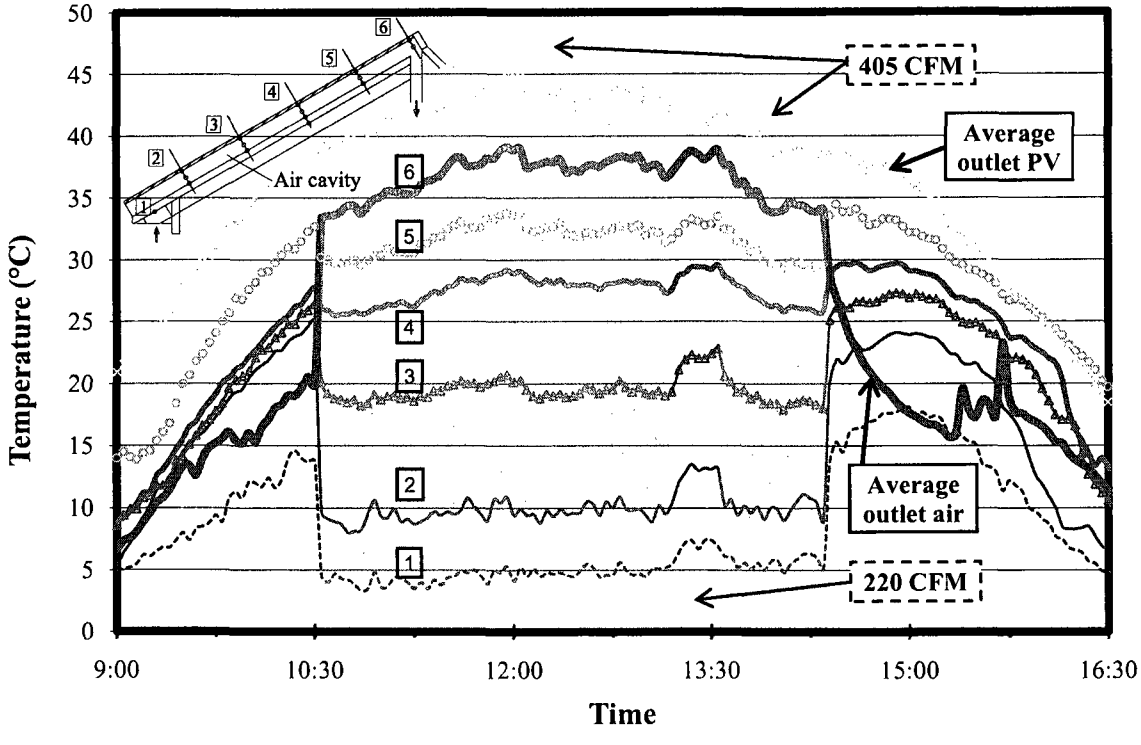

(b) Cavity air temperature profile

Figure 4.6: BIPV/T system temperatures on a cold sunny day, March 17^{th}, 2008

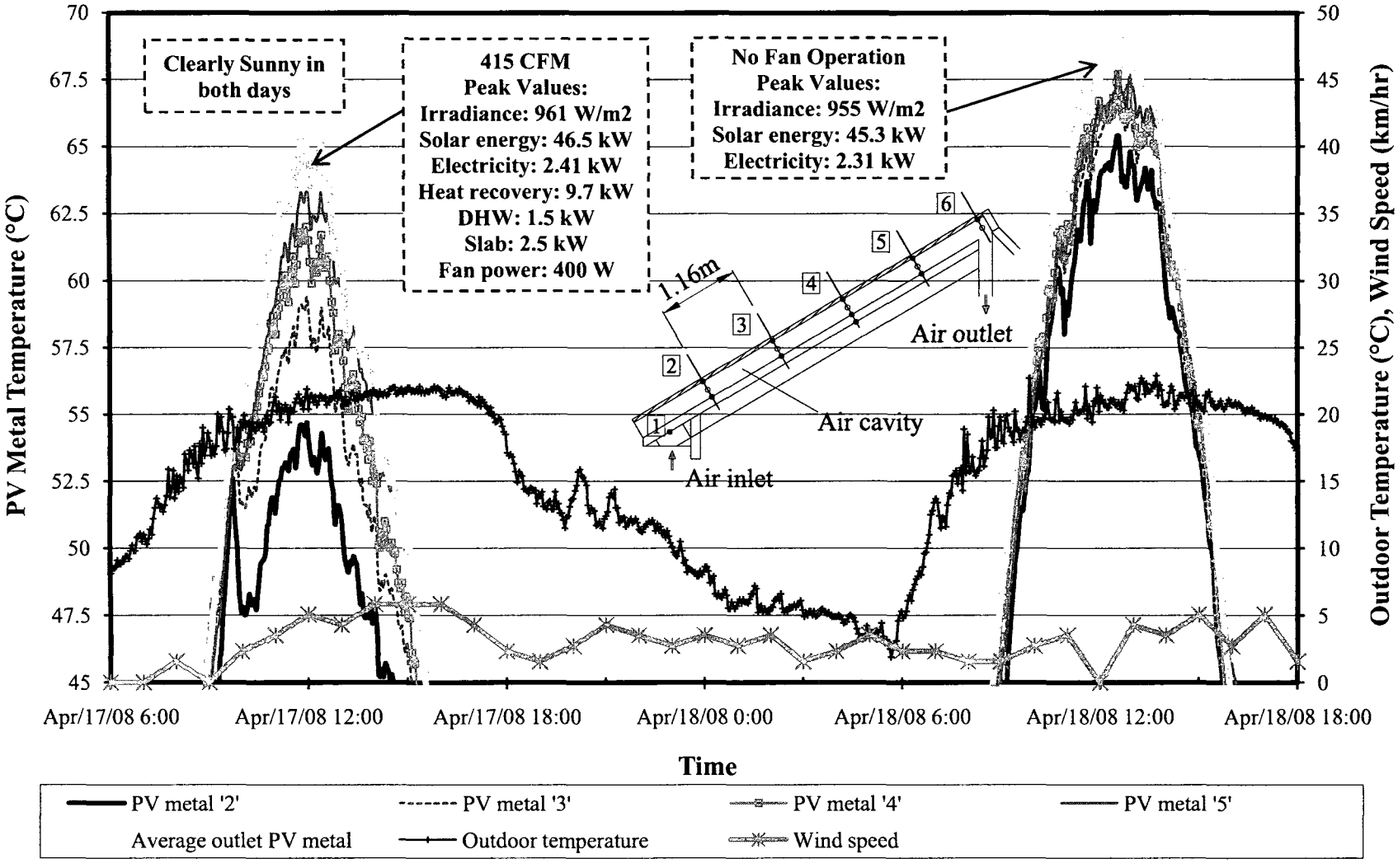

Figure 4.7: PV temperature profiles and effect of BIPV/T air flow on energy performance

Figure 4.6(b) shows the temperature profiles of the air as it flows upward. Near the end of the path (i.e. position "5" and "6"), the air temperature was already very close to the PV metal temperature (about 5 °C difference). During the test, when the flow rate was reduced from 405 CFM to 220 CFM, the temperature increase was marginal. The outlet air temperature was not affected significantly by lowering the cavity air velocity below a certain point (e.g. 405 CFM (0.58 m/s)). This will be further investigated in Section 4.4.

Two consecutive days, April 17^{th} and 18^{th} have identical weather conditions. Intentionally, no operation was conducted on April 18^{th}. By comparing the data from these two days, the advantages of the BIPV/T system and the PV-panel-cooling effectiveness can be evaluated (Figure 4.7). On April 17^{th}, at noon, 9.7 kW thermal energy was being collected from the BIPV/T roof. Among this thermal energy, 1.5 kW was used for DHW heating and 2.5 kW was used for VCS heating. Approximately 40% of the collected energy is useful. The PV panel temperature near the inlet was cooled down by about 10 °C; however, near the outlet, it was only about

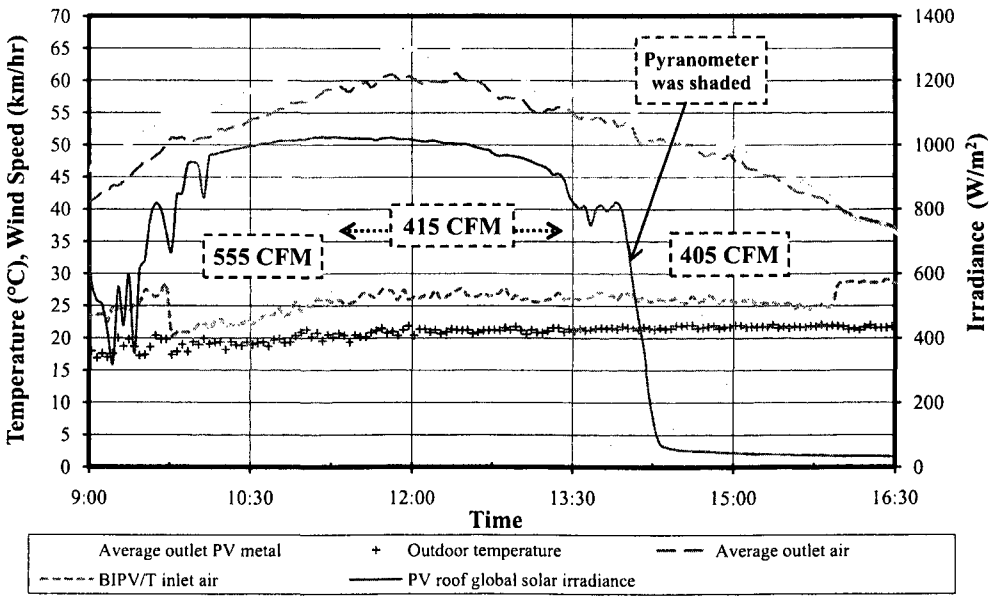

Figure 4.8: BIPV/T system temperatures on a warm sunny day, April 17^{th}, 2008

5 °C. Figure 4.8 shows the thermal performance of the BIPV/T system on the warm sunny day, April 17^{th}, 2008. The temperature increase of the air was 40 °C, as it was in Figure 4.6(a). This comparison shows that the solar irradiance intensity is critical in defining the increase of the air temperature as compared with outdoor air temperature. It's interesting to notice that the air is pre-heated by the south-facing facade and increased about 5 °C before it entered the BIPV/T roof.

The slight cooling effect did not significantly increase the efficiency of electricity generation, because the efficiency is defined by the highest temperature in the PV panel. The cooling effect from a larger flow rate is shown in Figure 4.9(b). An additional temperature decrease of 3 °C was gained. The improvement is not significant. This is because, when the air flow rate is increased, the fluid capacity rate and air velocity increase; however, the interior convective heat transfer coefficient $h_{c,pvt}$ increases as well due to higher air velocity (see Section 4.4). Also, because the air path is long (5.5 m), the air gains a lot of heat on its approach to the outlet. So, near the end of the air path, the air will still reach a temperature close to that of the air at lower speed. This implies that the air at higher speed is not able to extract more heat from the PV panels near the outlet. In order to increase the efficiency of electricity generation and take better advantage of the air ventilation, a better layout for the PV panels would have been to orientate the PV panels horizontally. In this way, the PV panels near the air inlet will have a higher efficiency because of having a lower peak temperature. For the panels near the top, however, their peak temperatures will remain almost the same.

On a warm partially cloudy day, June 25^{th}, air was drawing at a large flow rate of 580 CFM (velocity of 0.824 m/s). The BIPV/T still performed well (Figure 4.9(a)). It can also be observed that the thermal time constant is only about a few minutes. The monitoring time step is 3 minutes. Each marker represents one time step. It can

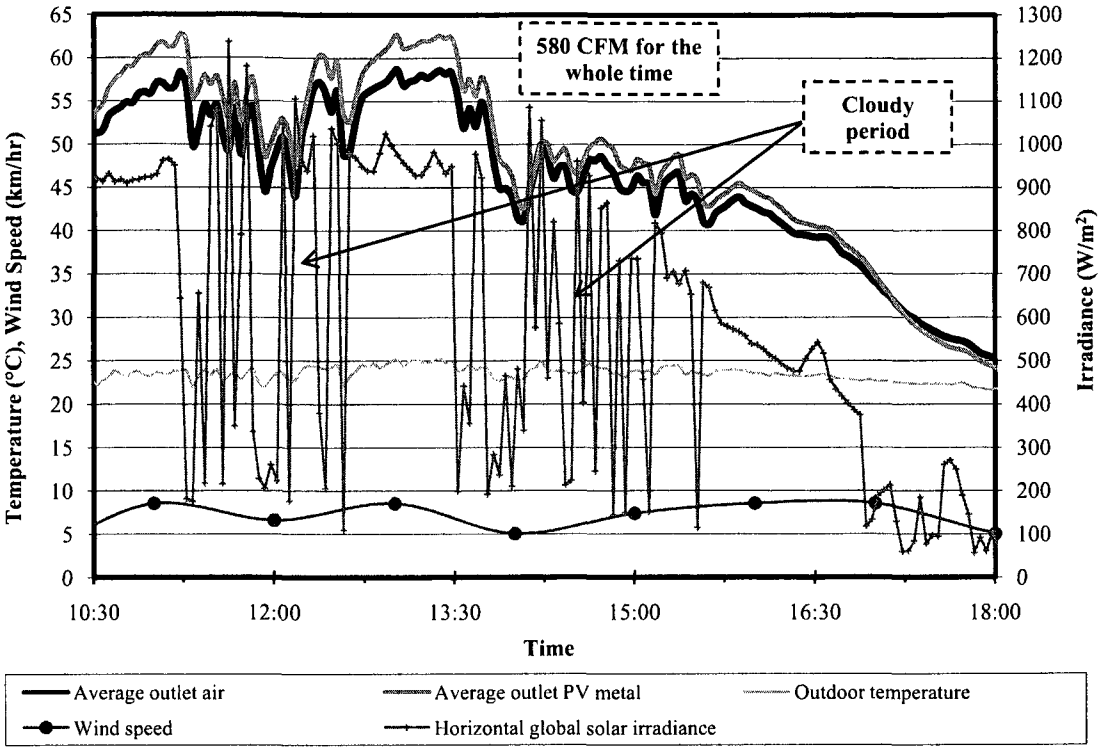

(a) Outlet temperatures and weather profiles

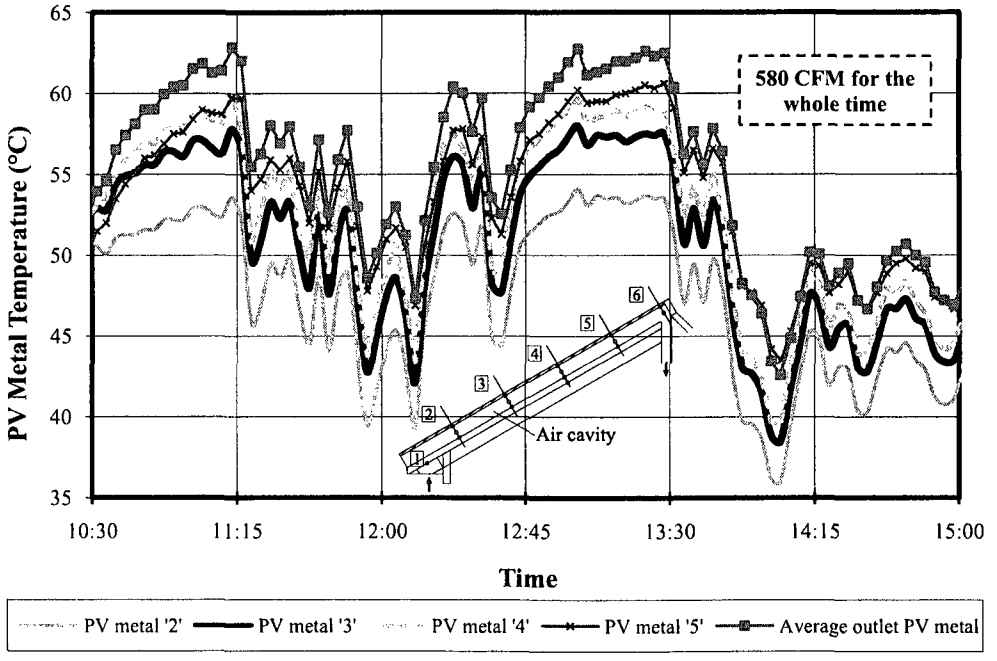

(b) PV metal temperature profiles

Figure 4.9: BIPV/T system temperatures on a warm and partially cloudy day, June 25^{th}, 2008

be seen that the profiles of temperatures followed closely with the solar irradiance profile. No long thermal lag appeared. This indicates that using a steady state model for hourly simulation is viable.

Figure 4.10 plots the BIPV/T thermal outputs vs. cavity air velocities from different data samples. The data samples are taken from different flow rates and arranged here in order from low to high air velocity. For each flow rate, samples are taken from at least two tests on two different days. It shows that, under almost the same conditions, the outlet air temperatures are the same for either low or high air velocity. For example, this can be seen at sample "200" and "500", and also at sample "70" and "470". This is because, when the air flow rate increases, the fluid capacity rate and air velocity of course will increase; however, the interior convective heat transfer

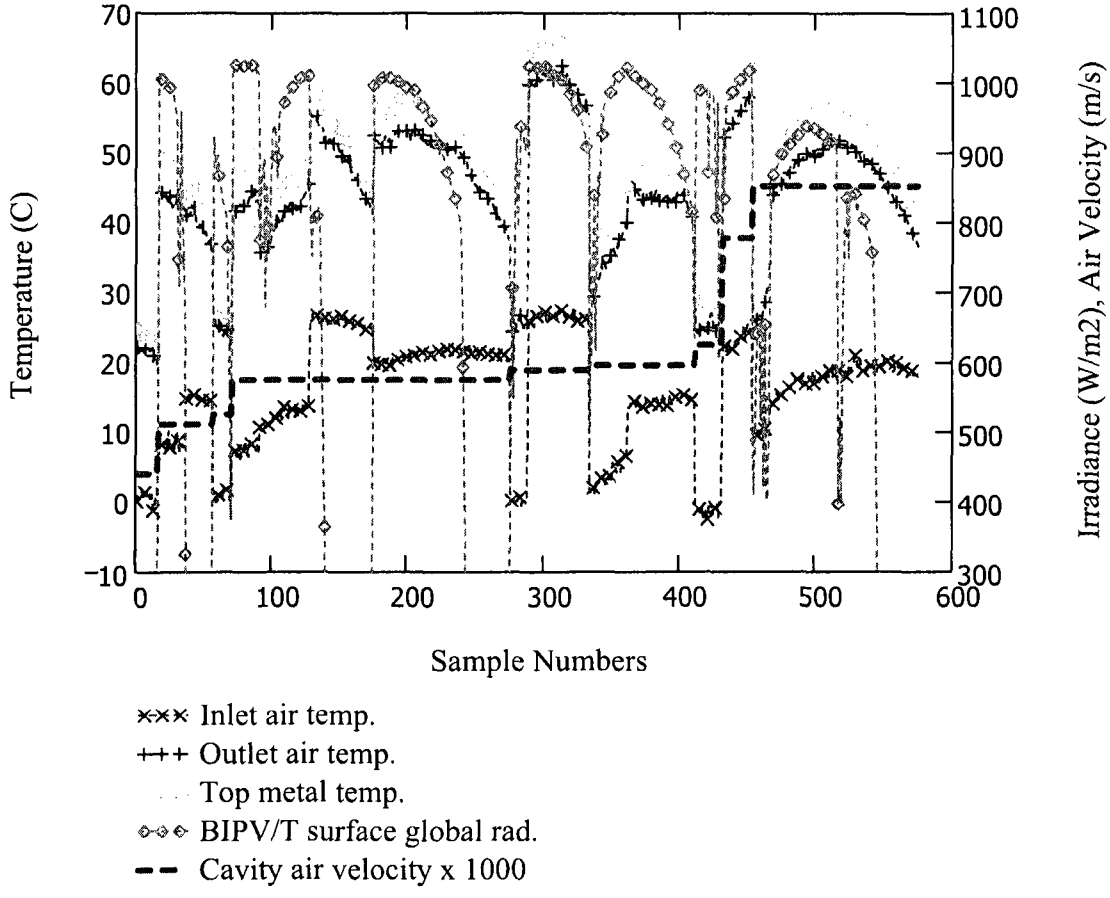

Figure 4.10: BIPV/T system temperatures vs. cavity air velocity

coefficient $h_{c.pvt}$ increases as well due to higher air velocity. It is beneficial in this case to use larger flow rates to improve thermal efficiency.

4.4 Interior CHTC Calculation

The Reynolds number was calculated to be 4100 corresponding to a maximum air velocity of 0.85 m/s (580 CFM) measured in the air cavity of the BIPV/T system. The characteristic length for the calculation of Reynolds number is twice the height of the air cavity [ASHRAE, 2005]. The Reynolds number range indicates that the heat transfer between the cavity air and its boundary is mixed convection within the transitional range. The control volume method is used for calculating the interior CHTC "$h_{c.pvt}$". On the roof, at position "1" and "6", the temperatures of the cavity bottom surface (top of the wooden sub-roofing) of the air cavity are not measured (Figure 4.4(a)). So, there are only three sections available to be used as control volumes for the CHTC calculation. These three sections are 'Lower section' between position "2" and "3", "middle section" between "3" and "4", and "higher section" between "4" and "5". At the inlets and outlets of these three sections, the temperatures of the top boundary (back of the PV metal), the air, and the bottom boundary are measured. Figure 4.12 shows the schematic of the control volume.

Figure 4.11 shows the temperature profiles of the top boundary, air, and bottom boundary at different positions in the BIPV/T air cavity for April 17^{th}. In these figures, temperature profiles are plotted against time (i.e. time is used for X-axis index). Temperature profiles along the air path (i.e. using "distance from the inlet" as X-axis index) can be found in Figure 4.17. The weather condition of the field operation on April 17^{th} can be found in Figure 4.7. As shown in Figure 4.11, the temperature of the air is very close to that of the bottom boundary. Closer to the

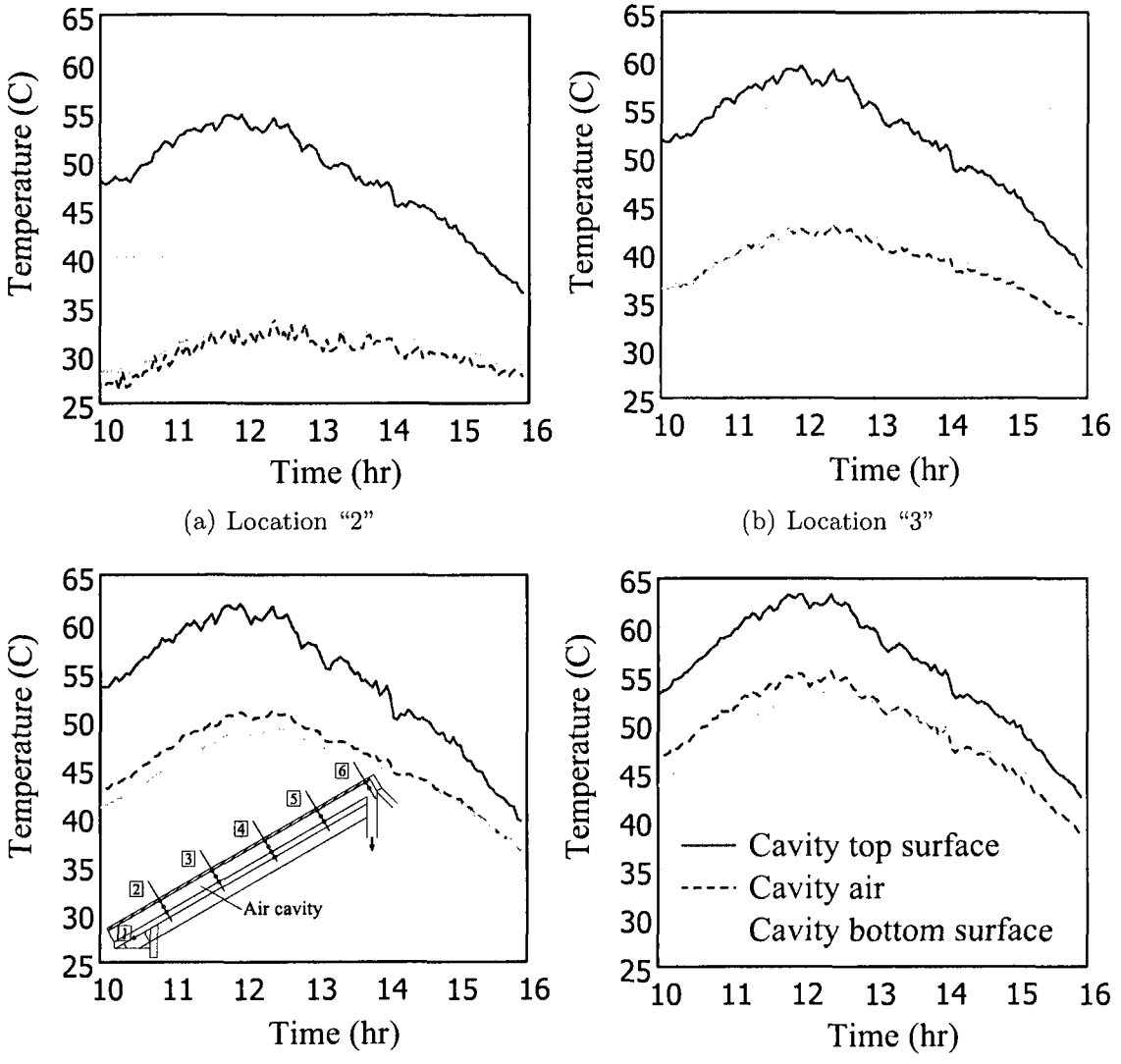

(a) Location "2"

(b) Location "3"

(c) Location "4"

(d) Location "5"

Figure 4.11: BIPV/T air cavity temperature profiles, April 17^{th}, 2008.

outlet, the air becomes hotter that the bottom boundary. The main direct heat source for the air is from the top boundary.

It is assumed that the heat flux between the bottom boundary and the air equals to the difference between $q_{top.to.btm}$ (the radiative heat flux from the top boundary to the bottom boundary) and $q_{btm.to.attic}$ (the conductive heat flux from the bottom boundary to the attic). The calculated CHTC based on this assumption will be the CHTC between the air and the top boundary. Since the back of the BIPV/T roof is

insulated with U value of about 1 $W/(m^2 \cdot K)$ (see Figure B.1 in Appendix B.1), it can be assumed that there is no heat loss through the back of the BIPV/T system, and all the radiative heat from the top received by the bottom boundary is transferred to the air. The calculated $h_{c.pvt}$ using the first assumption is about 2 to 3 $W/(m^2 \cdot K)$ higher than that using the second assumption. This is because there is heat loss from the bottom boundary to the attic space. In the following calculations, the first assumption is applied.

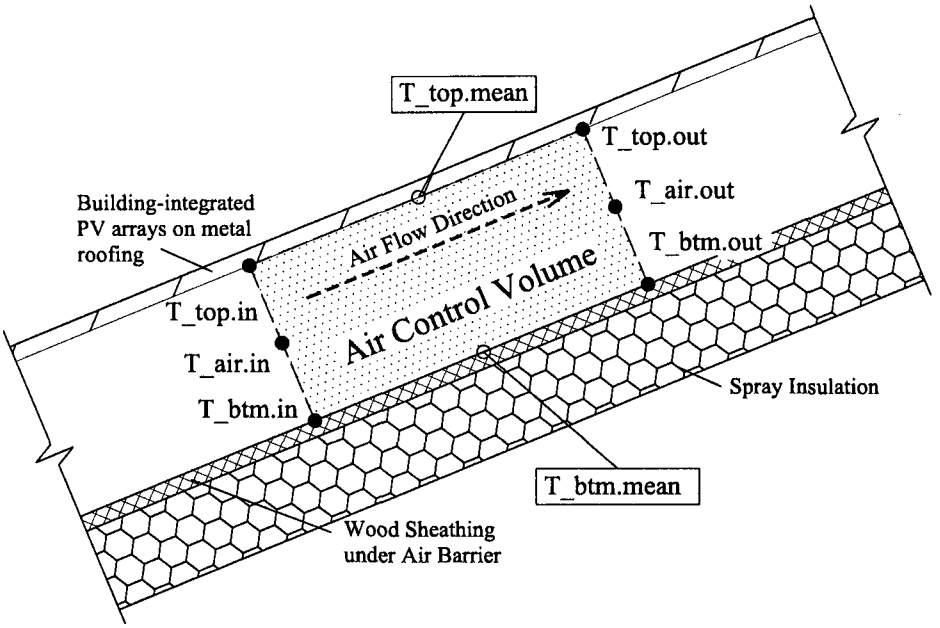

Figure 4.12: Schematic for control volume in BIPV/T system

Control volume energy balance equation

$$\begin{aligned} \Delta q_{air} &= q_{top.to.air} + q_{btm.to.air} \\ &= (T_{air.out} - T_{air.in}) \cdot (\dot{m}_{air} \cdot c_{p.air}) \end{aligned}$$

where

$q_{top.to.air} = h_{c.pvt} \cdot A_{top} \cdot (T_{top.mean} - T_{air.mean})$

$q_{btm.to.air} = q_{top.to.btm} - q_{btm.to.attic}$

$q_{top.to.btm} = \sigma_{SB} \cdot F_E \cdot F_A \cdot (T^4_{top.mean} - T^4_{btm.mean})$

Temperature is in kelvin.

$\dot{m}_{air}$ is the mass flow rate of air.

A_{top} is the area of the top boundary.

σ_{SB} is the Stefan-Boltzmann constant, $5.670 \times 10^{-8}\ W/(m^2 \cdot K^4)$.

F_A is the angle factor of 1.

F_E is the emissivity factor of 0.82.

Arithmetic mean temperature is used here for mean temperature. Note that if the temperature difference at the inlet is not more than 50% greater than that at the outlet, the arithmetic mean temperature difference will be within 1% of the log mean temperature difference (LMTD) and may be used to simplify calculations [Kreith and Bohn, 2001]. This is the case in this study. The convective coefficient $h_{c.pvt}$ is then calculated using:

$$h_{c.pvt} = \frac{\Delta q_{air} - q_{btm.to.air}}{(T_{top.mean} - T_{air.mean}) \cdot A_{top}}$$

Figure 4.13 shows the calculated $h_{c.pvt}$ for one test day. As it can be seen, the calculated CHTC is increasing as time passes. This phenomenon can also be observed from the calculations for other test days. This is possibly due to the flow rate decreasing as time passed during the operations. The recorded data shows that the fan power output (i.e. fan power consumption) was constant for each fan power signal set by the control system in that speed period. The flow rate changes could be due to the changes of the thermal gravity effect[5] (stack effect) [ASHRAE, 2005, Ch. 35] . For the duct system in ÉcoTerra, air goes down from the warm environment (i.e. BIPV/T outlet) to the relatively cool environment (i.e. the basement). When the

[5] $\Delta P = g\,(\rho_{in} - \rho_{out})\,(z_{out} - z_{in})$, *in* is inlet; *out* is outlet; ρ is the density of air; z is the elevation from datum. When ΔP is positive, flow is assisted.

warm air was being drawn down to the house through the duct, the duct was being warmed up. When the bottom part of the duct line is warmer, it provides smaller flow assistance. Note that when the capture hood was used to measure the flow rate, the measurements were only conducted at the beginning of each test. BIPV/T experiments in other Concordia research facility show the same phenomenon: flow rate becomes lower as time passes. This phenomenon needs to be further investigated.

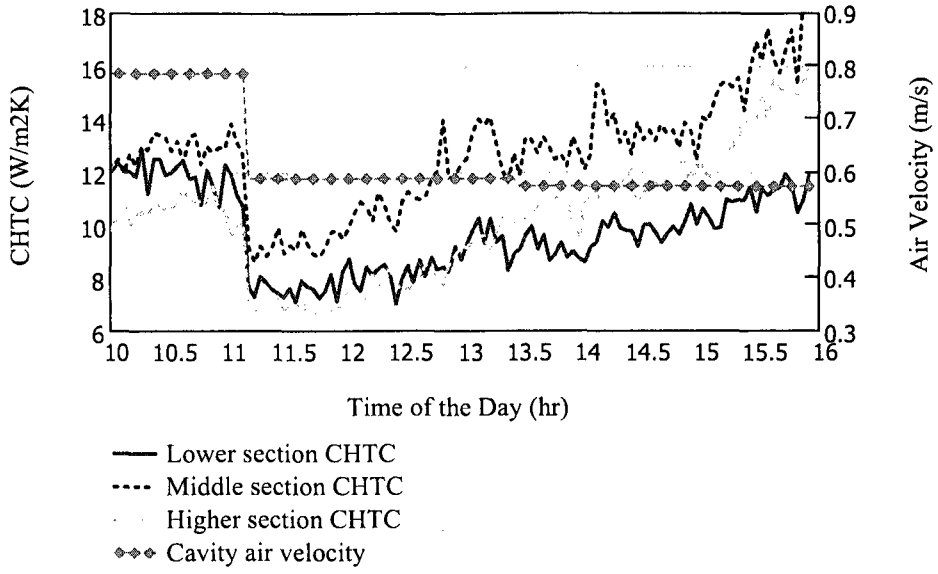

Figure 4.13: Calculated CHTC vs. air velocity for April 17^{th}, 2008

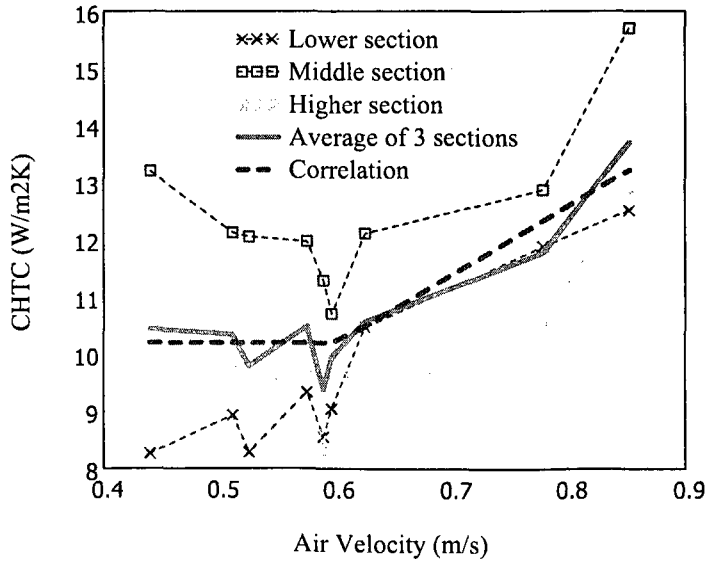

Figure 4.14: Average CHTC of each section and all sections vs. air velocity

Using data from different full-scale measurements, the $h_{c.pvt}$ is calculated for each air velocity. Figure 4.14 shows, for each section, the average $h_{c.pvt}$ for each air velocity. The average of the three sections is also plotted. When the air velocity is lower than 0.6 m/s, the $h_{c.pvt}$ remains at about 10.5 $W/(m^2 \cdot K)$. For air velocity larger than 0.6 m/s, it shows an almost linear increase as a function of the air velocity. A two-stage correlation Eq. 4.1 is adopted here, and plotted in Figure 4.14.

$$h_{c.pvt} = \begin{cases} 10.2 & (v_{air.pvt} \leq 0.6\ m/s) \\ 12 \cdot v_{air.pvt} + 3 & (v_{air.pvt} > 0.6\ m/s) \end{cases} \quad [W/(m^2 \cdot K)] \tag{4.1}$$

where

$v_{air.pvt}$ is the air velocity inside the cavity $[m/s]$.

4.5 Modeling and Simulation

4.5.1 Exterior CHTC

In cases where collectors have no covers or are un-glazed (such as the case in ÉcoTerra), a large portion of the heat on the collector surface could be extracted by the exterior free stream air. It's shown in literature that more than 40% of the heat absorbed on the uppermost surface could be released to the free stream air [Sharples and Charlesworth, 1998]. Hence, wind-induced external CHTC on the uppermost surface of roof-mounted BIPV/T system '$h_{c.wd}$' is an important factor in simulation. It directly affects the thermal output of the BIPV/T system.

Sharples and Charlesworth [1998] conducted full-scale measurements of wind-induced convective heat transfer from a roof-mounted flat plat solar collector. The filed measurements showed a slight variation in the $h_{c.wd}$ with wind direction. For a given

wind speed, $h_{c.wd}$ is at its lowest value when the surface is leeward. However, the variations have no pattern and cannot be correlated with wind direction. By comparing with their own developed correlations, correlation 4.2 from Test et al. (cited by Sharples and Charlesworth [1998]) gives approximately the average $h_{c.wd}$ among those from correlations of Sharples and Charlesworth for different wind directions.

$$h_{c.wd} = 2.56 \cdot V_{1m} + 8.55 \ \left[W/(m^2 \cdot K)\right] \tag{4.2}$$

where

V_{1m} is wind speed measured at a height of 1 meter above the plate $[m/s]$.

Palyvos [2008] presented a survey for the available correlations for $h_{c.wd}$ in the literature and tabulates the correlations on the basis of algebraic form of the coefficients and their dependence upon characteristic length and wind direction, in addition to wind speed. The author proposed the following two correlations. They are the purely empirical "average" correlation of other correlations from literature. The maximum deviations from the predictions of other individual correlations are 18% for Eq. 4.3 and 22% for Eq. 4.4.

$$h_{c.wd} = 4.0 \cdot V_f + 7.4 \ \left[W/(m^2 \cdot K)\right] \ (windward) \tag{4.3}$$

$$h_{c.wd} = 3.5 \cdot V_f + 4.2 \ \left[W/(m^2 \cdot K)\right] \ (leeward) \tag{4.4}$$

where

V_f is free stream wind speed at 10 m above roof $[m/s]$.

Figure 4.15 shows the comparison between Eq. 4.2 and Eq. 4.4. It can be seen that the predictions from both equations are close. In this study, since the prevailing wind direction is from north-west (i.e. from the back of the south-facing BIPV/T system)

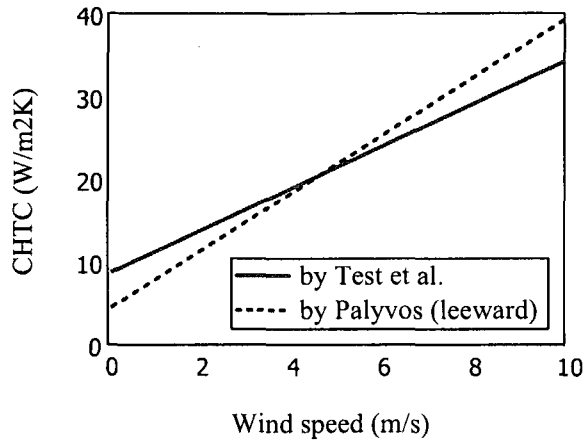

Figure 4.15: Comparison of wind-induced CHTC correlations

correlation 4.4 is used for the $h_{c.wd}$ calculation in simulation.

4.5.2 Modeling

A one dimensional explicit finite difference technique, steady state model and upwind scheme [Patankar, 1980] are adopted in modeling the BIPV/T system. Figure 4.16 shows the thermal network of the model. Correlation 4.1 is used for the CHTC of both the top and the back surfaces. Actually, preliminary CFD simulations from other researchers in Concordia show that the CHTC of the top and the back surfaces are approximately the same except the places very close to the wood battens.

Sky temperature For the calculation of the radiative heat transfer between sky and BIPV/T top surface, the following equation from Duffie and Beckman cited in [Davies, 2004] is used for effective sky temperature:

$$T_{sky} = T_{ext} \cdot (0.8 + \frac{T_{dp} - 273}{250})^{0.25}$$

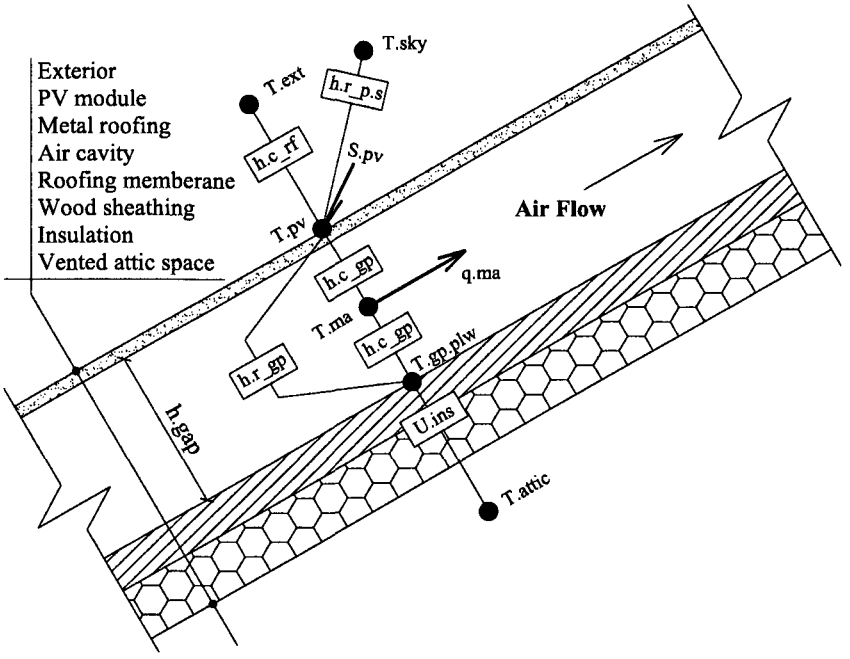

Figure 4.16: 1D Thermal network of the BIPV/T system

where

T_{ext} is exterior temperature.

T_{dp} is dew point temperature.

Temperatures are in kelvins (numerical value only).

Grid size A grid size (length along the air path) of 0.15 meters (36 sections for an 18 ft long path in this case) is used to predict the out air temperature to a satisfactory degree. Using a grid with larger control volume size results in a gentler profile (less steep). For example, 0.3-meter grid results in roughly 2°C lower in the temperatures of the PV metal, air and back surface at outlet. This will result in an error of about 5% considering the typical air temperature increase ranges from 30 to 40°C.

Upwind scheme numerical simulation

$$T_{air}^{i} = \frac{F_{air} \cdot T_{air}^{i-1} + h_{c.pvt} \cdot A_{step} \cdot (T_{top}^{i} + T_{btm}^{i})}{F_{air} + 2 \cdot h_{c.pvt} \cdot A_{step}}$$

$$T_{top}^{i} = \frac{h_{r.top.sky} \cdot T_{sky} + h_{c.wd} \cdot T_{ext} + h_{c.pvt} \cdot T_{air}^{i-1} + h_{r.top.btm} \cdot T_{btm}^{i} + I_a \cdot (1 - \mu_{PV})}{h_{r.top.sky} + h_{c.wd} + h_{c.pvt} + h_{r.top.btm}}$$

$$T_{bottom}^{i} = \frac{u_{btm.attic} \cdot T_{attic} + h_{c.pvt} \cdot T_{air}^{i-1} + h_{r.top.btm} \cdot T_{top}^{i}}{u_{btm.attic} + h_{c.pvt} + h_{r.top.btm}}$$

where

$F_{air} = \dot{m}_{air} \cdot c_{p.air}$

$h_r = \sigma_{SB} \cdot F_E \cdot F_A \cdot (T_1^2 + T_2^2) \cdot (T_1 + T_2)$

$\dot{m}_{air}$ is the mass flow rate of air.

I_a is the absorbed solar radiation.

μ is the efficiency of electricity generation. It is a function of the temperature of the PV panel.

Figure 4.17 shows that the simulated temperature profiles match well with the measurement. Using the model developed here, the air and PV temperatures at outlet are simulated under different exterior temperatures and air velocities in the cavity (Figure 4.18). The solar irradiance and the free stream wind velocity for the simulation are assumed to be 900 W/m^2, and 15 km/hr, respectively. From Figure 4.18, it can be seen that the temperature increase of the outlet air is almost independent of the exterior temperature, so is the temperature difference between the PV and the exterior.

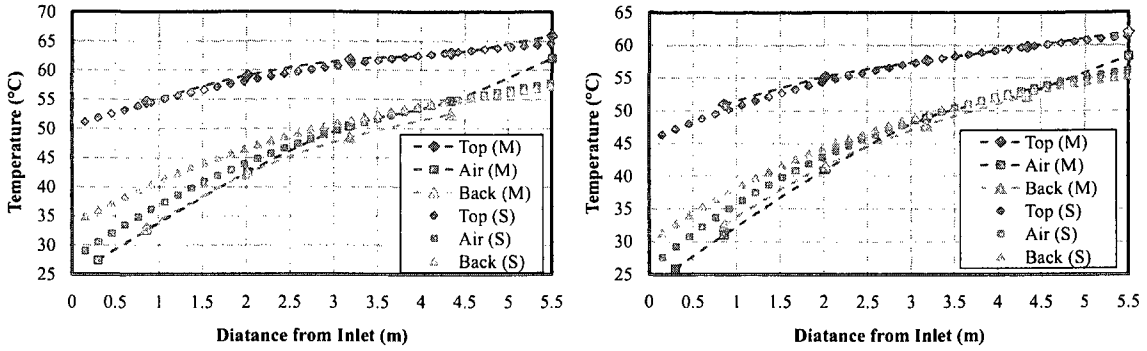

(a) April 17, 2008 11:46 (b) April 17, 2008 13:00

Figure 4.17: Comparison of simulated and measured BIPV/T system temperatures (M: measured; S: simulated)

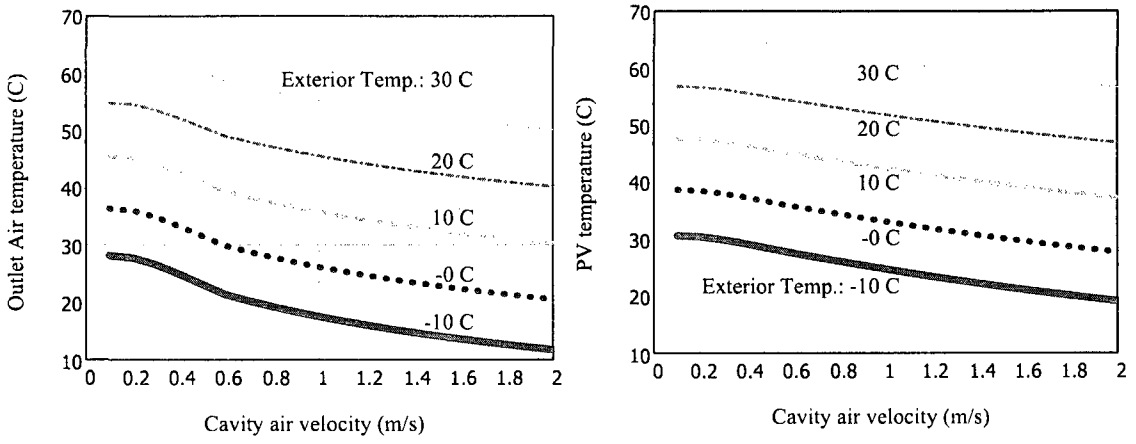

(a) Air temperature (b) PV temperature

Figure 4.18: Simulated temperatures at outlet under different exterior temperatures

4.6 Conclusions

This chapter presents a comprehensive study of the BIPV/T system in ÉcoTerra, including the field measurement, the calculation of CHTC inside the air space, the correlation for wind-induced CHTC on the uppermost surface, and the modeling of the BIPV/T system. The construction of the BIPV/T system is based on mature construction technologies. It is practical, reliable, and simple. Prefabrication of the BIPV/T roof ensures high-quality construction in terms of air tightness, thermal insulation and balance of pressure drop. The data from field measurements indicate

that the BIPV/T system functions very well. It is able to collect a considerable amount of solar thermal energy, and meanwhile, cool down the PV panels. A simple one-dimensional finite difference model is created to simulate the thermal performance of the BIPV/T system. The model is proved to be satisfactory for design and control purposes.

For future improvement and study, the followings are recommended:

- The BIPV/T roof discussed above is a prototype model. The cost-effectiveness and methods for lowing cost need to be investigated, such as the possibility of mass production.

- The efficiency of electricity generation could be improved from the current situation. This can be done through a better layout - orientating the PV panels horizontally. Following the temperature gradient along the air path, the PV panels near the air inlet will have a lower peak temperature, and hence have a higher efficiency.

- An accurate flow rate measuring device is needed in order to pursue a more detailed study of the CHTC inside the air cavity. Detailed CFD studies are also helpful.

- The optimization of the length of the air path, the air flow rate, and the air cavity height needs further investigation. In the cases presented in this chapter, the outlet air temperature at a relatively high air velocity (0.85 m/s) is almost the same as that at a low velocity (0.5 m/s). This is because higher air velocity induces a higher heat transfer between the air and the surfaces. Further increases due to higher air velocity or different geometries of the air cavity may be possible. A roughened, or finned top boundary surface could be employed to enhance the heat transfer as well [Webb, 1987; Saini and Saini,

1997; ASHRAE, 2005; Saini and Verma, 2008]. However, the trade-off for pressure drop should be kept in mind. The length of the air path might be shortened if the heat gain by the air is marginal near the end.

- A dimensionless analysis would improve the liability and applicability of the numerical thermal model.

Chapter 5

Ventilated Concrete Slab

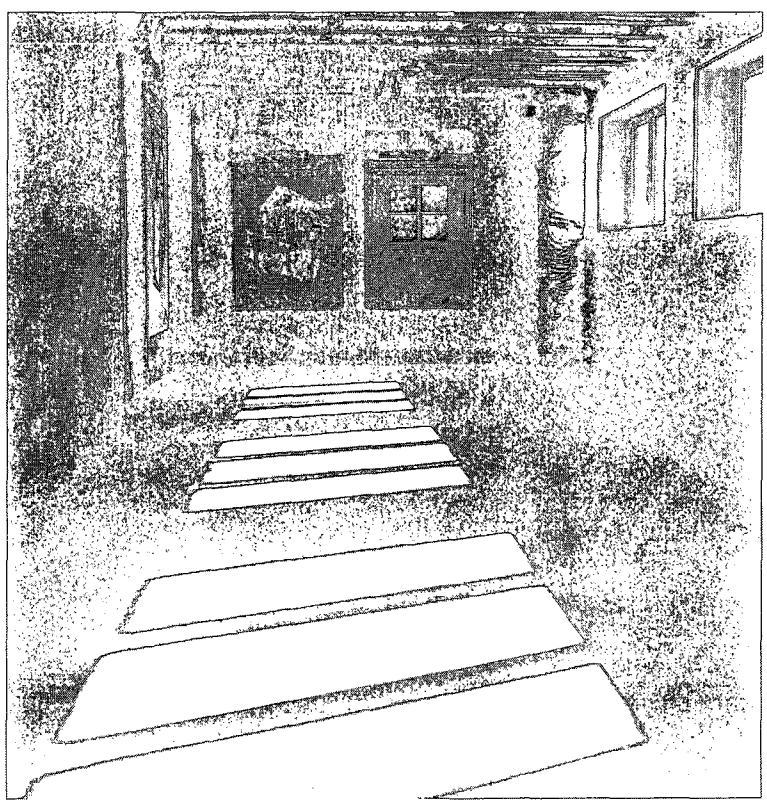

Figure 5.1: Ventilated concrete slab located in basement

A ventilated concrete slab (VCS) (Figure 5.1) is adopted in the solar house ÉcoTerra (Chapter 3). It stores the heat collected by the roof-mounted BIPV/T system (Chap-

ter 4). In this chapter, field measurements, and modeling of the thermal performance of the VCS are presented. The construction details of the VCS and the study of the thermophysical properties of the concrete are included in Appendix C.

5.1 Introduction

Implementing a VCS as an active thermal energy storage (TES) system is one of the techniques selected to help ÉcoTerra achieve close to net-zero annual energy consumption. The stored heat would be released passively into the living space through its top surface by natural convection.

A VCS is an active TES system that uses structural mass as thermal mass. It stores the thermal energy from the air passing through its hollow cores. The stored thermal energy can be released to the living space passively by natural convection, or actively by circulating air through its core to extract heat from the slab. Mechanical ventilation through the internal hollow cores of thermal mass enhances the convective heat transfer coefficient and utilizes a larger heat transfer area than natural convection on outer surfaces alone. Hence, the heat transfer rate is significantly increased. Consequently more thermal mass can be utilized and less time is needed for storing the same amount of thermal energy. The thermal storage effectiveness is considerably increased. The geometry of the cross section significantly affects the heat transfer rate between the surface of hollow cores and the air [Chen et al., 2008]:

- The total cross section area of all air channels determines the air velocity
- The cross section geometry (i.e. height and width) determines the hydraulic diameter.
- The Reynolds number is based on the air velocity and the hydraulic diameter.

It determines the CHTC.

- The cross section perimeter and the CHTC define the conductance U_c per unit meter channel length (unit: $W/(m \cdot K)$).

The VCS to be adopted has the following requirements:

- Efficiently store of the thermal energy collected by the BIPV/T system.
- Avoid overheating the top surface. The comfortable temperature range for concrete slab surface (no cover) is between 26 and 28.5 °C for people with bare feet [ASHRAE, 2005, Ch. 8]; and 19 and 29 °C for wearing lightweight indoor shoes in office environment [ASHRAE, 2004]. The latter temperature range is applied in this research.
- Release the stored thermal energy passively at an appropriate rate into the living space to avoid space overheating.
- Serve as a structural component. The slab should not be added as a non-structural component.

A new type of VCS is developed to satisfy these design requirements (Figure 5.2 and 5.3). It is located in the basement (Figure A.5). The concrete was poured on the steel decks to form air channels to allow air to pass through the slab. In order to have a higher convective heat transfer coefficient (CHTC) inside the channels, a layer of metal mesh was placed under the steel deck to increase the roughness of the channel. The metal mesh also distributes the structural load from the flutes (the bottom 38-*mm* extrusion) of the steel deck to the rigid insulation form - Extruded Polystyrene (EPS) underneath. The compressive strength of the EPS ranges from 25 to 140 *psi*[1]

[1]National Research Council Canada. `http://irc.nrc-cnrc.gc.ca/pubs/cbd/cbd167_e.html`

(from 170 to 960 kPa) at 5% deflection. The calculated maximum actual stress on the EPS from the flute due to the combined load is about 20.5 kPa[2], which is much smaller than the compressive capacity of the EPS. The cross sectional area of each air channel is 77 cm^2. There are a total of 19 channels used for ventilation in the slab. The total area of the cross section of the 19 hollow cores is 0.14 m^2. 125-mm thick concrete was poured on top of the steel deck[3]. The volume of the concrete of the VCS is about 5 m^3. The air inlet (northwest corner) and outlet (southeast corner) (Figure 5.3) of the VCS is located at the two diagonally opposite corners. This reverse-return layout ensures the balance of the pressure drop.

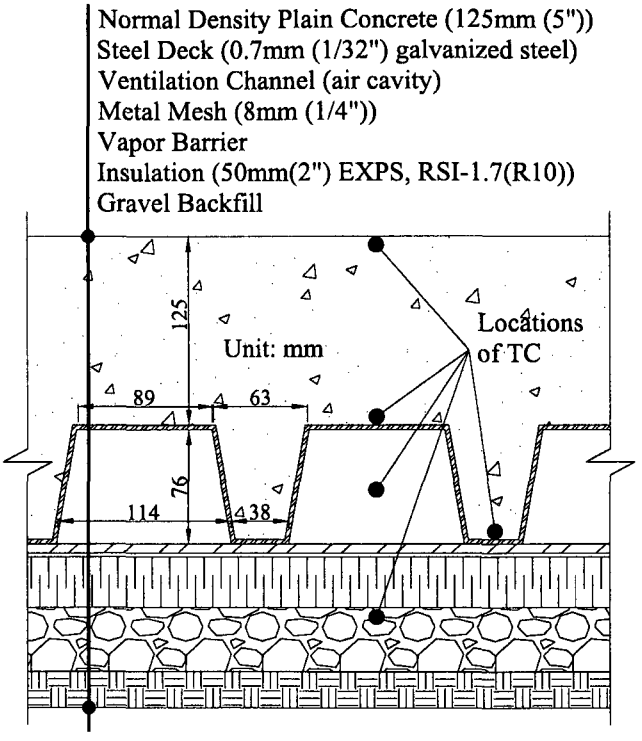

Figure 5.2: Cross section of VCS and monitoring locations

Placing the VCS on grade in the basement has two advantages. One of the advantages is that the construction of the air distribution system is simple: the manifolds and the steel decks are placed directly on grade (with rigid insulation). No structural support

[2]National Building Code of Canada, 2005. The factored dead load (i.e. the concrete slab) is 17.5 kPa; and factored live load (occupants, furniture, etc) is 3 kPa.

[3]The design value is 100 mm. This discrepancy is due to the imperfect workmanship.

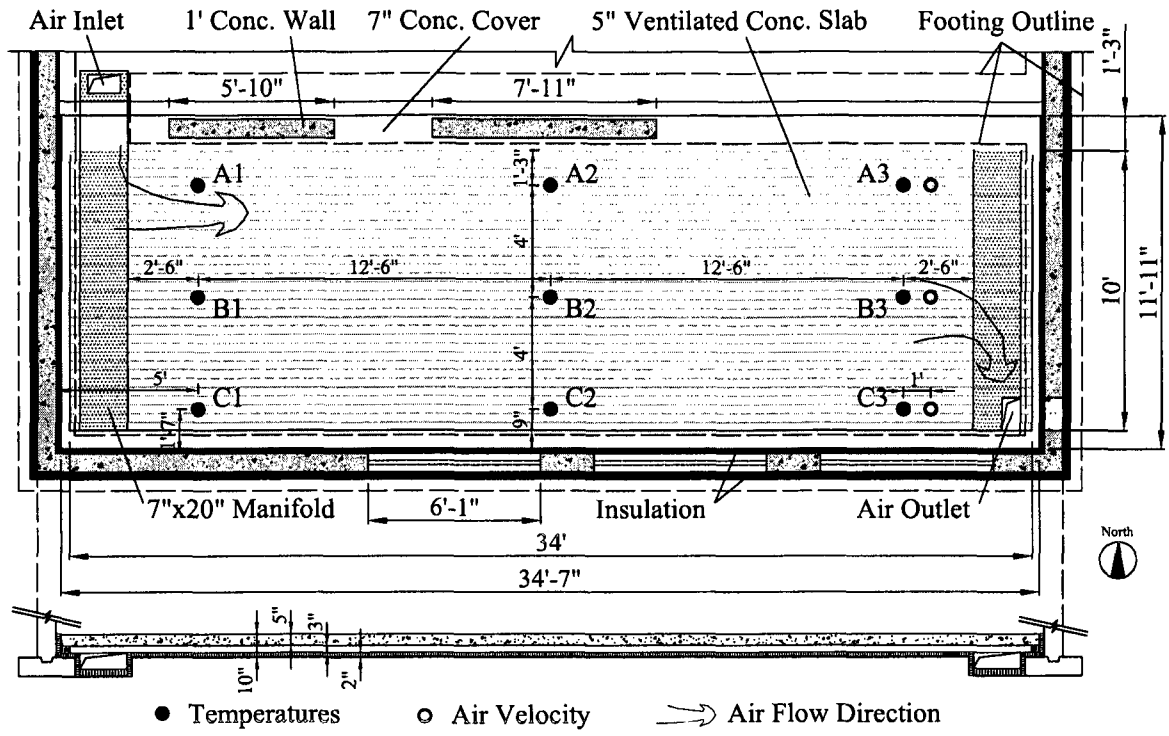

Figure 5.3: Plan and longitudinal cross section of VCS, and monitoring locations

is needed. Because the air channels and the manifolds are surrounded by the concrete poured on top and the water barrier and soil underneath, the air-tightness of them can be easily accomplished. This advantage also implies low cost. Another advantage is that the VCS can store more thermal energy efficiently: lower inlet air temperature and larger allowable temperature rise. The slab temperature before charging is lower than that of the other floors. This is because the basement is colder than other living spaces due to temperature stratification. However, the accompanying disadvantage is the passing warm air and the heated concrete lose their heat to the soil under the insulation. This can be prevented by proper insulation.

The design of the VCS is interrelated with the design of the house and the BIPV/T roof. The design and sizing of the steel deck (e.g. length, cross section geometry, and quantity of the air channel) and the concrete slab (e.g. the amount of concrete and its thermophysical properties) take into account the thermal capacitance and

heating load of the house, the thermal energy output of the BIPT/T roof (e.g. air temperature and flow rate), the geometry of the basement, the CHTC inside the VCS channels, the thermal capacitance of the VCS, the prevention of top surface overheating of the VCS, and the structural design issues. The design was optimized based on comprehensive simulations ran using customized thermal model, which connects the VCS model to the whole house model and performs transient simulation simultaneously for the BIPV/T roof, the VCS and the whole house. Chen et al. [2007, 2008] described the preliminary design of the VCS.

Control of the flow affects the thermal energy recovered from the roof and also the air supply temperature to the VCS. Generally, the higher the flow rate, the more thermal energy is recovered by the BIPV/T system, but the temperature of the supply air to the slab (i.e. the outlet air from the BIPV/T system) is lower. The flow rate also affects the CHTC inside the channel. As the flow rate increases, the energy spent on fan electricity consumption increases rapidly (approximately proportional to the square of the flow rate). The desirable air temperature for heating the VCS could be just 3 to 10°C higher than room temperature. The flow rate is controlled through a variable speed fan to achieve optimum heat recovery and air supply temperature to the VCS.

5.2 Monitoring Approach

The VCS is heavily instrumented. Thermocouples are installed to monitor the temperature distribution. The time step of recording the temperatures is 3 minutes. The total flow rates and corresponding pressure drops are measured manually.

Temperature The temperatures at different locations of the VCS are closely monitored. "T" type (copper-constantan) thermocouples with accuracy of $\pm 0.5\,^{\circ}C$ were used. Figure 5.2 and 5.3 show the locations of the temperatures measuring points. There are 4 thermocouples in each of these 9 locations, measuring the temperatures of the soil just under the insulation, in the middle of the cavity (i.e. air temperature), the middle layer (just above the steel deck), and the top layer of the slab (Figure 5.2). At locations "A2", "B2", and "C2", the temperatures of the bottom layer of the slab are also monitored. Inlet and outlet air temperatures are measured right before and after the slab inlet and outlet, accordingly. The recorded values are instantaneous and the time step of recording temperature data is 3 minutes.

Flow rate and pressure drop Total flow rates were measured at the outlet of the VCS as described on page 65. Table 5.1 shows the measured pressure drops under different corresponding flow rates. The pressure drops were measured between the inlet and outlet manifolds using a hand-held digital manometer. The values show that the pressure drops are relatively low.

Table 5.1: Measured pressure drop vs. flow rate

Total Flow Rate (CFM)	220	300	360	405	420
Pressure Drop across VCS (kPa)	0.01	0.03	0.05	0.06	0.07

Figure 5.3 shows the three locations for measuring the air velocities inside the air channels of the VCS. The velocities inside the channels were measured only in one site test. The velocities measured at these locations are very close to each other. This indicates that the mass flow rate is well balanced and the reverse-return strategy is applied successfully. The air flow from the inlet is evenly distributed into the 19 channels. In the following site tests, the air flow was assumed to be evenly distributed. The correlation between the total flow rate and the corresponding air velocity in each channel is $TotalFlowRate(CFM) = AirVelocity(m/s) \times 315$.

5.3 Thermal Performance

Various site tests were conducted under different flow rates and temperatures of the inlet air. The recorded temperatures within the slab and of the air from these site tests were used to assess the thermal performance of the VCS and optimize the integrated operation of the VCS-BIPV/T system.

The transmitted solar radiation can reach the top surface of the VCS. In order to assess the capability of thermal energy storage without being affected by the solar gain, one test was conducted during an overcast day (March 3^{rd}, 2008). The inlet air was heated artificially before entering the slab. In the testing period, the south facade global irradiance was below 100 W/m^2. So the transmitted solar radiation was below 50 W/m^2, considering the solar transmittance of the window is lower than 0.5. During the 5-hour testing period, the flow rate was maintained at about 310 CFM (1 m/s air velocity in the air channel). Figure 5.4 shows the temperature profiles of the air as it was passing through the ventilated slab in three different channels "A", "B" and "C" (Figure 5.3). This graph indicates that, as expected the heat transfer is high in the inlet manifold due to the high turbulence.

Figures 5.5 shows the temperature distributions at different layers of the VCS during the site test. The plotted values are interpolated based on the 9 measurement points of each layer (see Figure 5.2 and 5.3 for sensors' locations). The effects of the inlet and outlet manifolds are not shown here due to the incomplete instrumentation. Full-scale measurements indicate that air flow is evenly distributed in the air channels; however, the temperature distribution across the air channels is not even. A considerable amount of heat is stored near the inlet manifold (Figure 5.5). The further the air channel is away from the inlet, the lower the temperature of the entering air (Figure 5.4).

As shown in Figure 5.5, the temperature gradient on the top surface along the direction of the air flow is about 4°C for 10 meters. The temperature difference between the top surface and the center layer of the slab is less than 0.5°C. This is because the inlet air temperature and flow rate were not high. Stored thermal energy

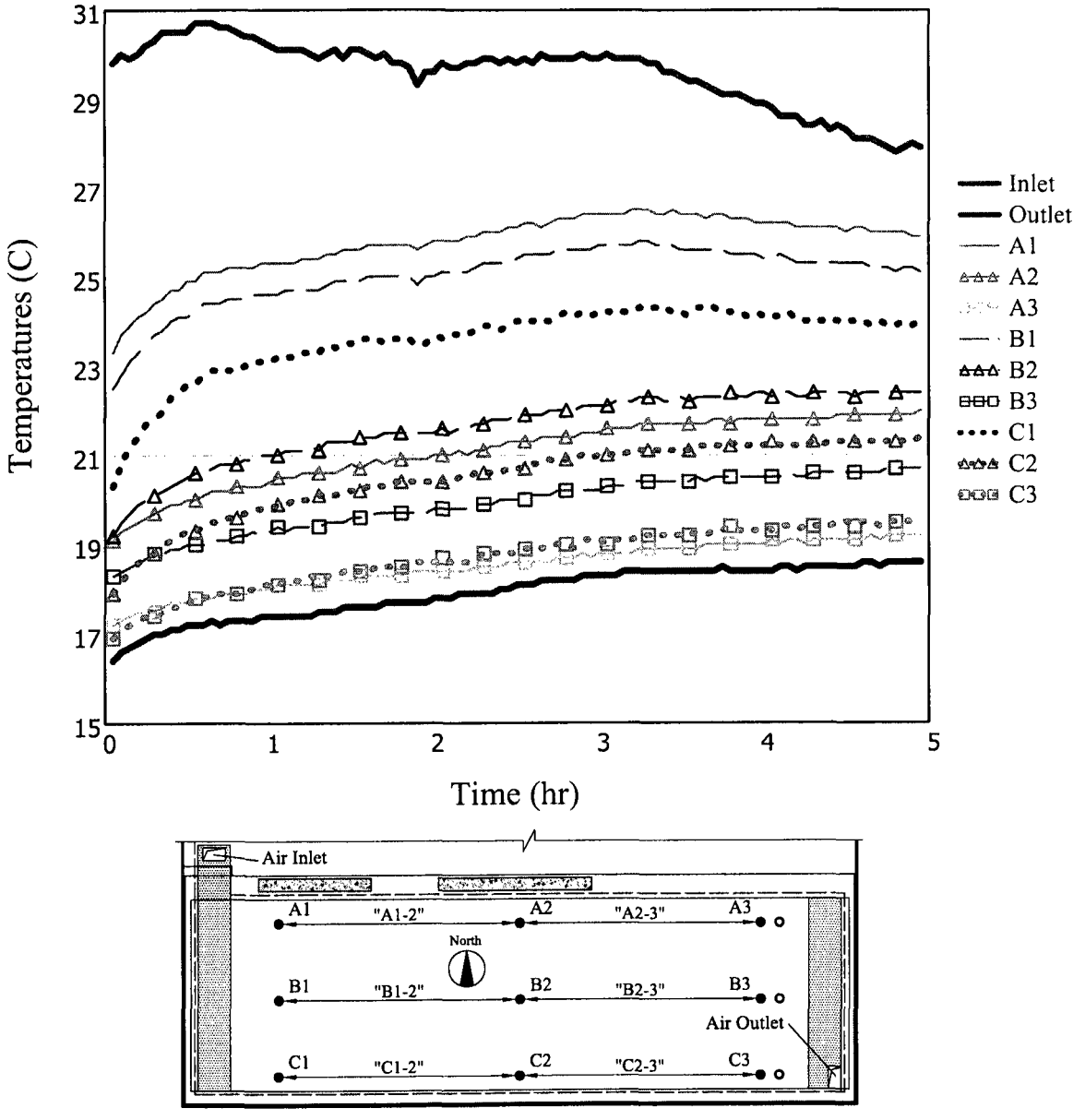

Figure 5.4: Air temperature profiles in VCS with no transmitted solar radiation (thin solid lines represent channel "A", dashed line for "B" and dotted line for "C"; triangular markers represent position "2" and square makers for "3")

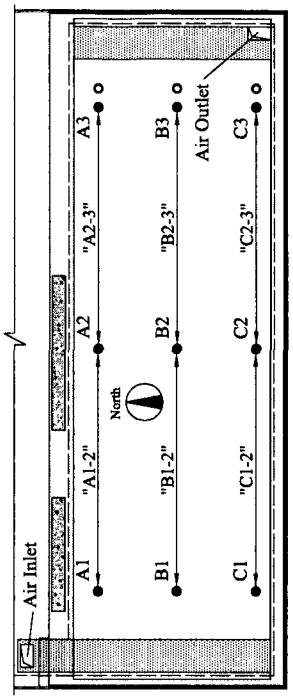

(a) Rotated floor plan

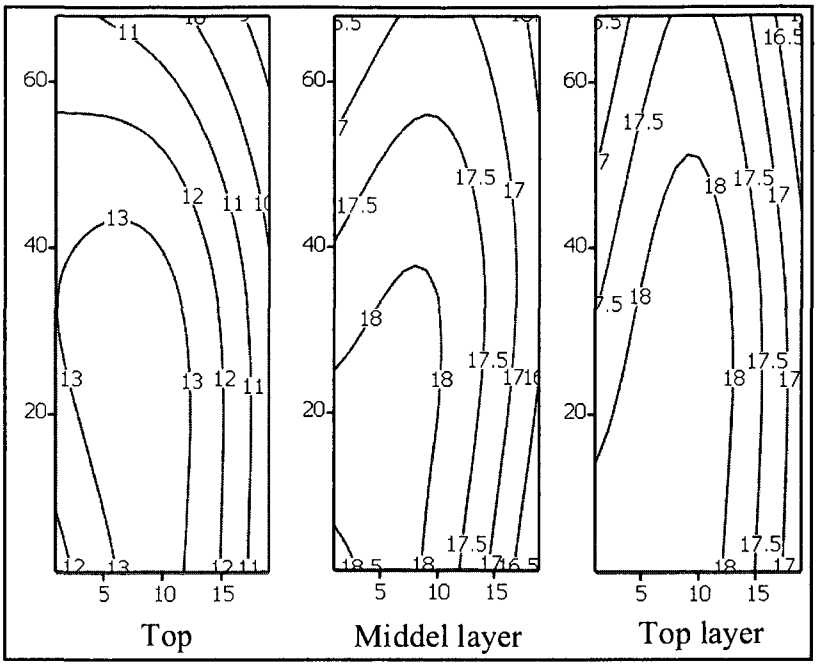

(b) In the beginning

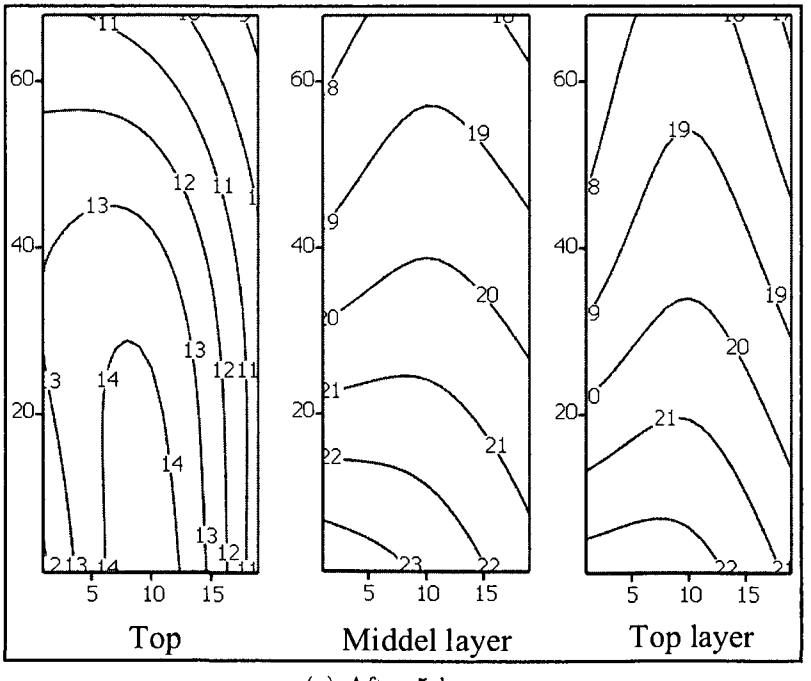

(c) After 5 hours

Figure 5.5: Measured and interpolated temperature distributions in VCS with no transmitted solar radiation (The plots are rotated 90 degrees counter-clockwise. Each unit of X or Y axis is the grid size (i.e. 150 mm))

has enough time to be redistributed inside the slab. Comparing Figure 5.4 and 5.5, the temperature difference between the air and the center layer of the slab, near the outlet is less than 1°C. This is also shown in another site test (Figure 5.9). This indicates that most of the heat is stored in the slab. Heat exchange effectiveness is high.

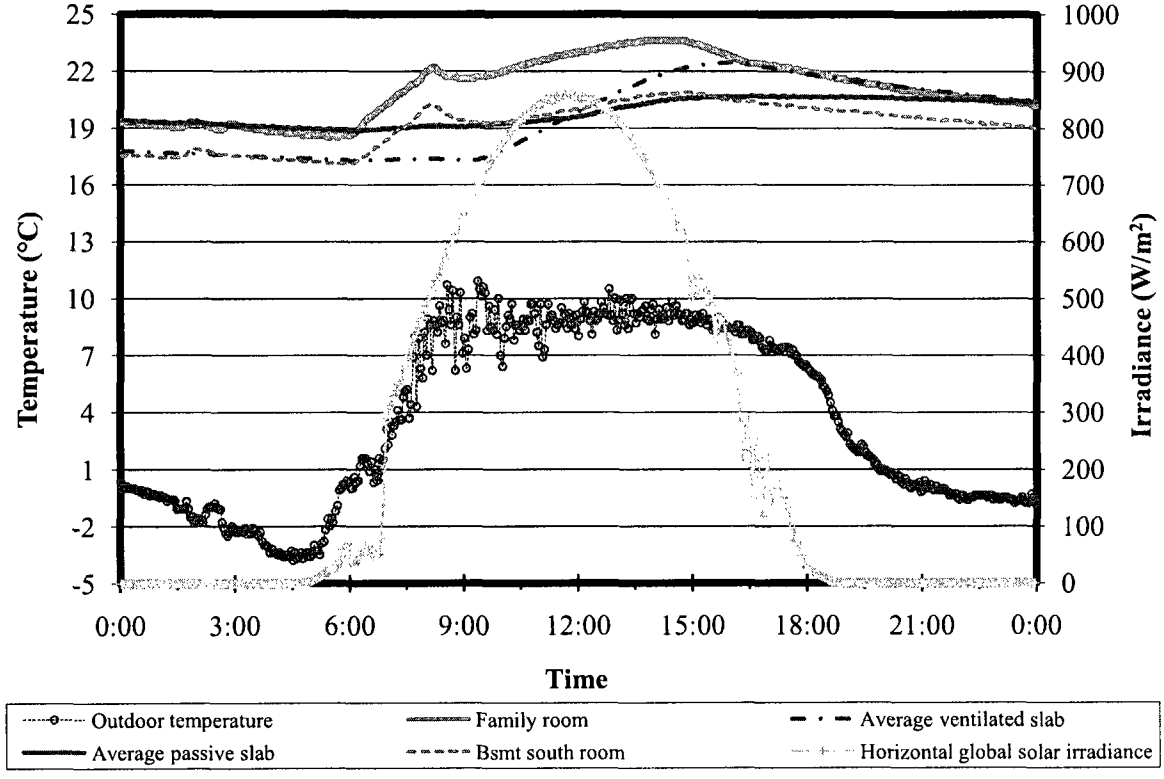

Figure 5.6: Temperature profiles on a day with active TES, April 15^{th}, 2008

Another site test was conducted on a mildly cold sunny day, April 15^{th}, 2008 without eliminating the effect of the solar gain (Figure 5.6). Figure 5.7(a) shows the temperature profiles and flow rate. The warm air from BIPV/T system 405 CFM (1.3 m/s in the air channels of the VCS) was drawn through the ventilated slab for about 7 hours. Comparing the average slab temperatures at the initial time and 7 hours later, about 14 kWh thermal energy was stored in the VCS, excluding the heat released from the slab to the living space during the storage process. The measured 24-hr heating load for April 15^{th} was about 30 kWh. The data from other two site tests

conducted on March 24^{th} and 25^{th} are shown in Section 3.4 on page 58.

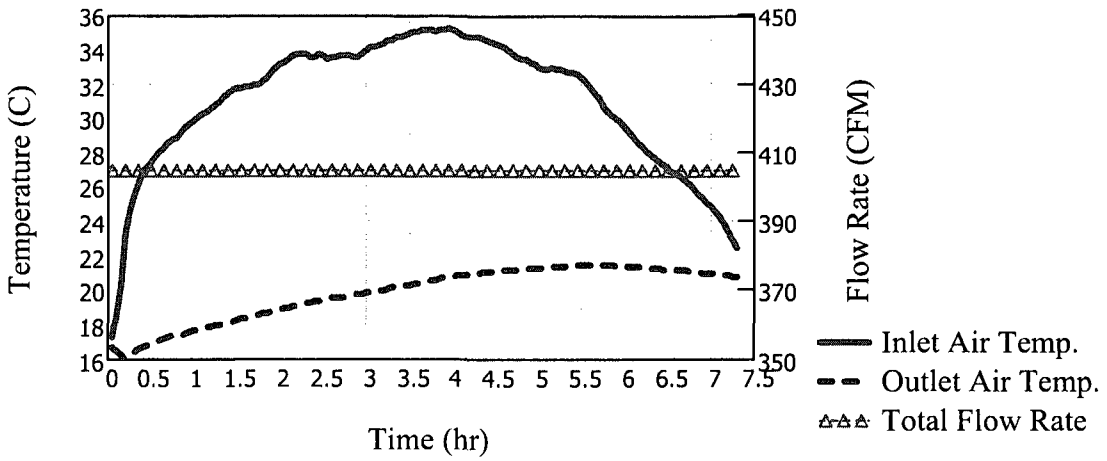

(a) Temperatures and flow rate profiles

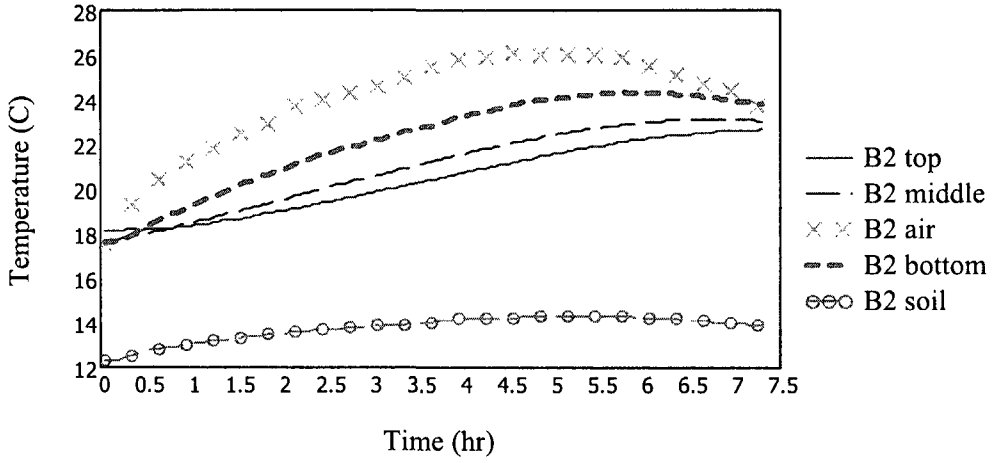

(b) Temperature profiles at "B2" (slab center)

Figure 5.7: Temperature profiles in VCS, April 15^{th}, 2008

From Figure 5.7(b), it can be seen that the maximum temperature difference between the bottom and the top surfaces was about 2°C. The temperature distributions on different layer of the slab can be found in Figure 5.14. Based on the data recorded from different site tests, the temperature gradients in all directions are not significant. This indicates that in control volume finite difference modeling, the discretization grid does not have to be very dense (Section 5.5).

5.4 Interior CHTC Calculation

Control volume (Figure 5.8) and log mean temperature difference (LMTD) [Kreith and Bohn, 2001] methods are used in the calculation of the CHTC $h_{c.vcs}$ between the steel deck surface and the air inside the air channels of the VCS. There are total six control volumes. Each control volume is defined by two adjacent temperature-measuring points (Figure 5.3). For example, from location A1 to A2 is control volume "A1-2". The length of each control volume is shown in Figure 5.3 on page 93. The measured temperatures of air, slab and soil at inlets and outlets, respectively, were input into Eq. 5.1 to calculate the $h_{c.vcs}$ of each control volume. The CHTC between the air and the bottom surface (metal mesh) is neglected considering its thermal conductance value is relatively small (about 10 $W/(m^2 \cdot K)$) compared to that of the rigid insulation (about0.5 $W/(m^2 \cdot K)$) under the metal mesh. The following equations were used:

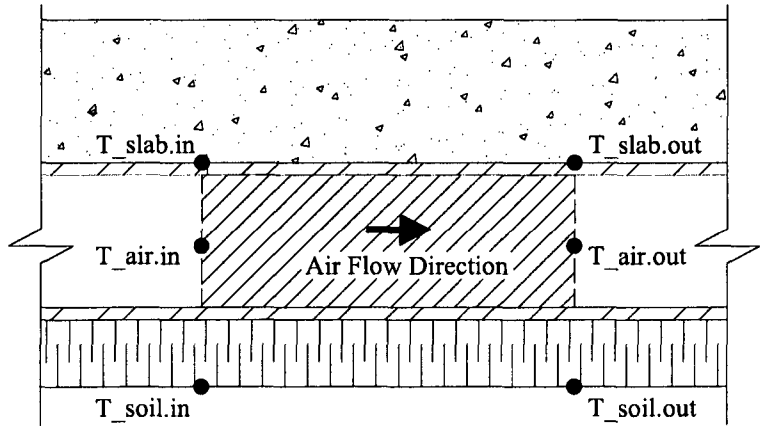

Figure 5.8: Schematic of control volume in VCS

Control volume energy balance equation

$$\Delta q_{air} = q_{air.to.slab} + q_{air.to.soil}$$

where

$$\Delta q_{air} = (T_{air.out} - T_{air.in}) \cdot (\dot{m}_{air} \cdot c_{p.air})$$

$$q_{air.to.slab} = h_{c.vcs} \cdot A_{chn} \cdot \Delta T_{LMTD.slab}$$

$$q_{air.to.soil} = u_{ins} \cdot A_{soil} \cdot \Delta T_{LMTD.soil}$$

$$\Delta T_{LMTD} = \frac{\Delta T_{out} - \Delta T_{in}}{\ln(\Delta T_{out}/\Delta T_{in})}$$

$\dot{m}_{air}$ is the mass flow rate of air.

A_{chn} is the area of steel deck surrounding the air (i.e. the boundary area except the metal mesh surface).

A_{soil} is the are of the bottom surface (i.e. the metal mesh).

ΔT_{in} is the temperature difference between the concrete/soil and the air at the inlet.

ΔT_{out} is the temperature difference between the concrete/soil and the air at the outlet.

$$h_{c.vcs} = \frac{\Delta q_{air} - q_{air.to.soil}}{\Delta T_{LMTD.slab} \cdot A_{chn}} \tag{5.1}$$

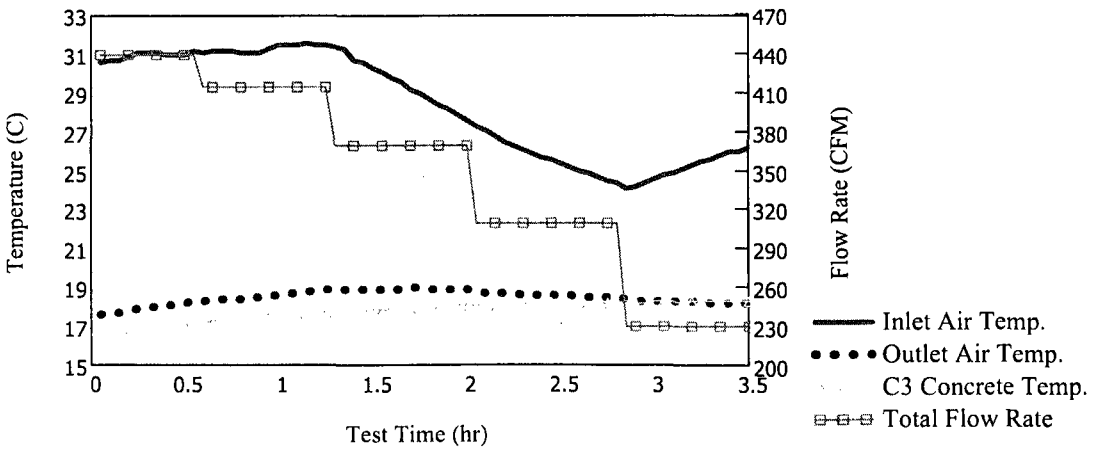

Figure 5.9: Test conditions for obtaining interior CHTC of VCS ("C3" is near outlet).

A site test was conducted on March 22^{nd} to obtain the data for the calculation of $h_{c.vcs}$. During the test, different air flow rates were used. The $h_{c.vcs}$ in the 6 control volumes were calculated. Figure 5.9 shows the test conditions and Figure 5.10 shows the calculation results used the recorded data from the site test. Except for control volumes "A1-2" and "A2-3", the calculated $h_{c.vcs}$ for each of the control volumes is similar to each other. As the flow rate decreased, the variations of $h_{c.vcs}$ between different channels became larger. This is possibly due to the fact that when there is smaller dynamic pressure in the air, less air is distributed to the channel "C" than that to channel "B". The main reason for differential values obtained in control volumes "A1-2" and "A2-3" (Figure 5.10) is that there are actually 20 air channels in the VCS; however, there is one channel above channel "A" sharing the air flow with channel "A". This means the air from one of the manifold outlets flows into two channels. Inputting higher than actual air mass flow rate in the calculation model caused the higher $h_{c.vcs}$ value than the actual value. The actual causes for these deviations mentioned above need further investigation.

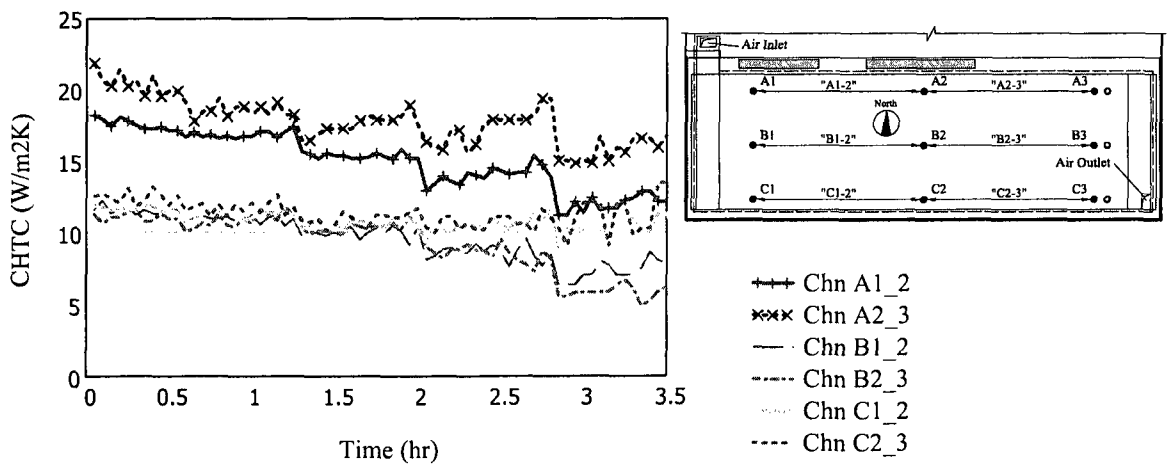

Figure 5.10: Calculated $h_{c.vcs}$ for each section

As it can be seen, the calculated $h_{c.vcs}$ for one control volume at one set flow rate (i.e. from hour 2 to hour 2.8) is increasing as time passes. The possible reason for this time-dependent increment is due to the change of the actual flow rate, which is

caused by the change of the thermal gravity effect discussed on page 79.

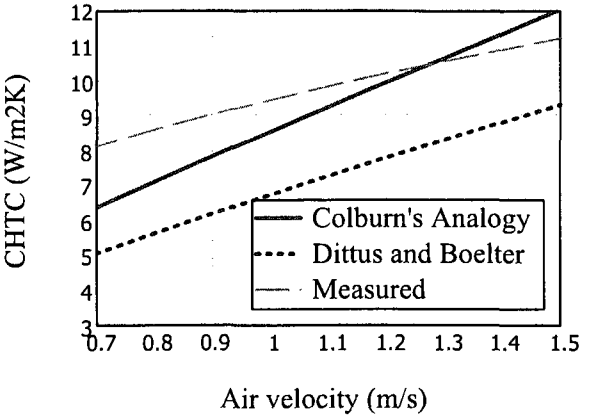

Figure 5.11: Calculated average $h_{c.vcs}$ vs. air speed

Figure 5.11 plots the experimental average $h_{c.vcs}$ against air velocity in the channel. The $h_{c.vcs}$ values plotted is the average of the $h_{c.vcs}$ values of the four control volumes "B1-2", "B2-3", "C1-2", and "C2-3". Reasonable values for $h_{c.vcs}$ are observed. In Figure 5.11, Colburn's analogy[4] [ASHRAE, 2005, Ch. 3] and Dittus-and-Boelter equation[5] [Rohsenow et al., 1998] are also plotted for comparison. Surface roughness of 0.8 mm was used to calculate the friction factor "f" in Colburn's analogy. The experimental $h_{c.vcs}$ can be approximated by a linear correlation Eq. 5.2, which is a function of the air velocity. The corresponding Reynolds numbers for 0.7 and 1.5 m/s air velocities inside the channel are about 3850 and 8250 respectively. For future studies, the air velocity inside the air channel has to be precisely measured to obtain a more accurate $h_{c.vcs}$.

$$h_{c.vcs} = 3.94 \cdot v_{air} + 5.45 \tag{5.2}$$

where

v_{air} is the air velocity in the channel (m/s).

[4] $Nu = {}^{f}/_{8}\mathrm{Re} \cdot \mathrm{Pr}^{1/3}$

[5] $Nu = 0.026\,\mathrm{Re}^{0.8} \cdot \mathrm{Pr}^{1/3}$ $(T_s < T_{fluid},\ 2500 < Re < 124000,\ L/d > 60)$

5.5 Modeling and Simulation

Three-dimensional control volume finite difference numerical analysis is employed in the modeling of the VCS. The existence of the metal deck is neglected. The physical properties of concrete are taken as follows: specific heat is 900 $J/(kg \cdot K)$; density is 2300 kg/m^3; conductivity is 1.9 $W/(m \cdot K)$. The study of the thermophysical properties of concrete is presented in Section C.1. Small variations of the physical properties do not affect the slab's thermal behavior to a significant extent [Bilgen and Richard, 2002; Chen et al., 2008]. Eq. 5.3 is the explicit finite difference equation for the concrete nodes. The last term of Eq. 5.3 is the combined convective and radiative heat transfer for exterior nodes of the VCS. For internal nodes, the last term equals to zero. For the air control volume inside the channel, upwind scheme method [Patankar, 1980] is applied, as shown in Eq. 5.4. The length of each air control volume equals to that of the concrete node in stream-wise direction.

$$\frac{(T^{t+\Delta t}_{x,y,z} - T^{t}_{x,y,z}) \cdot C_{x,y,z}}{\Delta t} = \sum_{i} (\Delta T^{i}_{x,y,z} \cdot U^{i}_{x,y,z}) + (T^{c.r}_{x,y,z} - T^{t}_{x,y,z}) \cdot A_{x,y,z} \cdot h^{c.r}_{x,y,z} \quad (5.3)$$

where

$\Delta T^{i}_{x,y,z}$ is the temperature difference between current node at x, y, z and the adjacent node in direction i.

$U^{i}_{x,y,z}$ is the conductance (W/K) between current node at x, y, z and the adjacent node in direction i.

$T^{c.r}_{x,y,z}$ is the effective temperature for combined convective and radiative heat transfer (e.g. solar-air temperature).

$h^{c.r}_{x,y,z}$ is the combined convective and radiative heat transfer coefficient.

$$T_{air}^{p} = \frac{\dot{m}c_{p.air} \cdot T_{air}^{p-1} + \sum_{i} (T_{surface}^{i} \cdot U_{c}^{i})}{\dot{m}c_{p.air} + \sum_{i} U_{c}^{i}} \tag{5.4}$$

where

T_{air}^{p-1} is the temperature of the air at previous control volume.

U_c^i is the conductance (W/K) between current air node and the surface in contact at location i.

The control volume numerical model of the VCS evolved from the standard regular 3D discretization with a large number of control volumes to the simplified discretization. Based on the simulations used the regular discretization and the monitored data from site tests, a simplified discretization scheme: a 9-layer model is developed. The 9-layer model is viable for the study on the specific type of VCS considered in this study. Using the simplified model, the computational effort required for simulation is greatly reduced; meanwhile, the accuracy is retained on acceptable level.

5.5.1 Regular 3D discretization

At the design stage of the VCS, in order to facilitate the modeling, the cross section of the slab channel was transformed as shown in Figure 5.12(a), and a regular-grid discretization scheme was employed. A regular discretization and simulations were performed for the half section of the channel [Chen et al., 2007] (Figure 5.12(b) and 5.12(c)). The distance between nodes is 15 mm in X and Y directions and 60 mm in the Z direction. The radiative heat exchange between the surrounding surfaces of the air channel (e.g. between concrete nodes or between concrete node and the upper surface of the bottom insulation) is neglected. Figure 5.12(c) shows a contour plot of the typical temperature distribution on the cross section of the simulated half channel.

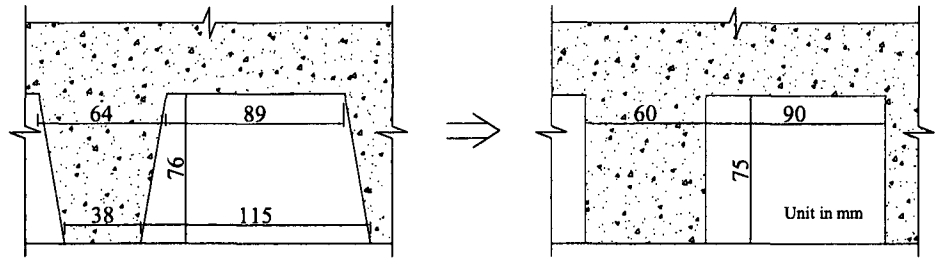

(a) Transformation of the cross section

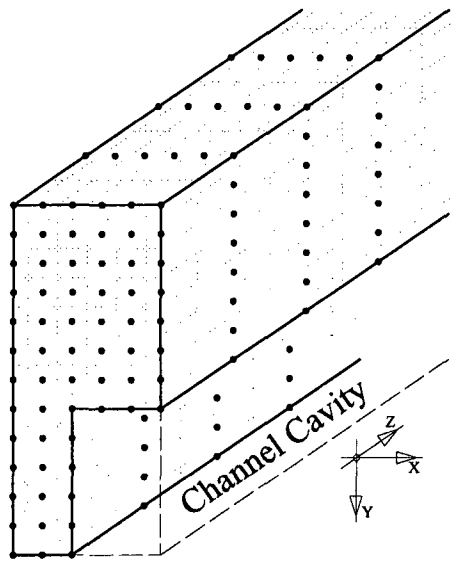

(b) 3D discretization of the transformed slab

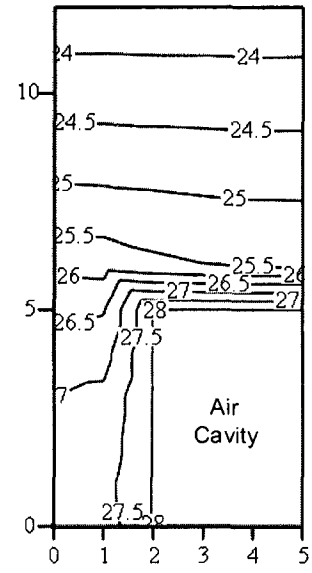

(c) Simulated cross section temperature distribution

Figure 5.12: Regular 3D discretization and simulation (in figure (c), unit of X or Y axis is the grid size (i.e. 15 mm)).

5.5.2 9-layer 3D discretization

The modeling using a regular 3D discretization scheme requires large computational effort. Performing transient simulations for the whole slab over a long period (e.g. for several days) is not practical. Based on the pattern of the temperature distribution on the cross section, the discretization was modified (Figure 5.13).

The thickness of the control volume is 2.4 *mm* for the top node "Y-1". The corresponding Biot number[6] is 0.015. This Biot number is calculated by assuming the

[6]The ratio of the internal thermal resistance of a solid to the boundary layer thermal resistance. When Biot is less than 0.1, the temperature gradient inside the grid is small, and the error in-

surface combined heat transfer coefficient "$h_{c.r}$" is 10 $W/(m^2 \cdot K)$ and there is no solar gain. If solar gain is present, the Biot number will increase. For the bottom node "Y-9", the thickness is 2.7 mm. It is 1/16 of the bottom width of the flute. By using "$h_{c.r}$" is 15 $W/(m^2 \cdot K)$, the calculated Biot number is about 0.02. Denser grids for the top layer and the bottom layer enhance the accuracy of the simulation of the heat transfer at the boundaries. From exterior layer to interior layer, the thickness of the layer increases with a factor of two. The thickness of the top and bottom grids and the increasing factor result in the 9-layer discretization scheme. The allowable maximum time step for explicit solution is about 12 seconds for satisfying $Fo < 0.5$ [Kreith and Bohn, 2001][7]. A 10-second time step was used in the simulation. Eq. 5.2 was used for the calculation of the $h_{c.vcs}$.

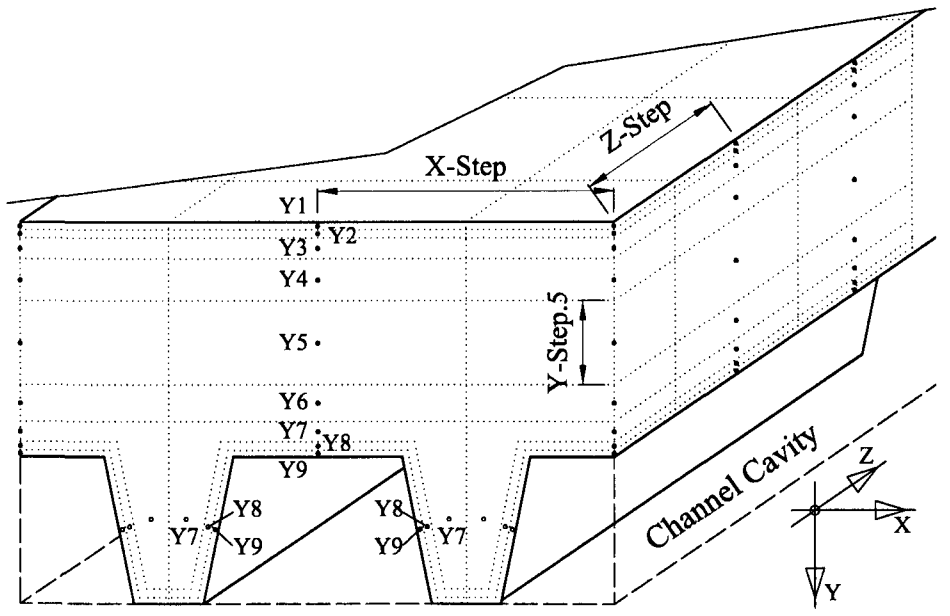

Figure 5.13: Schematic of the 9-layer 3D discretization of VCS

In the simulation, the calculation of effective conductance between nodes with irregular shapes uses the area-weighted distances: the X-direction distances between

troduced by the assumption that the temperature at any instant is uniform will be less than 5% [Kreith and Bohn, 2001].

[7]Fourier number. It is the ratio of the heat conduction rate to the rate of thermal energy storage in a solid.

adjacent "Y-7" nodes and between "Y-7" and "Y-8" nodes; the Y-direction distances between "Y-6" and "Y-7" nodes and between "Y-7" and "Y-8" nodes. It is assumed that for the radiative heat transfer inside the air channels, the concrete nodes only exchange heat with the upper surfaces of the bottom insulation within the same air control volume. The value of angle factor F_a equals to one. This assumption is based on two factors: First, the length of the air control volume stream-wise is 150 mm in this discretization scheme. This is two times the height of the control volume (i.e. the height of the air channel). Second, the temperature difference between two adjacent concrete nodes or two adjacent insulation nodes is negligibly small.

One simulation was performed using the measured boundary conditions (i.e. the room air, the ground soil temperatures, the air flow temperature, and the flow rate) as inputs. Figure 5.14 shows the measured and interpolated surface temperature distributions and the simulated values side by side. The measured data is from the April 15^{th} test. The thermal performance of the VCS of that day was described in Section 5.3 on page 99. The plots in Figure 5.14 show the temperature distributions (both measured and simulated) on different layers 4 hours after the field operation started. The top end and the bottom end of the plots of the simulated data show the effect of the manifold. It can be seen that the simulation matches well with the measured data. The discrepancy is mainly due to the following factors:

- The actual boundary conditions of the VCS are complex. The soil temperatures were only measured at 9 locations. The soil temperature is lower near the edge of the foundation as shown in Figure 5.14. The north side of the VCS is directly in contact with the concrete footing and the concrete wall. There was also transmitted solar irradiance absorbed by the VCS. These factors cannot be completely represented in the simulation.

- The exact amount of the concrete mass is unknown. The slab was designed to

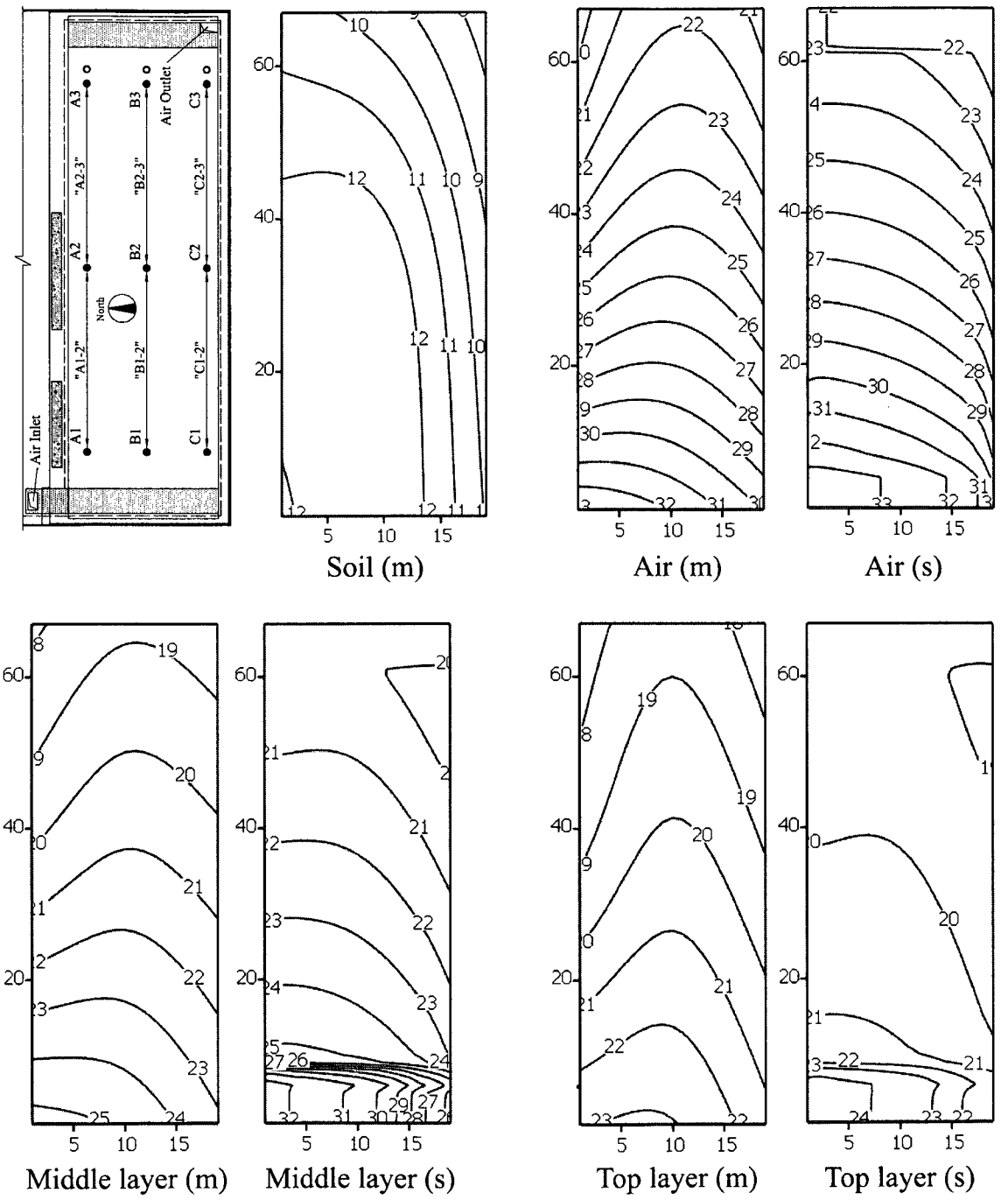

Figure 5.14: Measured and simulated (9-layer model) temperature distributions of VCS ("m": measured and interpolated; "s": simulated. The plots are rotated 90 degrees counterclockwise. Each unit of X or Y axis is the grid size (i.e. 150 mm)).

be 4 inches thick; however, some parts of the slab are measured about 5 inches thick.

- The heat transfer rate in the inlet and outlet manifolds cannot be simulated precisely due to the lack of instrumentation.
- The affects of the transmitted solar radiation absorbed by the slab.
- The $h_{c.vcs}$ in the channel "A" and its close channel are uncertain. This was shown in the calculation of the $h_{c.vcs}$ in Section 5.4.
- The errors induced by the temperature measurement. The type of thermocouple used has an accuracy of $\pm 0.5\,^{\circ}C$.

5.6 Conclusions

This chapter presents an in-depth study of the VCS in ÉcoTerra. The VCS serves as an active TES to store the thermal energy collected by the roof-mounted BIPV/T system. The study presented includes the assessment of the thermal performance based on field measurements, the calculation of CHTC inside the air channel, the characteristics of the temperature distributions in the VCS, and the modeling of the VCS. The construction of the VCS is based on mature construction technologies. It is practical, reliable, and simple.

The data from field measurements indicate that the VCS efficiently stores the heat collected by the BIPV/T system. The thermal energy from the warm air passing through its hollow cores is recovered by the VCS to the most extent without considerable pressure drop. Its thermal coupling with the BIPV/T system significantly increases the overall efficiency of the VCS-BIPV/T system. The amount of the useful thermal energy is increased. A simplified three-dimensional explicit finite difference

thermal model is created to simulate the thermal performance of the VCS. The model was shown to be appropriate for design purposes and to study control strategies.

The following topics are suggested for future studies:

- The study of the sizing methodology for thermal mass and using alternative types of precast slabs or walls, for example double-Tee slab, as active TES.
- The effects of placing the VCS between two living spaces. In such way, all stored thermal energy would be useful for space heating/condition.
- The study of the combined usages of auxiliary forced-air radiant floor heating, active solar TES and passive solar heating. If the VCS is possibly exposed to a large amount of direct solar radiation, the combined heating effect of the warm air and the absorbed solar radiation need to be carefully studied to avoid overheating of the living space and floor surface [Athienitis and Chen, 1993; Athienitis, 1997; Athienitis and Chen, 2000].
- The further simplification of the discretization of the slab can reduce the computational effort. The compromise of accuracy in both temperature and thermal energy storage needs to be quantified.

Chapter 6

Conclusions

This thesis presents an interdisciplinary research of an integrated solar/structural system: an innovative VCS coupled with a BIPV/T system (VCS-BIPV/T) in a prefabricated energy efficient solar home - ÉcoTerra. Based on measurements, the study quantifies the capabilities and effectiveness of the VCS and the BIPV/T roof, and their significant contribution to the reduction of the space heating energy consumption of the solar home. The design concepts, models for thermal simulations and construction details of the VCS-BIPV/T system and the house are also presented.

The full-scale monitoring indicate that the BIPV/T roof is able to lower the PV panels' operation temperature and collect a considerable amount of solar thermal energy at the same time. The typical temperature rise of the air on a sunny winter day is about 30 to 35 °C at 500 CFM flow rate. The typical thermal efficiency is larger than 20% (the ratio of the heat extracted by the air to the solar irradiance absorbed by the roof). Comparing the energy (electricity and thermal energy) output and the construction cost of the BIPV/T system with that of the BIPV system, the former has considerably higher cost-effectiveness. A simple one-dimensional, control volume finite difference, steady state model is created to simulate the thermal performance

of the BIPV/T system. The model is validated using full-scale monitoring data.

The mechanically ventilated concrete slab (VCS) uses the basement slab as active thermal mass to efficiently store the thermal energy collected by the BIPV/T roof and release the heat through its top surface to the living space. The heated air from the BIPV/T roof goes directly into the VCS. The reverse-return layout enables the even distribution of air inside the air channels. The mechanical ventilation increases the CHTC between the air and the concrete. The air channels inside the VCS provide additional and larger heat transfer area compared to normal solid concrete slab. Higher CHTC and larger heat transfer area enables the VCS to efficiently recover the heat from the warm air passing through. Field monitoring show that 35 °C inlet air at 400 CFM flow rate left the VCS at 20 °C, which is the temperature of the concrete near the outlet. This suggests that the heat transfer effectiveness reached the maximum value. A simplified three-dimensional, explicit finite difference, transient thermal model is created to simulate the thermal performance of the VCS. The model is validated using full-scale monitoring data and proved to be efficient and adequate for design purposes and to study control strategies.

The constructions of the VCS and the BIPV/T roof are based on mature construction technologies. They are practical, reliable, and simple. More attention should be paid to the thermal insulation and the air-tightness of the ducting. Site tests show that there is a considerable heat loss from the heated air between the outlet of the BIPV/T roof and the inlet of the VCS - about 8 °C decrease for 40 °C outlet air at 400 CFM flow rate. The heat loss is due to conduction and air leakages. Some of the lost heat goes into the living space through the ducts. That is useful for space heating but not controlled. The typical COP of the VCS-BIPV/T system for heating DHW and VCS together is about 8 to 9. This number could be higher if the heat loss is reduced.

ÉcoTerra adopts an integrated space and domestic hot water heating system, which

combines the solar systems (VCS-BIPV/T, passive solar space heating) and the ground source heat pump. The heating system is operated by a home automation system to optimize this integrated system's overall performance. The advantage of using the VCS to store the thermal energy collected by the BIPV/T system is that the necessary supply air temperature for heating the VCS can be just 3 to 10 °C higher than the temperature of the slab. Normally the floor temperature is close to the room temperature. That means this is a relatively low temperature heating application. High PV temperatures are not required for heating air. A large amount of air at relatively low, but useful temperature can be utilized. The typical 24-hour heating energy consumption of the house on a cold (average outdoor temperature of -10 °C) sunny winter day is about 60 kWh. This is under the condition of no internal heat gain (e.g. occupancy, appliance). The house is expected to have an annual energy consumption approaching net-zero (less than 4000 kWh, 10% of that for a normal house of similar size).

Since the very beginning of the conceptual design of ÉcoTerra, and through the whole construction and commissioning process, architects, engineers, researchers, manufacturers, home builders, government officials, and other professional personnel have worked together interactively. The close collaboration between the parties has been critical in helping each other understand the new and advanced building technologies and apply them appropriately. Their collective work finally brings the ÉcoTerra into reality successfully.

Major modern buildings adopt concrete structures. The building itself is a large evenly distributed thermal mass; neither extra material nor structural weight is added. Ways of utilizing building structures as thermal mass are available, feasible, and already in practice. Utilizing building structure as thermal mass is environmentally and economically beneficial. Objectives of current research are to determine

approaches that are more energy efficient and effective, and can integrated structural mass with other sustainable energy systems to have an overall better performance. The integrated VCS-BIPV/T system presents a feasible and efficient approach. The study presented in this thesis sets up a valuable and informative reference for future studies. The suggested future improvement and studies are included at the end of each respective chapter.

Bibliography

ACI Committee 122 [2002]. 122R-02: Guide to thermal properties of concrete and masonry systems, *in* ACI (ed.), *Manual of Concrete Practice*, Vol. 2008, American Concrete Institute, Farmington Hills, MI, USA.

ASHRAE [2004]. *Standard 55: Thermal Environmental Conditions for Human Occupancy*, ASHRAE Standards, American Society of Heating, Refrigerating and Air-Conditioning Engineers, Atlanta, GA, USA.

ASHRAE [2005]. *Fundamentals*, ASHRAE Handbooks, SI edn, American Society of Heating, Refrigerating and Air-Conditioning Engineers, Atlanta, GA, USA.

Athienitis, A. K. [1997]. Investigation of thermal performance of a passive solar building with floor radiant heating, *Solar Energy* **61**(5): 337 – 345.

Athienitis, A. K. and Chen, T. Y. [1993]. Experimental and theoretical investigation of floor heating with thermal storage, *ASHRAE Transactions* **99**(1): 1049 – 1057.

Athienitis, A. K. and Chen, Y. [2000]. Effect of solar radiation on dynamic thermal performance of floor heating systems, *Solar Energy* **69**(3): 229 – 237.

Athienitis, A. K. and Santamouris, M. [2002]. *Thermal Analysis and Design of Passive Solar Buildings*, James & James Science Publishers, London, UK.

Balcomb, J. D. [1983]. *Heat storage and distribution inside passive buildings*, Los Alamos National Laboratory, Los Alamos, NM, USA.

Balcomb, J. D. (ed.) [1992]. *Passive solar buildings*, Solar Heat Technologies: Fundamentals and Applications, MIT Press, Cambridge, MA, US.

Bankston, C. A. (ed.) [1990-1997]. *Solar Heat Technologies: Fundamentals and Applications*, MIT Press, Cambridge, MA, US.

Barton, P., Beggs, C. B. and Sleigh, P. A. [2002]. A theoretical study of the thermal performance of the termodeck hollow core slab system, *Applied Thermal Engineering* **22**(13): 1485–1499.

Bazilian, M. D., Kamalanathan, H. and Prasad, D. K. [2002]. Thermographic analysis of a building integrated photovoltaic system, *Renewable Energy* **26**(3): 449–461.

Bazilian, M. D., Leenders, F., Van Der Ree, B. G. C. and Prasad, D. [2001]. Photovoltaic cogeneration in the built environment, *Solar Energy* **71**(1): 57–69.

Bazilian, M. D. and Prasad, D. [2002]. Modeling of a photovoltaic heat recovery system and its role in a design decision support tool for building professionals, *Renewable Energy* **27**(1): 57–68.

Bilgen, E. and Richard, M.-A. [2002]. Horizontal concrete slabs as passive solar collectors, *Solar Energy* **72**(5): 405 – 413.

Braham, G. D. [2000]. Comparative performance of U.K. fabric energy storage systems, *ASHRAE Transactions* **106**: 811 – 818.

Braun, J. E. [2003]. Load control using building thermal mass, *Journal of Solar Energy Engineering* **125**(3): 292–301.

CCMC [2006]. CCMC evaluation report: Walltite, *Technical Report CCMC 12840-R*, National Research Council Canada.

CCMC [2007]. CCMC evaluation report: Enertite, *Technical Report CCMC 13055-R*, National Research Council Canada.

Charron, R. and Athienitis, A. K. [2006a]. Optimization of the performance of double-facades with integrated photovoltaic panels and motorized blinds, *Solar Energy* **80**(5): 482 – 91.

Charron, R. and Athienitis, A. K. [2006b]. A two-dimensional model of a double-facade with integrated photovoltaic panels, *Journal of Solar Energy Engineering* **128**(2): 160–167.

Chen, Y., Athienitis, A. K. and Galal, K. E. [2007]. Design and simulation of a building integrated photovoltaic-thermal system and thermal storage for a solar house, *Proceedings of 32rd Solar Energy Society of Canada Inc. (SESCI) Conference & 2nd Conference of the Solar Buildings Research Network (SBRN)*, Calgary, Canada.

Chen, Y., Athienitis, A. K., Park, K. and Galal, K. E. [2008]. Design, thermal performance & modelling of a ventilated concrete slab coupled with BIPV/T system, *Proceedings of 33rd Solar Energy Society of Canada Inc. (SESCI) Conference & 3rd Conference of the Solar Buildings Research Network (SBRN)*, Fredericton, Canada.

CMHC [1998]. *Tap the Sun*, Canada Mortgage and Housing Corporation, Canada.

Davies, M. G. [2004]. *Building Heat Transfer*, 1 edn, Wiley, West Sussex, England.

Duffie, J. A. and Beckman, W. A. [2006]. *Solar Engineering of Thermal Processes*, 3 edn, Wiley, Hoboken, NJ, US.

Eicker, U. [2003]. *Solar Technologies for Buildings*, Wiley, Chichester, NJ, US.

Filleux, C. and Elste, P. [2000]. Closed collection loop with radiant discharge storage, *in* S. R. Hastings and O. Mørck (eds), *Solar Air Systems - A Design Handbook*, James & James Ltd., London, UK, chapter II.4.

Fort, K. [2000]. Hypocaust and murocaust storage, *in* S. R. Hastings and O. Mørck (eds), *Solar Air Systems - A Design Handbook*, James & James Ltd., London, UK, chapter IV.6.

Franta, G. [1990]. Thermal energy distribution in building interiors, *in* B. Anderson (ed.), *Solar Building Architecture*, MIT Press, Cambridge, MA, US, chapter 5.

Hastings, S. R. and Mørck, O. (eds) [2000]. *Solar Air Systems - A Design Handbook*, James & James Ltd., London, UK.

Howard, B. D. and Fraker, H. [1990]. Thermal energy storage in building interiors, *in* B. Anderson (ed.), *Solar Building Architecture*, MIT Press, Cambridge, MA, US, chapter 4.

Hutcheon, N. B. and Handegord, G. O. P. [1983]. *Building science for a cold climate*, Wiley, Toronto, Canada.

Krauter, S., Araujo, R. G., Schroer, S., Hanitsch, R., Salhi, M. J., Triebel, C. and Lemoine, R. [1999]. Combined photovoltaic and solar thermal systems for facade integration and building insulation, *Solar Energy* **67**(4): 239 – 248.

Kreith, F. and Bohn, M. S. [2001]. *Principles of Heat Transfer*, 6 edn, Brooks/Cole Pub., Australia.

Liao, L., Athienitis, A. K., Candanedo, L., Park, K.-W., Poissant, Y. and Collins, M. [2007]. Numerical and experimental study of heat transfer in a bipv-thermal system, *Journal of Solar Energy Engineering* **129**(4): 423–430.

NRCan [2003]. HOT2000, software. Natural Resources Canada, `www.sbc.nrcan.gc.ca/software_and_tools/software_and_tools_e.asp`.

NRCan [2006]. RETScreen, software. Natural Resources Canada, `www.retscreen.net/ang/home.php`.

Palyvos, J. A. [2008]. A survey of wind convection coefficient correlations for building envelope energy systems' modeling, *Applied Thermal Engineering* **28**(8-9): 801 – 808.

Pantic, S. [2007]. *Energy analysis of photovoltaic thermal system integrated with roof and hvac system*, Master's thesis, Concordia University, Montreal, QC, Canada.

Patankar, S. V. [1980]. *Numerical heat transfer and fluid flow*, Hemisphere Pub. Corp., New York, USA.

Persaud, R. and Symons, D. [2006]. Design and testing of a composite timber and concrete floor system, *Structural Engineer* **84**(4): 22 – 30.

PTC [2007]. Mathcad, software. Parametric Technology Corporation, `www.ptc.com/appserver/mkt/products/home.jsp?k=3901`.

Ren, M. J. and Wright, J. A. [1998]. Ventilated slab thermal storage system model, *Building and Environment* **33**(1): 43–52.

Rohsenow, W. M., Hartnett, J. P. and Cho, Y. I. (eds) [1998]. *Handbook of Heat Transfer*, 3rd edn, McGraw-Hill, New York, NY.

Rossi, G. and Scudo, G. [2000]. Open collection loop with radiant discharge storage, *in* S. R. Hastings and O. Mørck (eds), *Solar Air Systems - A Design Handbook*, James & James Ltd., London, UK, chapter II.2.

Saini, R. P. and Saini, J. S. [1997]. Heat transfer and friction factor correlations for artificially roughened ducts with expanded metal mesh as roughness element, *International Journal of Heat and Mass Transfer* **40**(4): 973–986.

Saini, R. P. and Verma, J. [2008]. Heat transfer and friction factor correlations for a duct having dimple-shape artificial roughness for solar air heaters, *Energy* **33**(8): 1277–1287.

Sharples, S. and Charlesworth, P. S. [1998]. Full-scale measurements of wind-induced convective heat transfer from a roof-mounted flat plate solar collector, *Solar Energy* **62**(2): 69 – 77.

Shaw, M. R., Treadaway, K. W. and Willis, S. T. P. [1994]. Effective use of building mass, *Renewable Energy* **5**(part II): 1028 – 1038.

Standeven, M., Cohen, R., Bordass, B. and Leaman, A. [1998]. Probe 14: Elizabeth fry building, *Building Services Journal* pp. 37–42.

Webb, R. L. [1987]. Enhancement of single-phase heat transfer, *in* S. Kakaç, R. K. Shah and W. Aung (eds), *Handbook of Single-Phase Convective Heat Transfer*, John Wiley & Sons, New York, NY, USA, chapter 17.

Winwood, R., Benstead, R. and Edwards, R. [1997a]. Advanced fabric energy storage i: review, *Building Services Engineering Research & Technology* **18**(1): 1 – 6.

Winwood, R., Benstead, R. and Edwards, R. [1997b]. Advanced fabric energy storage ii: computational fluid dynamics modelling, *Building Services Engineering Research & Technology* **18**(1): 7 – 16.

Winwood, R., Benstead, R. and Edwards, R. [1997c]. Advanced fabric energy storage iii: theoretical analysis and whole-building simulation, *Building Services Engineering Research & Technology* **18**(1): 17 – 24.

Winwood, R., Benstead, R. and Edwards, R. [1997d]. Advanced fabric energy storage iv: experimental monitoring, *Building Services Engineering Research & Technology* **18**(1): 25 – 30.

Zhang, Y., Lin, K., Zhang, Q. and Di, H. [2006]. Ideal thermophysical properties for free-cooling (or heating) buildings with constant thermal physical property material, *Energy and Buildings* **38**(10): 1164 – 1170.

Appendices

Appendix A Additional Information on ÉcoTerra

A.1 Construction Drawings of ÉcoTerra

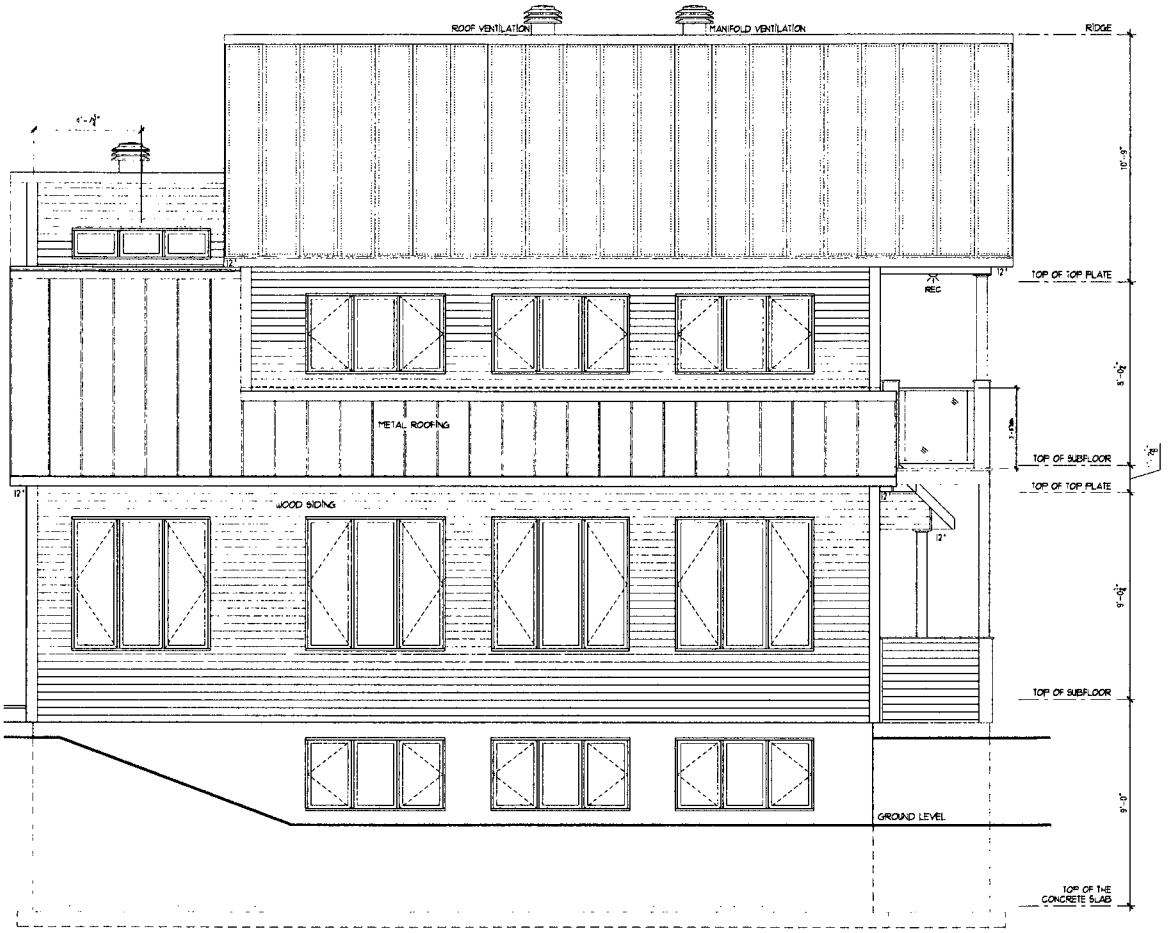

Figure A.1: South elevation (courtesy of Alouette Homes)

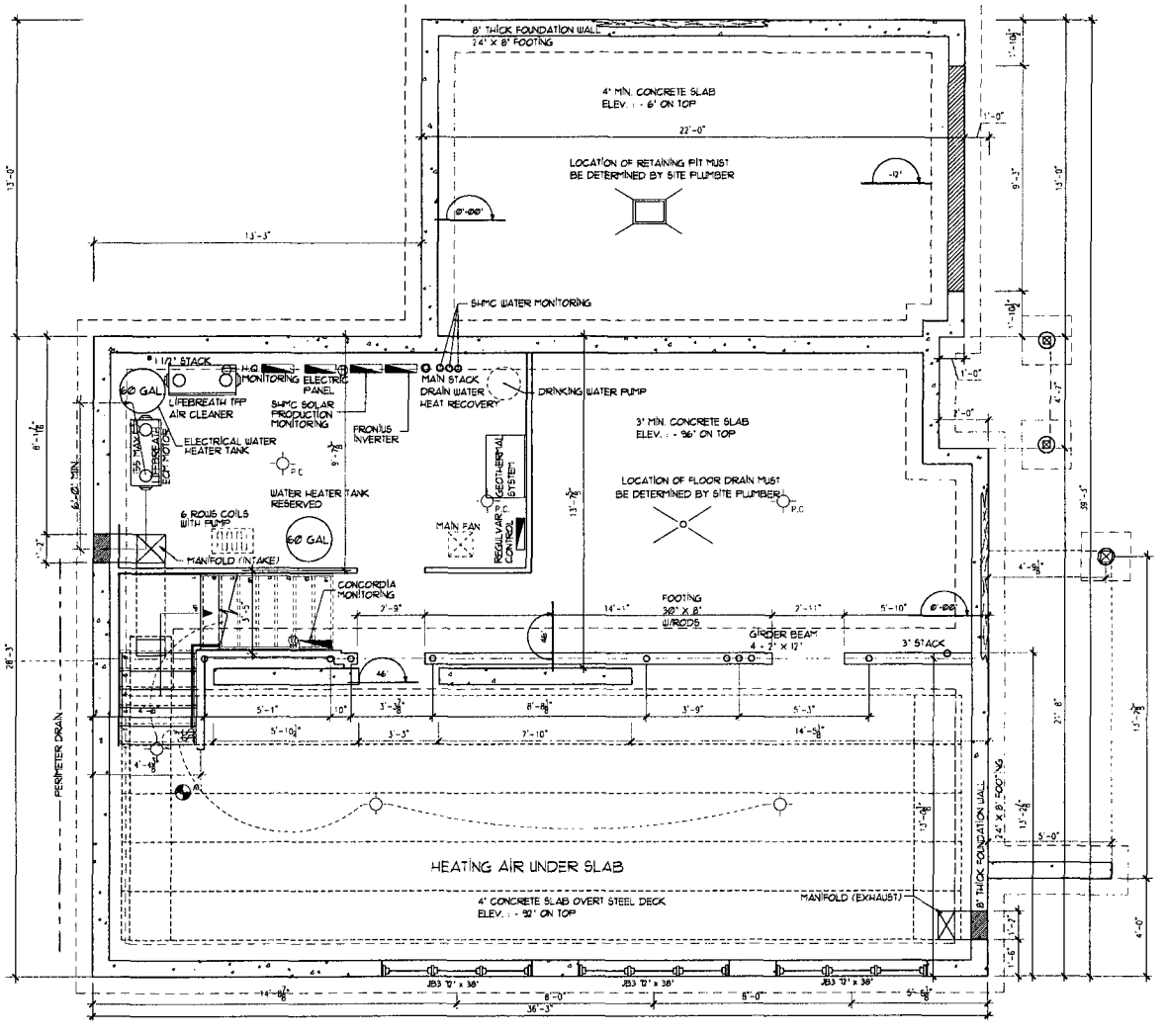

Figure A.2: Basement plan (courtesy of Alouette Homes)

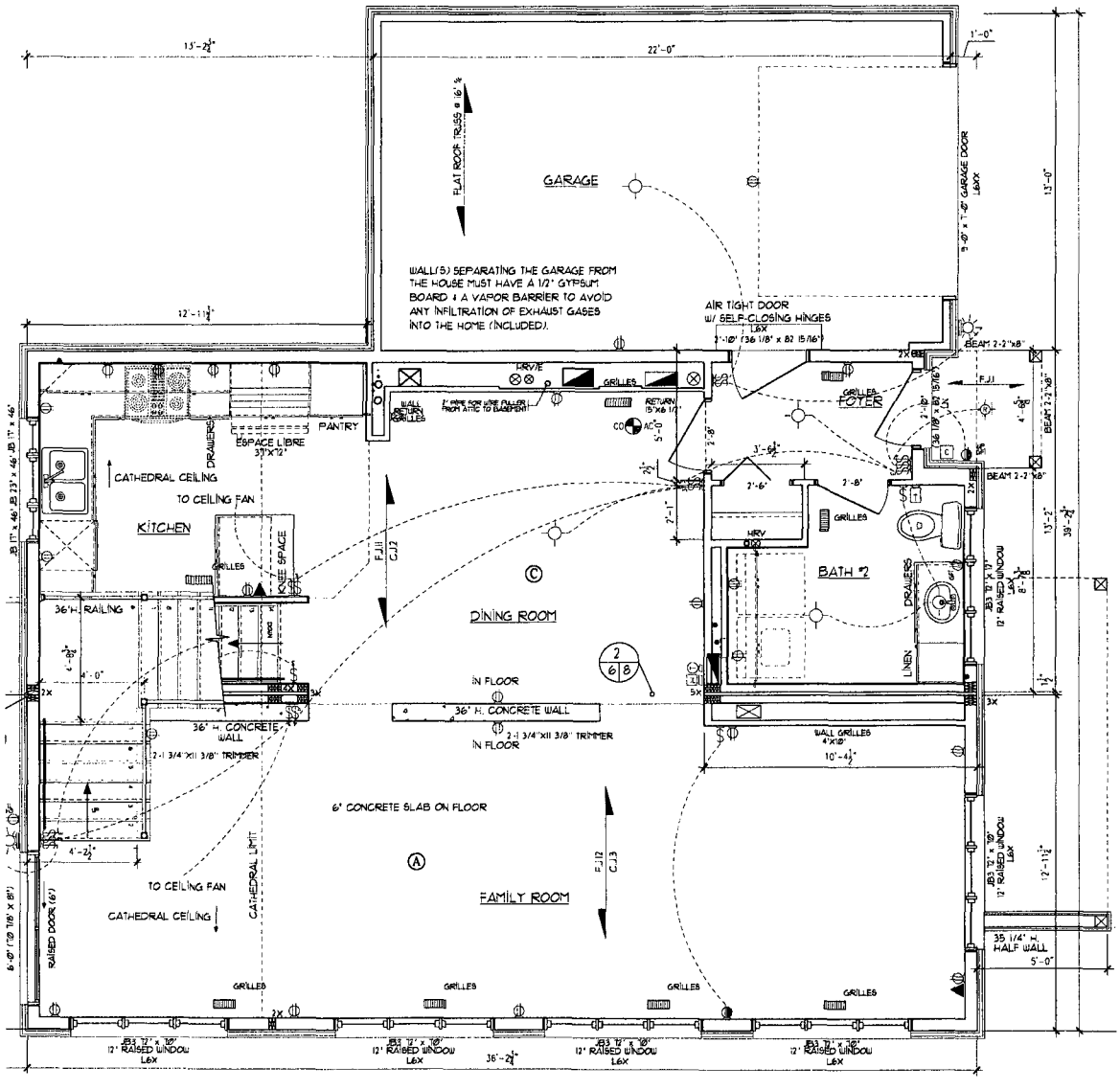

Figure A.3: Ground floor plan (courtesy of Alouette Homes)

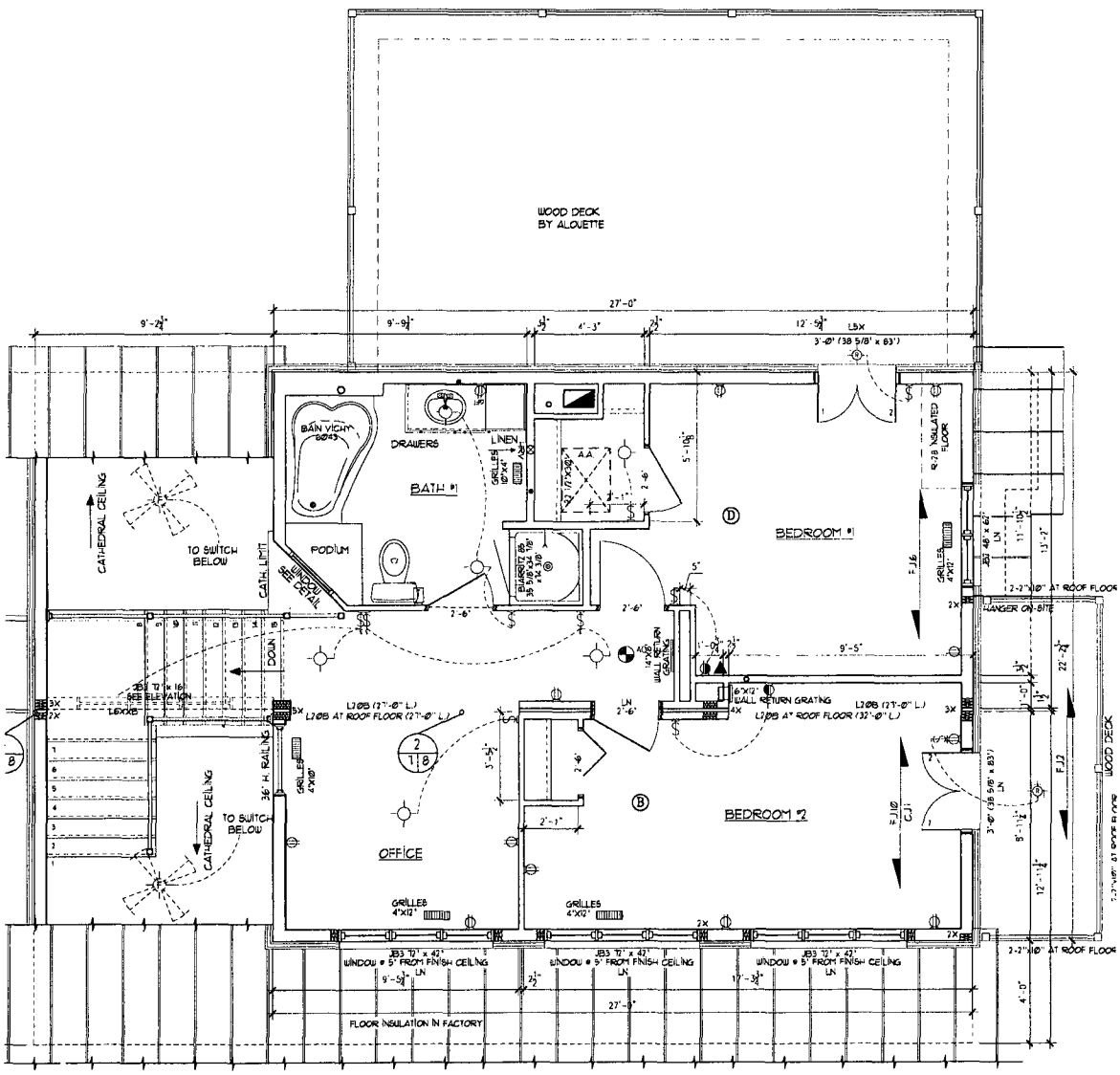

Figure A.4: 1st floor plan (courtesy of Alouette Homes)

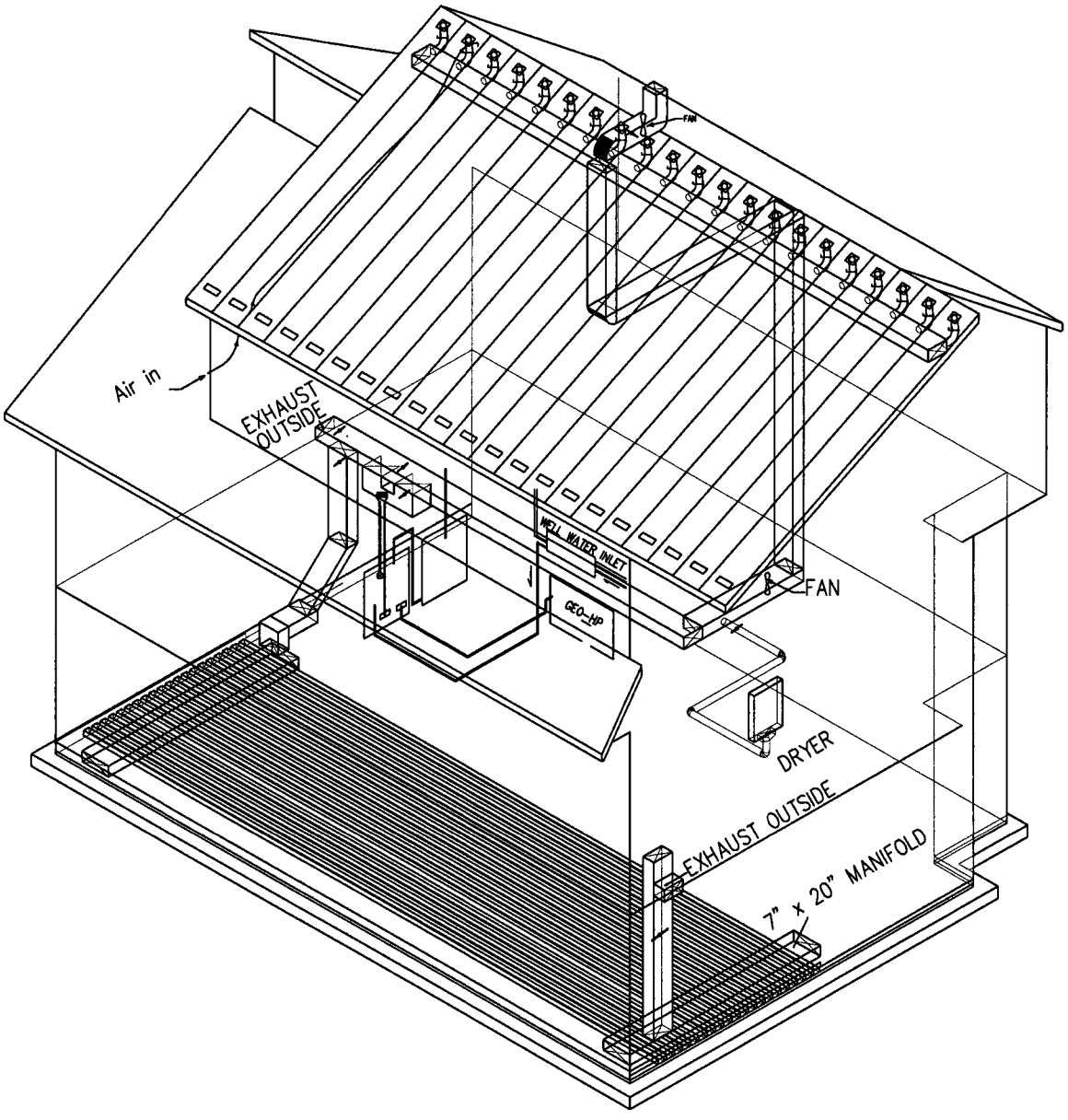

Figure A.5: Connecting BIPV/T with VCS (courtesy of Alouette Homes)

A.2 Construction Photos

(a) Floor structure

(b) Wall panels

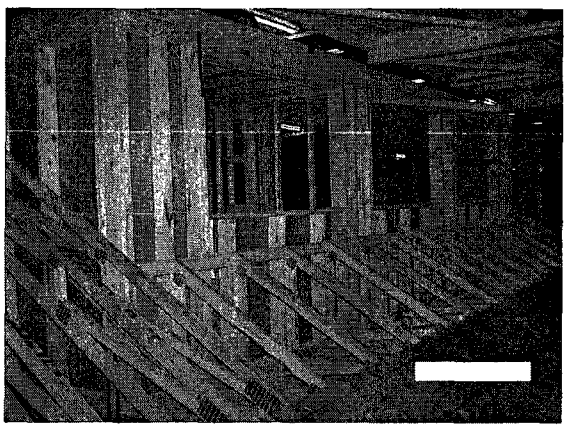

(c) Frame of one module

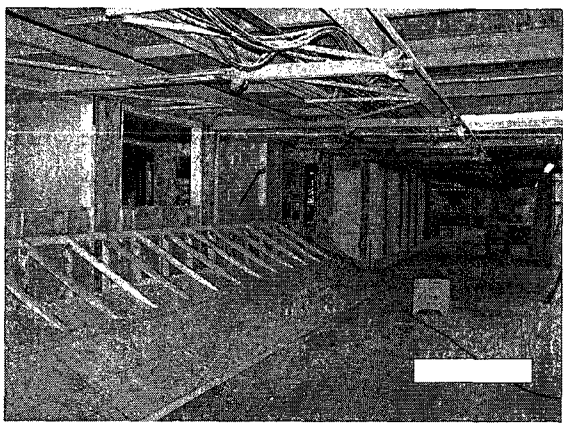

(d) Insulation

Figure A.6: Factory prefabrication

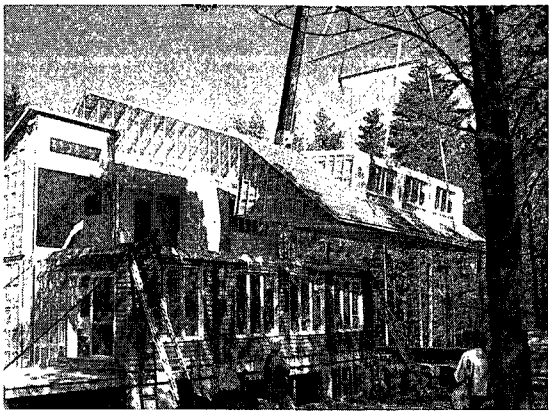

(a) Bedroom module

(b) BIPV/T module

Figure A.7: On-site modules assembling

(a) Ground floor

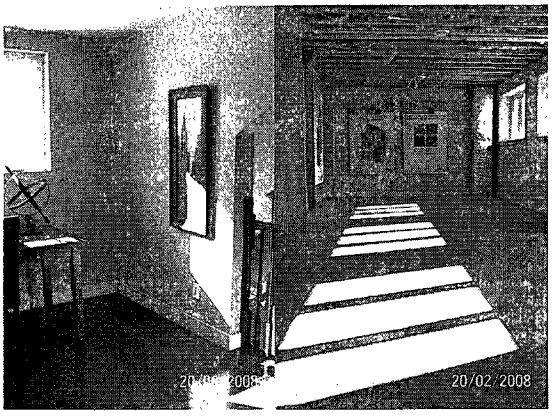

(b) 1st floor and basement VCS

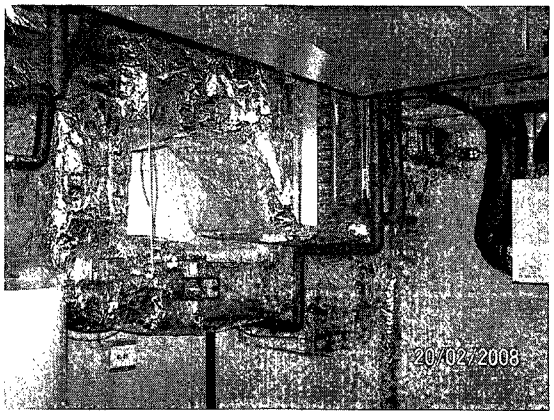

(c) Mechanical system

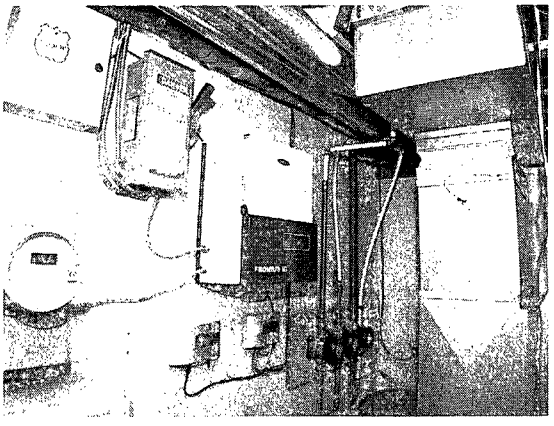

(d) Instrumentation

Figure A.8: Built environment

A.3 Thermal Insulation for Envelope

The samples of the final products of the two kinds of insulation can be seen in Figure 6.9(a). "Enertite®" is a low-density, semi-flexible polyurethane foam that has an open cell structure. At a 25.4-mm thickness, the design thermal resistance is 0.67 $m^2 \cdot K/W$ (R 3.8). Enertite also improves the acoustic insulation of the envelope [CCMC, 2007].

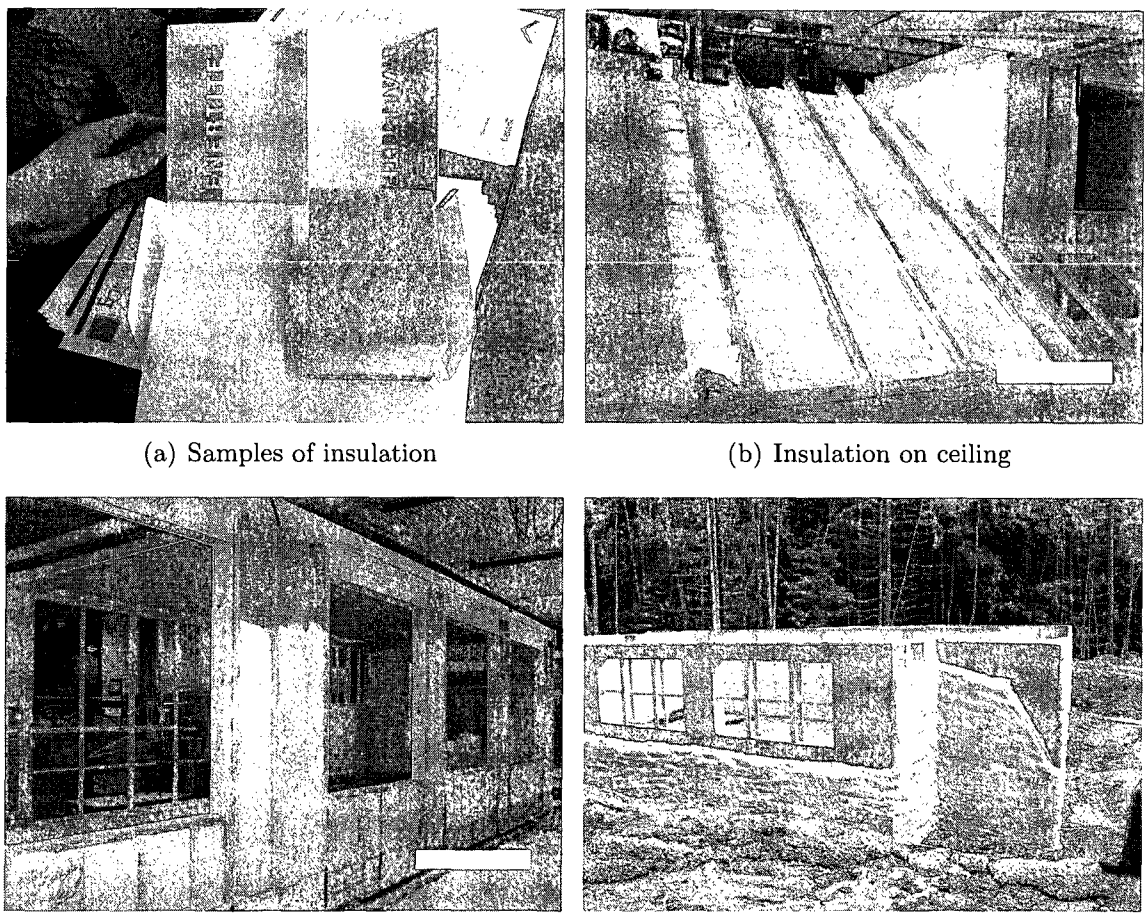

(a) Samples of insulation

(b) Insulation on ceiling

(c) Insulation on wall

(d) Insulation on foundation wall

Figure A.9: Insulation samples and on-site applications

"Walltite®" is a medium-density, rigid polyurethane with close cells. The final cured product has an assigned design thermal resistance of 1.05 $m^2 \cdot K/W$ per 25 mm (R 6 per inch). Other than being thermal insulation, Walltite acts as an air or vapor

barrier and also contributes structural rigidity to the wall system. The spacing of the 2"x6" wood stud increases from 16" to 24", which also means less thermal bridging [CCMC, 2006]. Spray foam Walltite costs more than traditional batt insulation. However, since Walltite serves as both insulation and air/vapor barrier, it can be cost competitive compared to batt insulation because it eliminates the steps for air-tightness detailing (such as caulking, applying house wrap and vapor barrier, and taping joints).

One of problem for applying spray-in-place foam insulation is that the insulation expanded after spraying. The expansion volume cannot be control easily. The excessive portion has to be cut manually. The time spent in the cutting process is much longer than the spraying part. The total insulation process for the modules of the house above basement cost about 3 days.

A.4 Solar Thermal System

It was decided that traditional solar thermal systems such as solar water heating systems are not be installed. This is mainly because of the consideration of the cost and the architectural appearance. The total cost of a solar water heating system, including a 3 m^2 collecting area, installation, testing and other accessories, normally cost around CAN$4,000. If this amount of money is invested in the PV system, an extra 0.5-kW peak PV capacity could be installed. The extra 0.5-kW capacity means roughly an extra 600 kWh of electricity can be gained annually. Conservatively assuming the average COP of the GSHP is 3, 1800 kWh of energy would be produced by the GSHP for DHW heating. Based on the HOT2000 simulation, for 150 liters DHW at 55°C per day, the annual DHW heating load is around 3300 kWh/year. The gap between 1800 and 3300 kWh/year could be covered by other energy-saving technologies: the drain water heat recovery system is able to contribute about 700

kWh/year and the BIPV/T system about 1000 kWh/year. The DHW heating energy need would be satisfied. However, GSHP for DHW heating is not adopted. This is because proper GSHP model cannot be found from local suppliers. Instead, desuperheater from space heating GSHP is used to aid DHW heating. The desuperheater in the chosen GSHP model is able to provide about 170 kWh per year for DHW heating based on simulations.

Appendix B Additional Information on BIPV/T System

The information provided in this appendix is about the BIPV/T system adopted in the solar house ÉcoTerra.

B.1 Construction of BIPV/T System

A 2.9 kW PV system is installed in ÉcoTerra. The total cost of the PV system alone is about CAN$29,000. The sizing of the PV system considers the estimated annual electricity consumption of the house, the roof area (9.2 meters (30 ft) by 5.5 meters (18 ft)), and the cost affordability of the PV system. Metal roofing is chosen and amorphous laminate PV panels are glued on top of the metal pan. Using metal roofing forms a continuous boundary without air leakage. PV panels can be easily and firmly adhered to the metal roofing, so durability is assured.

Outdoor air is used as the heat transfer fluid for simplicity and practical construction purposes. It's an open loop system. When thermal energy is not desired, a ventilation fan will be turned on to exhaust the outdoor air directly after it passes underneath the PV panels (Figure B.2, the ventilation fan is actually installed between damper "D4" and the vertical vent). The temperature of the PV panels will be kept close to the ambient temperature in the hot season. When thermal energy is desired, a more powerful variable speed fan will draw the air down to the mechanical room for different applications, such as slab or DHW heating, clothing drying, etc.

The following photos show details of the construction of the BIPV/T roof (Figure B.3 and B.4). A cavity is created between the metal roofing and the sub-layer (wood sheathing). Air channels are partially separated by battens, as shown in Figure B.3.

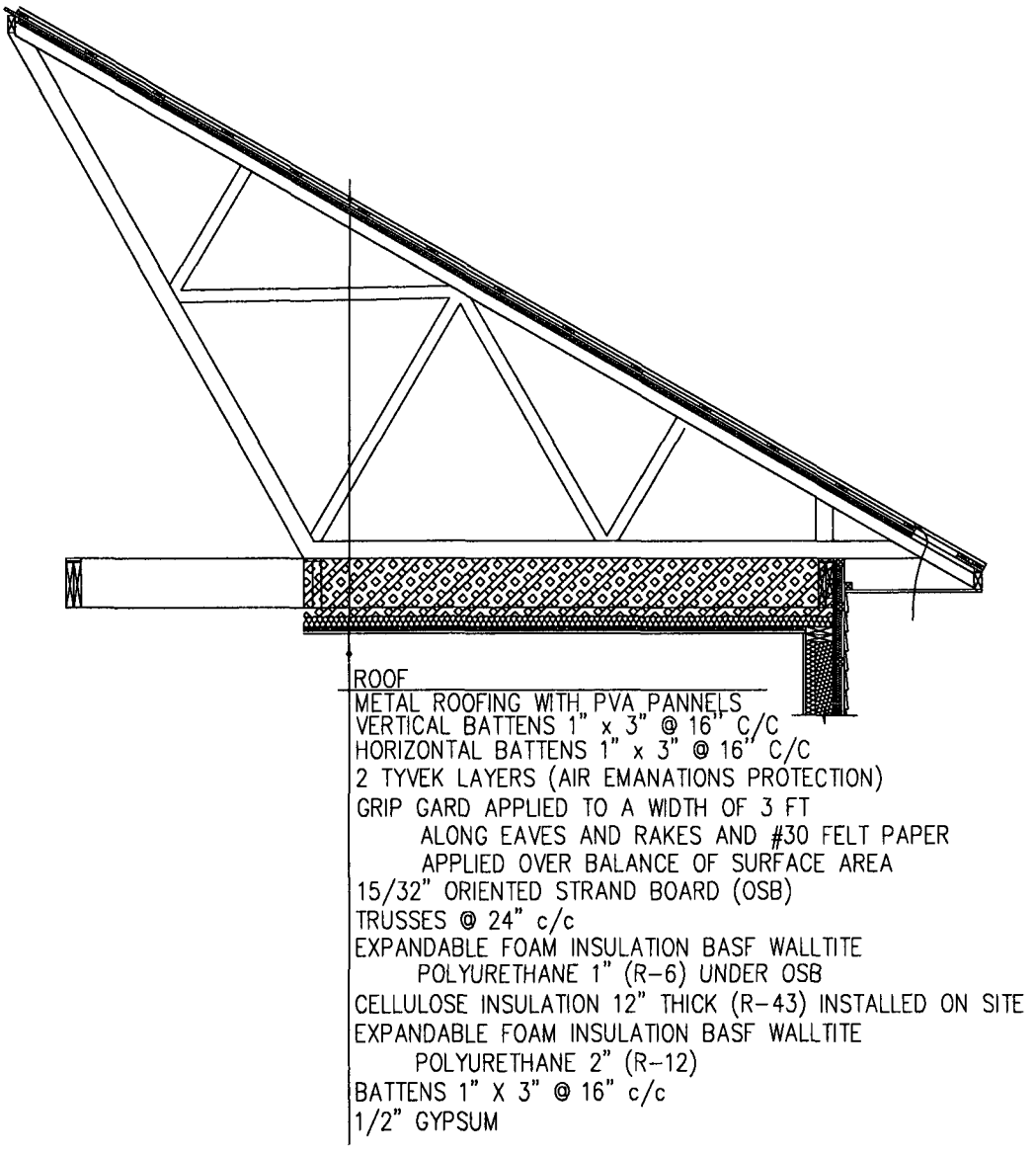

Figure B.1: Section of BIPV/T roof (courtesy of Alouette Homes)

Each air channel is 170 *cm* ($6\frac{1}{2}$ inches) wide. The inlet is 150 cm (6 inches) in steam direction. Photo 6.3(f) on the right hand side shows the inlet of air channel (from ground looking up) after the roof is covered by metal roofing. Photo 6.3(d) shows the outlets of the air channels, which are near the top edge of the roof. Vertical batten are cut before they reach the edge in order to reduce obstructions and even out the pressure distribution for smoother air suction.

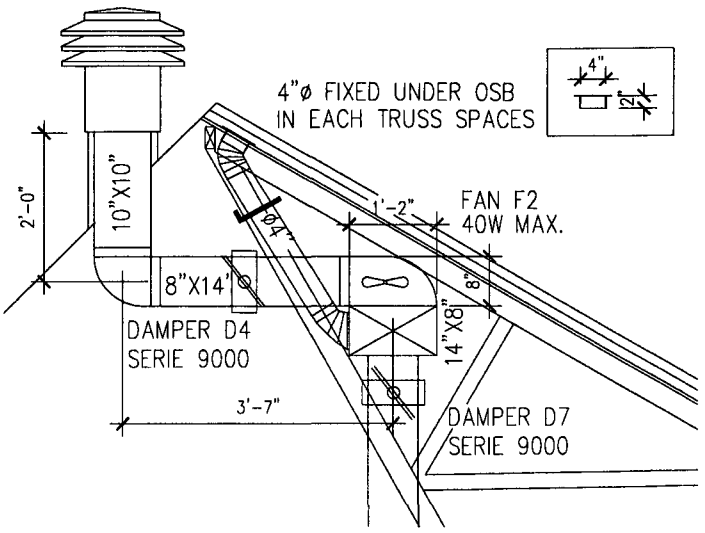

Figure B.2: BIPV/T system outlet (courtesy of Alouette Homes)

Collecting ducts behind the roof join the manifold and the outlets (Figure B.4). Each duct has its own damper. Pressure drop test were carried out, and dampers are adjusted to make sure flow rates in each duct are equal (i.e. balance of pressure drop). After the damper adjustment, Walltite insulation is sprayed under the roof and around the ducts to provide thermal resistance and air tightness. The thermal insulation will reduce the heat loss from the collected warm air to the cold attic space.

The construction of the roof, the placement and electrical wiring of PV panels, duct installation, and insulation form spraying was done inside the factory. Together with other modules of the house, the roof is shipped to the site and assembled by a crane. The air inlet of the BIPV/T roof is covered by the soffit. The outdoor air will pass through the soffit and then enters the air cavity.

(a) Glue PV panel on metal roofing

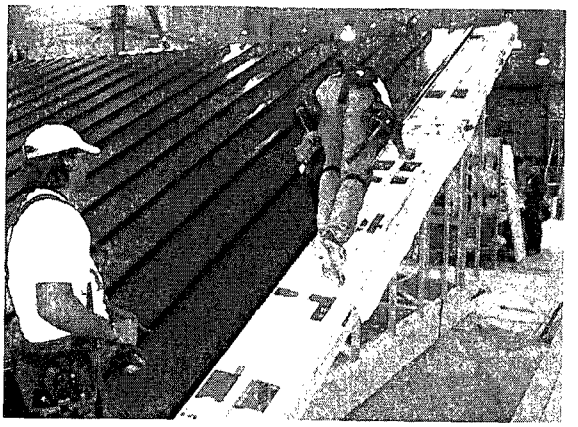

(b) Install metal roofing

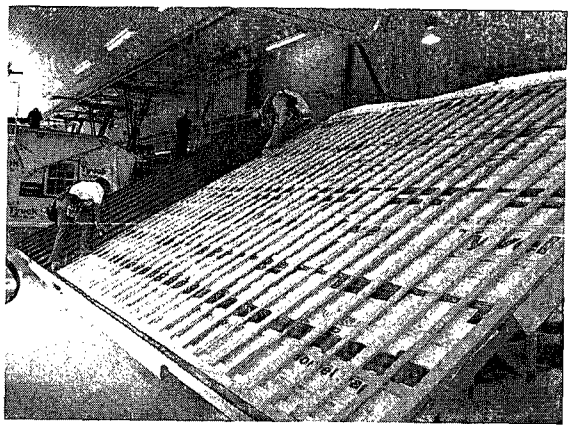

(c) Wood frame base

(d) Outlet

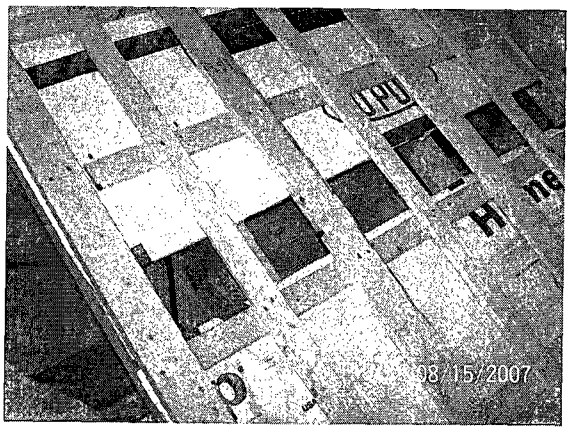

(e) Inelt top view

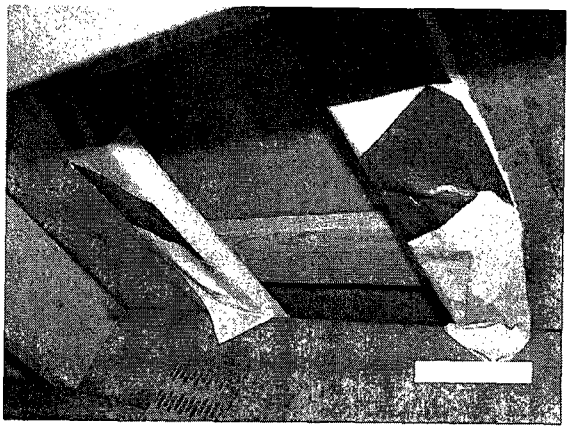

(f) Inlet bottom view

Figure B.3: Construction of BIPV/T - part a

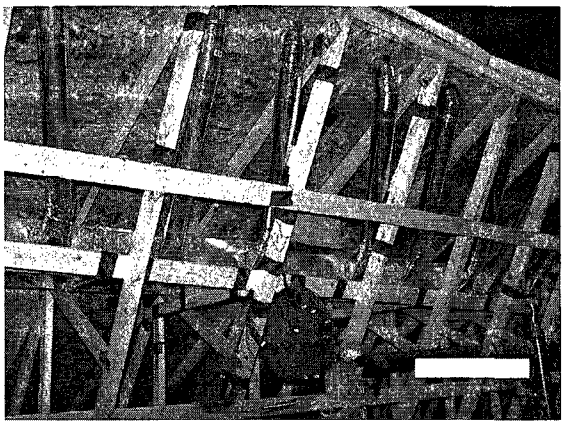

(a) Air collecting duct

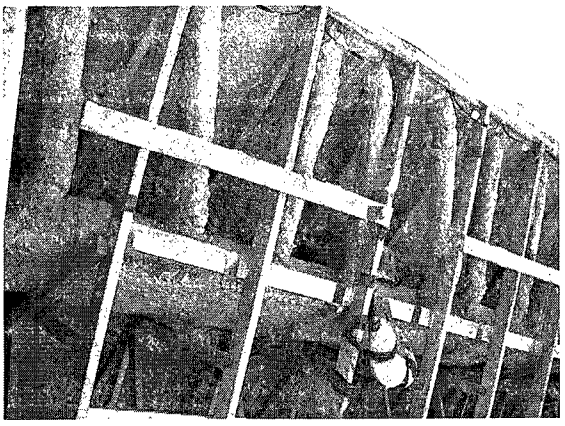

(b) Duct insulation

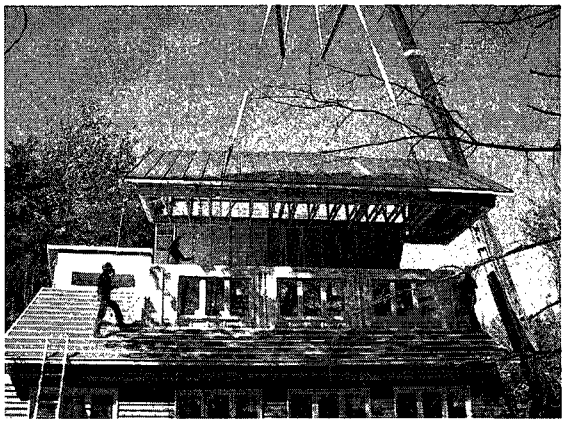

(c) Assemble BIPV/T module

(d) BIPV/T inlet

Figure B.4: Construction of BIPV/T - part b

B.2 Future Improvement

Snow accumulated on roof

In cold climate areas, solar thermal devices and PV system being covered by snow is a common problem. If the devices are covered by snow, they are not able to function as designed. Methods for avoiding snow covering or reducing the time of snow covering should be considered during the preliminary design stage. One common solution to snow covering is to increase the tilt angle of the solar device. In such way, the snow will automatically slide off from the device's surface. The tilt angle of the BIPV/T roof was designed to be 45 degrees in the preliminary design stage; however, the slope

was constructed as of 30 degrees. This change results in a considerable snow covering situation.

On a winter morning, the roofs were covered by a thin layer (2 cm) of snow, on both the south-facing 30-degree tilted BIPV/T roof and the north-facing 45-degree tilted normal roof (Figure 6.5(a) and 6.5(b)). The snow on the south-oriented roof (with 30 degrees tilted angle) melted and slid down completely after 2 to 3 hours under strong solar radiation. This shows that, with 2 to 3 hours of strong solar irradiance and 30-degree tilt angle, a thin layer of snow can melt away (Figure 6.5(c)). On the other hand, the snow on the north-oriented roof (45 degrees) stayed still (Figure 6.5(d)). A small pile of snow (about 5 cm) was near the gutter (there is no gutter for the BIPV/T roof). Comparing the two small east-oriented 45-degree tilted overhangs shown in (Figure 6.5(c)), there was thick snow accumulation on the upper overhang, but the snow on the lower overhang disappeared. This proves the solar radiation is critical in removing snow. The observations of other houses around the ÉcoTerra site also show that 45-degree tilt slope without strong solar radiation is barely steep enough to make the snow slide down automatically. Strong solar radiation plus a 45-degree or larger tilt angle slippery slope is required in order to make snow slide down the roof in a short time (i.e. half to one hour). There should be no obstruction (e.g. gutter, a slope with smaller tilt angle) at the bottom edge of the roof. Wind might be another important factor.

The mechanisms of snow melting by solar radiation could be the following ways: part of the exterior surface, even a very small area, like the top edge of the roof, is exposed to and heated by the solar radiation; it could be also possible that the solar radiation is partially transmitted through the semi-transparent snow cover and heat up the surface underneath. The surface temperature rises to higher than 0 °C, and then snow melts, becoming water. The water behaves like lubricant between the

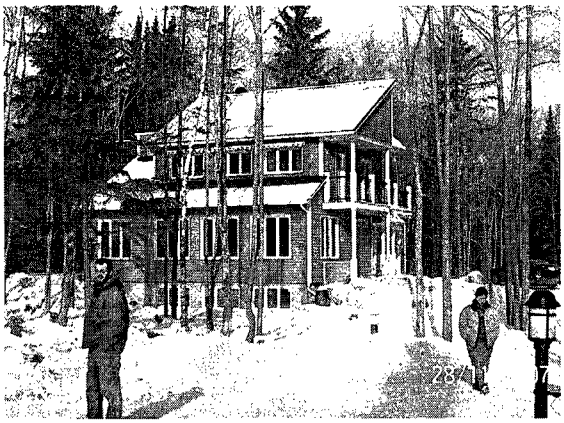

(a) 10:00am

(b) 10:00am

(c) 12:00pm south roof

(d) 12:00pm north roof

Figure B.5: Snow accumulation on roof

snow and the metal roof. Snow starts sliding down the roof.

Tree shadow

ÉcoTerra is built in a well-wooded area. The house is surrounded by deciduous and coniferous trees. Figure B.6 shows the engineering calculation for the requirement of on-site tree clean-up. Not all tall deciduous trees were cleaned under environmental and aesthetic considerations. Some of the coniferous trees in front of the house were not cleaned somehow (Figure B.7). Those leftover trees cast shadow on the PV panels and hence reduce the electricity production of PV panels, especially in the

winter time when solar angle is low.

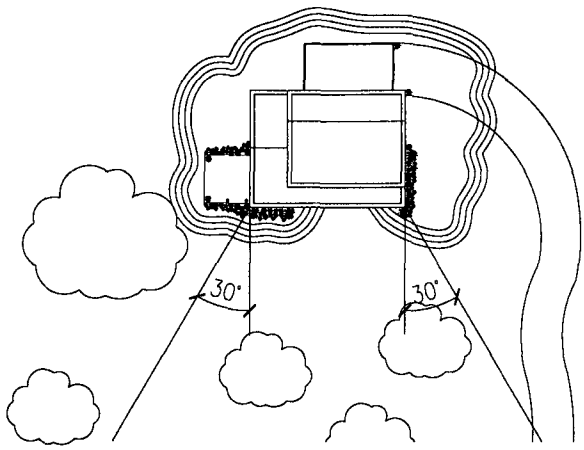

(a) Plan

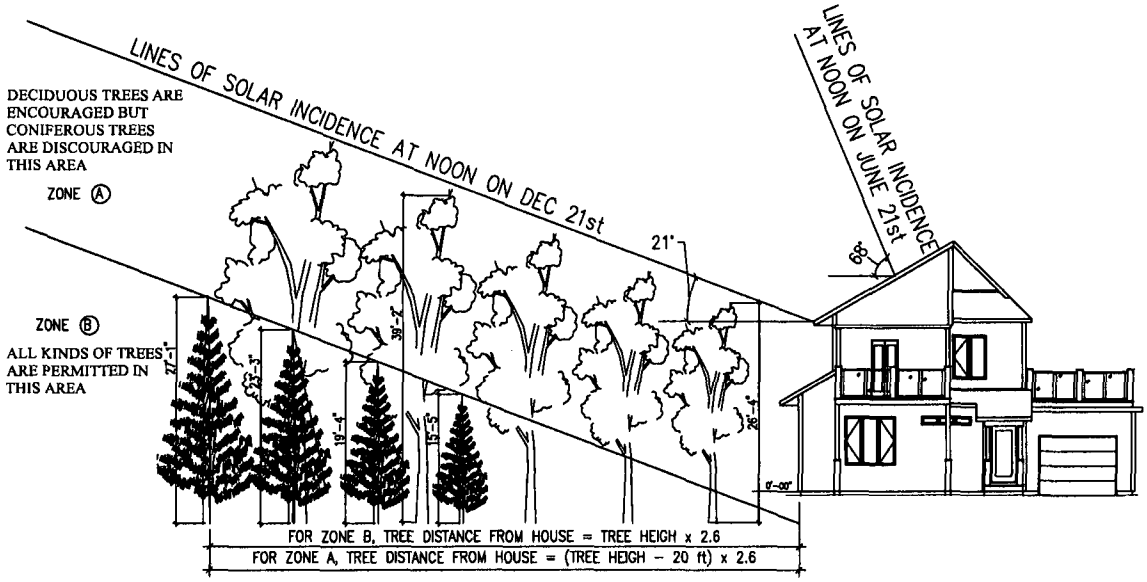

(b) section

Figure B.6: On-site tree cleaning

Duct work

BIPV/T system has strict requirements for the quality of the duct work. The duct work should be air tight and well insulated. However, in the site tests, the air leakage through the damper "D4" (Figure B.2) at the roof outlet is observed. Air leakages at joints between different duct line components (e.g. fan, duct sections) are

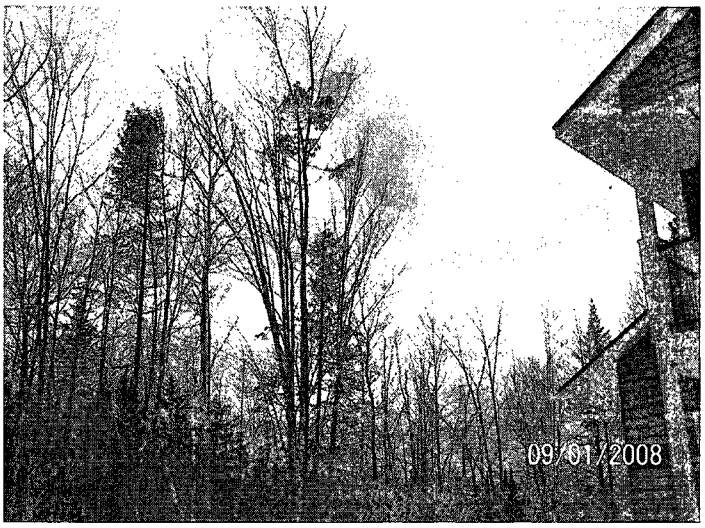

(a) trees in front of the south facade

(b) tree shahow cast on the roof

Figure B.7: Tree shading

also observed. During heating season, when warm air is being drawn from BIPV/T system, the warm air will be mixed with the cold outdoor air from damper "D4', and also with the indoor air. In this way, the thermal energy collected will be degraded. Site tests show that when warm air is being directed to the basement for heating purpose, a large temperature drop ($\sim 10\,^{\circ}\mathrm{C}$) is observed. This is caused by insufficient thermal insulation along the duct line, as well as air leakages.

Another problem with regards to the snow issue is discovered. Water dripping from the air collecting duct into the attic space is observed during the winter. This is because the outlet opening of the ventilation chimney is too close to the surface of

the roof. Accumulated snow drops into the chimney and melts. This also reveals that heat is escaping from the house through the hot air collecting duct. When the fan is not operating, indoor air will exit outdoor through the duct line and the exhaust outlet by buoyancy effect. This causes extra undesired heat loss from living space.

Appendix C Additional Information on VCS

C.1 Concrete Thermophysical Property

For practical calculation purposes, the thermophysical properties of normal-weight concrete correlated with its density are tabulated below. In normal construction, the commonly used concrete weighs about 2300 kg/m^3.

Table C.1: Thermophysical properties of normal-weight concrete. (Source: edited from the data provided in ACI-122R02 guide)

Density (oven-dry) $[kg/m^3]$	1603	1763	1924	2084	2244	2405
Specific Heat $[J/(kg \cdot K)]$	879	879	879	921	921	921
Thermal Capacity $[kJ/(m^3 \cdot K)]$	1409	1550	1691	1920	2067	2215
Conductivity $[W/(m \cdot K)]$	0.7~0.9	0.9~1.0	1.0~1.2	1.3~1.4	1.6~2.3	2.0~3.2
Equation 6.1 $[W/(m \cdot K)]$	0.64	0.78	0.96	1.17	1.43	1.75

The values of conductivity provided in Table C.1 are suggested for concrete in service. In reality, the conductivity is greatly influenced by the type of mineral and amount of aggregate mixed in the concrete and also the moisture content. Thermal conductivity of a discrete two-phase system, such as concrete, can be calculated (in oven-dry condition) using the *cubic model* by knowing the volume fractions and the thermal conductivity values of the cement pastes and aggregates [ACI Committee 122, 2002]. If the data are not available, the concrete conductivity can be estimated using Equation 6.1. However, this equation underestimates the k_{cnc} for normal-weight concrete. Furthermore, when steel reinforcement is used, the effective k_{cnc} will be further increased.

$$k_{cnc} = 0.0865 \cdot e^{0.00125 \cdot d} \tag{6.1}$$

where

d is the oven-dry density in kg/m^3.

C.2 Construction of VCS

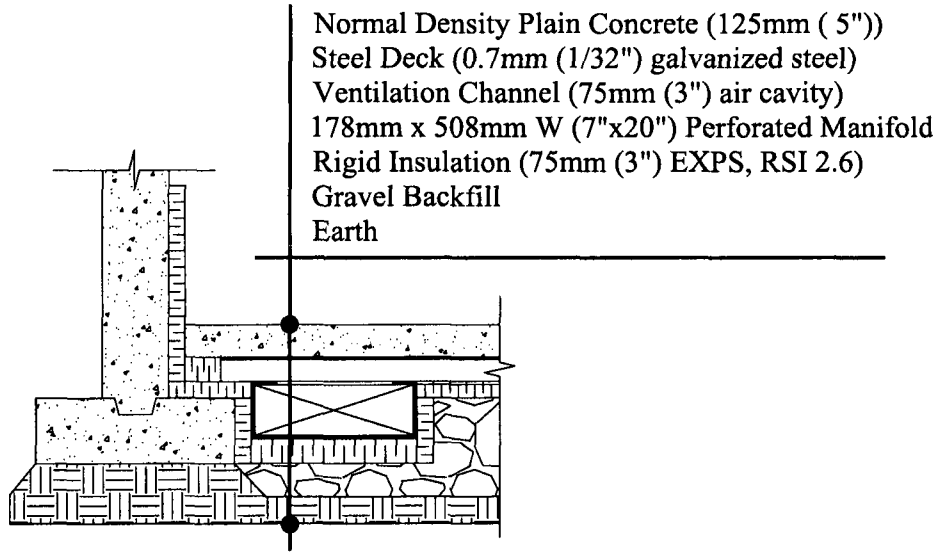

Figure C.1: Cross section of VCS at manifold (courtesy of Alouette Homes)

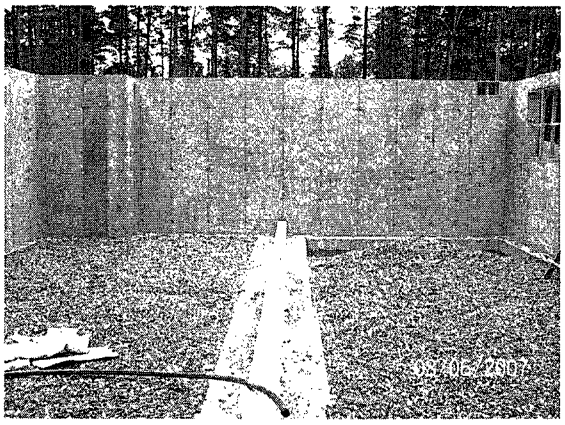

(a) Backfilled gravel

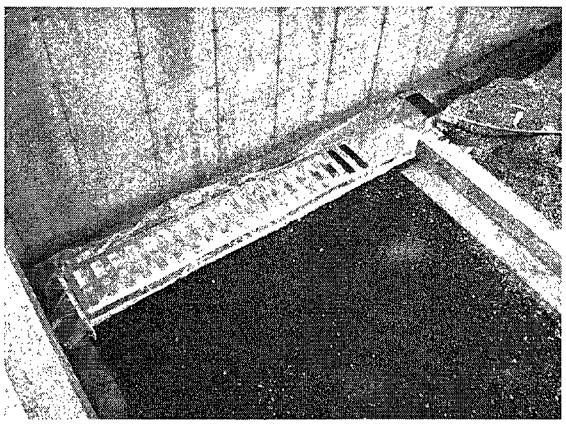

(b) Inlet manifold

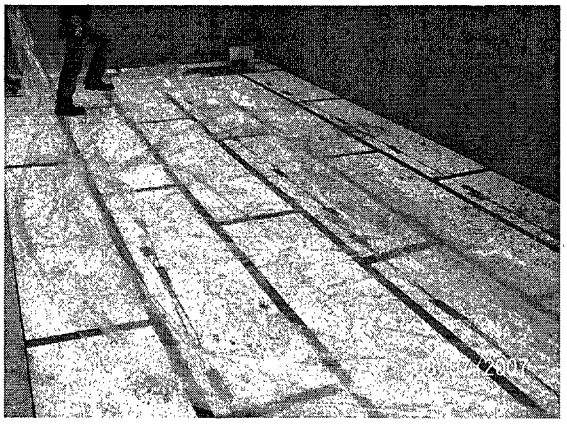

(c) Vapor barrier on top of rigid insulation

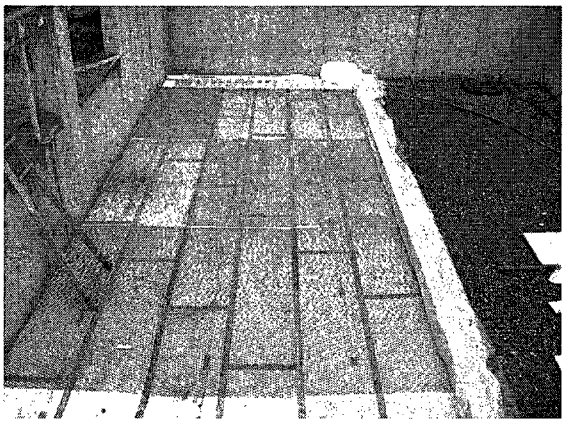

(d) Metal mesh

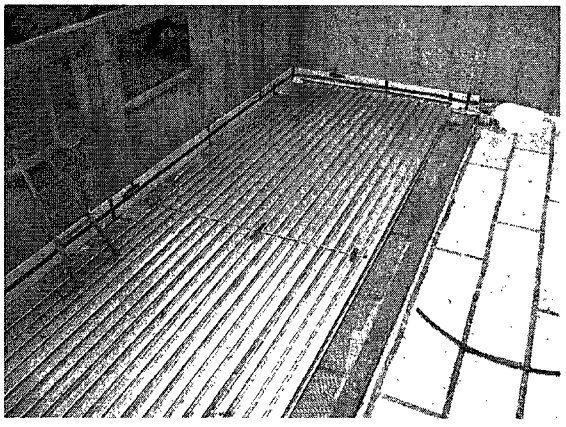

(e) Steel deck

(f) Pouring concrete

Figure C.2: Construction of VCS

The End